THESIS

OPTICAL DETECTION METHODS FOR MICROFLUIDIC DEVICES

Submitted by

Marina M. Koepke

Department of Electrical and Computer Engineering

In partial fulfillment of the requirements

For the Degree of Master of Science

Colorado State University

Fort Collins, Colorado

Summer 2020

Master's Committee:

Advisor: Kevin L. Lear

Jesse Wilson
Daniel Gustafson

ABSTRACT

OPTICAL DETECTION METHODS FOR MICROFLUIDIC DEVICES

Optical technology is a common tool integrated onto microfluidic devices to aid in data collection and counting for biological and chemical research. In this study, a simple optical technique was investigated as a detection method for microfluidic impedance cytometry (MIC) devices. The MIC devices were designed to characterize size and structure of parasite eggs through electrical impedance measurements. This data could directly benefit the medical and veterinary communities by providing information to aid in addressing helminth infections in humans and animals. The current MIC device and instrumentation does not provide a robust way to validate which impedance changes correlate to parasite eggs passing through the electrodes. To address this, an optical detection method was designed, implemented and tested on two different types of microfluidic devices: a glass device and printed circuit board (PCB) device.

The optical hardware was accompanied by a trigger circuit that was used to process and manipulate the detected light signal. The circuit was designed with a sensitivity that would detect small changes in light from strongyle-type eggs flowing through the microfluidic channel. The trigger circuit was composed of multiple stages of signal amplification and oscillation suppression techniques so the changes in light could clearly be detected by the electronics. This method proved to be successful in detecting voltage changes ranging from 1.7 mV to 6.8 mV which resulted from strongyle egg sized particles (63-75 μm in diameter) flowing through the microfluidic channel.

Adaptations for the optics, bench set-up and microfluidic device design were investigated to transfer this method to different laboratory settings. This study outlines the process of utilizing basic lab tools and components to create an easy to implement optical detection method for a variety of chip designs and laboratory set-ups.

DEDICATION

I would like to dedicate this thesis to the Fraser, Colorado mountain community for their support and creative insight that helped in the completion of this project during the COVID-19 pandemic.

TABLE OF CONTENTS

Chapter 1

Introduction

Microfluidics research is a growing field in chemical and biological sciences and is a technology used to control and manipulate fluids flowing through a microchannel. In a field of microfluidics called microfluidic impedance cytometry, micron size particles are studied by suspending the particles in liquid and passing them through a microchannel [1, 2]. Microfluidics can incorporate various measuring techniques which includes electrical and optical [3, 4]. Microfluidic chips provide a simple, compact and cost effective alternative to large traditional equipment used for cellular and micron sized studies [5].

Microfluidic impedance cytometry (MIC) is a label-free technique used to count and characterize various types of cells through electrical measurements [6]. In the research accompanying this thesis, MIC was being investigated as a method to study parasite eggs. The impedance data acquired from parasite eggs is expected to provide measurements concerning the exterior and interior structure of the egg. This information could directly benefit the medical and veterinary communities in addressing and studying helminth infections in humans and animals.

Optical integration onto microfluidic devices is another common measurement technique. Fluorescence based measurements, optical scattering, microscopy and miniaturized flow cytometers are a few of the ways optical methods have been used in molecular and cellular microfluidic analysis [7]. Optical systems are generally bulky, expensive and require trained personnel to operate, which can limit the availability of this technology to some laboratories. Miniaturization of optics such as micro-lenses and small diameter optical waveguides have been one way researchers have successfully incorporated optics onto these devices [7, 8]. While implementing micro-optics onto microfluidic devices reduces the size of the optics, issues such as scattering and unwanted reflections make integration of the optics difficult [7] and still requires trained personnel to operate and integrate the optics.

1.1 Motivation

The goal of our MIC chip was to provide a portable and label-free method for determining helminth infections in livestock. Using an MIC device to study and count parasitic loads in animals could lead to the elimination of bulky equipment which would allow for untrained personal to test their own animals in a cost effective way.

The design of our MIC data acquisition instrumentation did not have a robust method for taking impedance data for every egg/glass bead (used for testing) passing through the channel [9]. A field programmable gate array (FPGA) took impedance measurements in 4 second intervals with an additional 4 second off-loading interval of data onto the computer [9] where no impedance data could be collected. This could lead to missing measurements of objects flowing through the channel during that off-loading period. This could yield an inaccurate count of eggs in a test sample. While an average count of eggs/beads could be obtained by taking the average events that occur in each time period, clumping of eggs/beads and the non-uniform dispersion of particles in the medium could offset this average count. The only form of verification of the impedance data was a live video feed where the times of events were recorded separately and then later correlated to the collected data. This created some uncertainty on whether the impedance data recorded corresponded to an egg/glass bead, debris, bubble or the suspending solution as the exact times recorded based on the live video feed varied slightly from the time on the recorded data. An optical trigger could alleviate these problems by providing a signal when an egg passed through the electrodes. This signal could then be correlated to the impedance data and be used to initiate data acquisition. The optical signal of a parasite egg passing through the channel could also provide the ability to obtain an absorption profile of the egg. This absorption profile would be an additional measurement in characterizing the size and shape of the egg and could be used to compare against the impedance data. This could reveal trends between the two types of data potentially providing more information for helminth research.

1.2 Overview of Chapters

The information outlined in this document provides the methods used to establish an optical detection system to enhance data collection for the MIC devices and presents the results of the design capabilities. Multiple design stages of the light detection and trigger circuits were conducted using different microfluidic devices, test samples and optical set-ups. These stages are summarized in Table 1.1 and detailed explanations can be found in the corresponding sections.

Table 1.1: Summary of circuit design stages. TIA: Transimpednace Amplifier, LPF: Low Pass Filter, HPF: High Pass Filter and PCB: Printed Circuit Board.

Circuit	Microfluidics	Test Sample	Optics	Manuscript Section
TIA	Glass	Stationary Glass Bead	Microscope 1	4.2
TIA	Glass	Moving Glass Bead	Microscope 1	4.2
TIA and Inverting Amplifier	None	Opaque Card	Microscope 1	4.3
LPF without Buffer	None	Opaque Card	Microscope 1	5.2
LPF with Buffer	None	Opaque Card	Microscope 1	5.2.1
LPF with Amplifier	None	Opaque Card	Microscope 1	5.2.1
HPF	None	Sewing Thread	Microscope 2	5.3
HPF	PCB	Paint Spot on Fishing Line	Plastic Fiber Optic Cables	4.4.2
HPF and LPF at Comparator Output	None	Sewing Thread	Microscope 2	5.4

Chapter 2 provides a background of the current methods used to test for parasitic infections, technology of microfluidic systems (specifically MIC) and optical sensing methods for microfluidic devices. Discussion in this chapter focuses on the inconsistencies and difficulties with the current methods for diagnosing helminth infections and how the use of MIC devices can help mitigate those issues. An optical addition to microfluidic devices could be used to enhance data collection by providing cost effective and sensitive measurement techniques in addition to other data collection methods on the chip.

Chapter 3 discusses the apparatuses used to carry out the experiment. This chapter outlines the design of microfluidic devices used for testing and the optical set-ups for each device. The motivation behind the different samples used for testing the apparatus and circuit are outlined at the end of this chapter.

Chapter 4 describes the design of the light detection circuit. The design process and corresponding results for each design phase are discussed and presented here. Test results from samples described in Chapter 3 are presented here.

Chapter 5 outlines the design for the input voltages for the operational amplifier comparator trigger circuit. Multiple designs were tested to determine an effective technique to create a reference voltage for the comparator circuit. Simulations and breadboard tests were done to guide and troubleshoot the various designs.

Chapter 6 discusses the procedure for designing and adapting optical detection systems for different styles of microfluidic devices and different laboratory environments. Design considerations, methods for testing and errors to be aware of are discussed in this chapter to guide users on how to design and tailor an optical detection system to their specific microfluidic needs.

Conclusions and future work are discussed in Chapter 7.

Chapter 2

Background

2.1 Introduction

Parasitic infections in livestock and humans is one of the world's leading cause of mortality [10]. Specialized tests and training is required to properly diagnose helminth infections and there has been little advancement in the methods of testing [11]. A parasitic load in a host (animal, human or other organism harboring a parasite) is the number of parasites present in the host. Determining the parasitic load is important to establish the level of the infection which in turn will guide necessary treatment. Many methods for diagnosing target specific species of parasites and require intensive lab processing to obtain accurate results [11]. This makes diagnostic tests expensive and can limit reliability and availability.

Microfluidic impedance cytometry is a label-free method that can be used to characterize many kinds of cells [6], and one study has used this method to identify and analyze giardia at the oocyst level [12]. The current design of our MIC device aims to collect impedance measurements of parasite eggs passing through a 200 μm wide channel [9]. The impedance measurements of the eggs could lead to accurate counts and characterization of different kinds of parasitic loads and can be done by passing a small fecal sample through this simple device that would not require special training or education to use. The addition of an optical detector to this device could confirm which impedance measurements correspond to parasite eggs and yield greater confidence for data analysis.

Optical sensing and detection methods are commonly used with microfluidic research as there is a breadth of techniques that can be applied to obtain various kinds of data. Optics have been used to measure changes in light intensity, wavelength and phase to create profiles of the particles of interest [13]. It has also been used for mechanical processes such as cell sorting and manipulation on microfluidic devices [14]. Optical technology can be miniaturized with reduced fabrication

costs making it a favorable addition to microfluidic devices. Micro-optics are not widely used as the miniaturization compromises performance and sensitivity of the optics through coupling, reflective and other types of losses [14, 8, 13]. While on-chip optics is commonly integrated into high level microfluidic research, due to the specialized design requirements, optics are still not a routine practice for commercialized microfluidic devices [13].

2.2 Parasitic Diagnostic Methods

Parasite diagnostics have changed little in the past 20-30 years [11] and most tests rely on bulky and specialized equipment to accurately diagnose a parasitic infection. Fecal flotations, blood tests, molecular assays and microscopy methods are amongst the most commonly used techniques, but these methods often yield inaccurate results due to human error in interpretation of the data, incorrect sampling and poor preservation of the sample. This can often lead to a false diagnosis [15]. In some cases, a multitude of tests are required to accurately diagnose a helminth (parasitic worm) infection due to the specialization of tests for different species, lack of sensitivity, compromised samples and human error. Future development in diagnostic technologies for helminth infections look towards reliable, cost effective, user friendly and more portable devices for diagnosis [10].

Accurate parasite tests for livestock, animals and humans is a key factor for the progress of addressing and treating various types of helminth infections. Tests aid in determining geographical origins of parasites which help determine how they are spread and gives way to development of the most effective treatments [15]. There are many tests available to determine parasitic loads in animals that range from clinical tests to specialized tests that need to be conducted in the laboratory. Practitioners can carry out fecal floatation, in-house immunochromatographic and coproantigen tests. The conventional microscope tests (such as fecal flotation) are not able to distinguish between different species of parasites of the same genus within a single sample [10]. Laboratory tests include immunofluoresence antibody tests (IFAT), enzyme-linked indirect serology assays (ELISA) and molecular methods such as polymerase chain reaction (PCR). The laboratory tests are highly sensitive and rely upon proper handling of samples and trained scientists to run tests

and interpret results [10]. In addition, these methods of diagnosis can be over $100 per test panel [10] and are not as available as other lower cost tests. Most tests can identify a range of parasites, but extra tests may be required if other helminth issues are suspected. Nearly all tests are unable to identify between mild, severe and reoccurring infestations and require specialized equipment and trained personnel to carry out diagnosis [11, 15].

Microscopy is the leading technology for parasitic diagnosis compared to other widely used techniques such as assays, fecal floatation and serological based tests [15, 10]. Microscopy is one of the main practices for parasite diagnostics because it provides a range of methods that can be implemented for testing [10]. Some microscopy tests can be inexpensive making it more accessible to low income areas or research, but is not conducive for incorporating sensitive and precise testing instrumentation [11, 10]. Samples for microscopy studies range from invasive collection such as blood, bone marrow, tissue, lymph node and cerebrospinal fluid [11] to non-invasive collections such as fecal samples [11, 15, 10]. While there are many options in microscopy for testing, success of tests still relies on knowledgeable staff, financial support and proper handling of the samples which causes variability in accuracy of the results [10]. Changes in the technology could improve the accuracy of test by eliminating the margin for error when handling, storing and interpreting the data.

2.3 Microfluidics

Cellular research is paramount in understanding biology and the biological process of life, but the small size and diverse population of cells make them difficult to study. Microfluidics has been an integral tool in cellular research since the 1990s [16] that utilizes small amounts of flowing liquid through tiny channels and can incorporate a variety of cell detecting and measurement techniques [16, 5]. It is predominately used for research in medicine, biology and chemistry [5]. Microfluidic devices hold multiple advantages in studying and analyzing cells over tradition laboratory techniques as they are small volume diagnostic tools, inexpensive, have short reaction times

and high throughput for data analysis [5]. The versatility of microfluidic chips allows for progress in niche cellular research lending advances in the understanding of cellular biology.

A variety of detection and analysis techniques can be implemented onto microfluidic devices. Optical and electrical are the most widely used techniques and have been used to study and analyze the morphology and interactions of cells [4, 6, 3]. Common optical measurements include absorbance and fluorescence. Electrical based microfluidic measurements are label-free methods that provide an electrical model of cells yielding information on morphology and structure. These measurements are based on the impedance properties of a single cell at various frequencies [6]. In depth detail on electrical based microfluidic technology is discussed more in Section 2.4. Mechanical stimuli can also be implemented onto microfluidic devices which studies the cellular morphology response to stress and strain, co-culture interactions and response to different environmental stimuli [16].

2.4 Microfluidic Impedance Cytometry

Microfluidic impedance cytometry (MIC) is a label-free and non-invasive technique used to count and characterize single cells and has successfully been used to study mammalian and bacterial cells [6, 9, 4]. The cells flow through a microfluidic channel where they are measured at high and low frequencies. The "polarizations of the cells induced by an AC field, cause charges to accumulate between the cell membrane and suspended solution which have different dielectric properties"[6]. As the AC frequency applied to cell changes, the polarization of these built up charges change, and when measured, provide an impedance profile of the cell [6].

MIC is based on the Coulter Principle where the change of impedance of a conductive fluid between electrodes is proportional to the volume of the particle obstructing the path of the current [17]. The electrical properties of the cell reflect information regarding the physiology of the cell such as the morphology of the membrane, cell size and characteristics pertaining to the cytoplasm [4]. A range of AC frequencies can be applied to an electrolytic solution to identify impedance changes in that solution. As a cell passes through the applied field, charge accumulates between

the cell membrane and solution due to their difference in dielectric properties [6] which causes a change in resistance of the field. At low frequencies the cell membrane is essentially opaque (provides no current flow) and yields information on the cell size and volume. At high frequencies the cell membrane is seen as transparent and information regarding the internal structure and composition of the cell can be obtained [6]. These measurements can provide structure, size and composition information of each individual cell letting scientists distinguish between different populations [6]. This can give scientists and doctors a wide range of information regarding cellular processes and can be applied to clinical studies of drug screening and diagnosis for cellular pathologies [6].

2.5 MIC for Parasite Egg Analysis

In a proof-of-concept study, a MIC device was designed with the aim to collect impedance data on parasite eggs to provide an advanced testing apparatus for parasitic loads in livestock. Diagnosis and antihelminth treatment for large populations of livestock is highly dependent on fecal egg count reduction tests (FECRT) [9]. These tests can be costly due to shipping of samples and the need for trained scientists to interpret data and also involves time lags between sample collection and testing that could destroy the integrity of the sample [9]. This study consisted of fabricating a glass MIC device with a 100-200 μm wide channel with electrodes connected to a field programmable gate array (FPGA).

This MIC device utilizes multiple AC frequencies to gather information such as size, composition and structure of cells creating a full profile of the egg based on its electrical measurements [9]. The structures of the cell each have different polarizations so when an AC field is applied, it causes a charge accumulation between the membrane of the cell and the medium it is suspended in due to their different dielectric properties [6]. Fig. 2.1 shows the change in impedance (Δ Z) versus the AC frequency.

When lower AC frequencies are applied to the channel, the shell of the parasite egg acts as an insulator and blocks current flow through the egg providing information regarding the size and shape. At higher AC frequencies, current passes through the shell of the egg and thus can provide

a profile of the internal structure of the egg. The multiple AC frequencies are necessary to provide a full profile of the egg due to the the different structures of the egg being opaque at different frequencies as discussed in Section 2.4 [9].

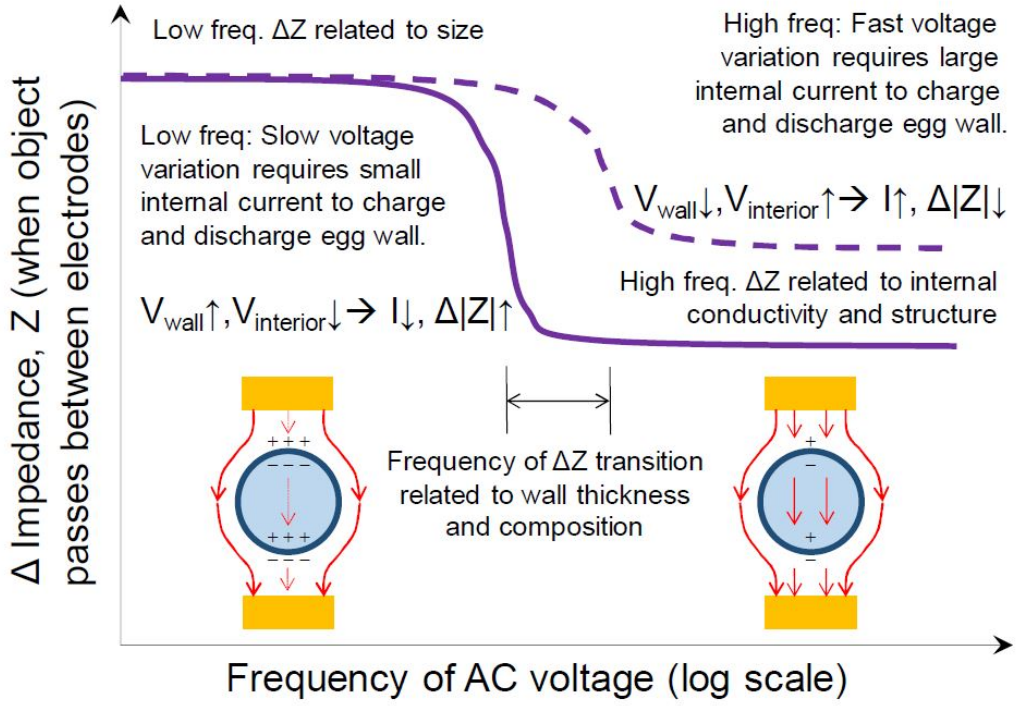

Figure 2.1: Illustration of the impedance change (Δ Z) versus the AC frequency. At lower AC frequencies, the shell of the egg acts as an insulator and no current flows through the particle. Higher AC frequencies do penetrate the egg shell providing internal structural information. Reproduced from proposal figure created by Kevin Lear.

An initial test of impedance data acquisition was done using glass beads with diameter sizes ranging from of size 63-75 μm, (approximately the same size as strongyle eggs at 65-100 μm[18]) combined with saline solution, that was pushed through the channel. The preliminary glass bead study was done to provide a beta test for the experiment. The results showed that the glass beads resulted in an increased impedance as they passed through the electrodes [9]. The impedance profiles of the glass beads are shown in Fig. 2.2.

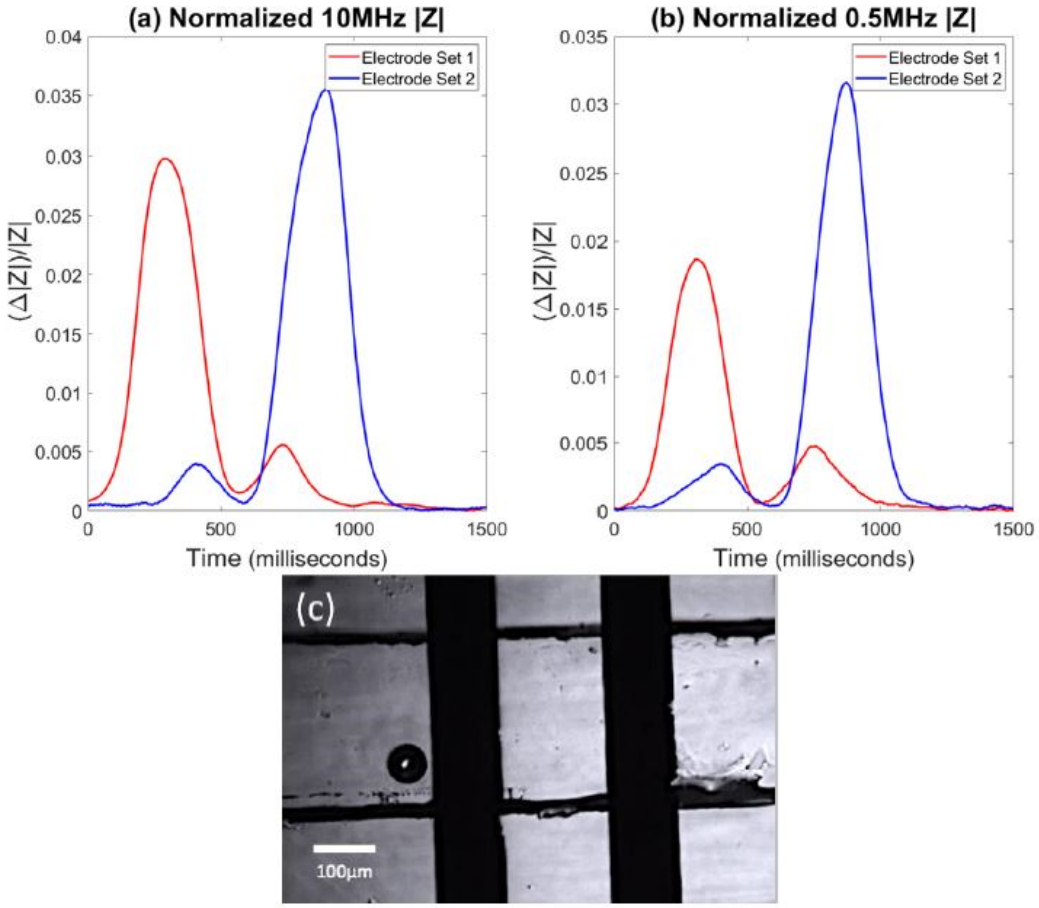

Figure 2.2: Time profiles of the change of impedance of a glass bead flowing through the microfluidic channel. The time profiles of impedance change at (a) 10 MHz and (b) 0.5 MHz demonstrate the different profiles of the bead when probed at the different frequencies. (c) Image of a glass bead as it passed through the 100 μm wide channel. Image from J. Nejad, et al, *Multifrequency Microfluidic Impedance Cytometry Using a Field Programmable Gate Array for Parasite Egg Analysis* [9].

While the structure and composition of the glass beads differ from that of strongyle eggs, these results provided confidence moving forward that particles of the same size and similar density would cause a change of the impedance. This would make it possible to count and study parasite eggs using this technique.

This MIC device was designed with electrodes fabricated using a lift off process onto glass slides joined by a double sided, laser cut adhesive tape channel 100-200 μm wide. This adhesive channel allowed the two glass slides to be combined to create the entire device. Headers for the

electrodes were placed on the side of the slides and used to connect to the FPGA for applying frequencies to the channel and to record impedance data [9]. The transparency of the glass slide allowed a camera image of the channel to verify the contents as well as provide an off-chip optical detection technique to improve data collection. The optical detection technique is discussed in Chapter 3, 4 and 5 of this manuscript.

2.6 Optical Sensing for Microfluidic Devices

Optical sensing technology is commonly integrated onto microfluidic chips and used for data collection and counting [7]. There are two main kinds of optical detection methods and can be implemented on or off the microfluidic device. On-chip optics allow for precise measurements but require special equipment and training to integrate correctly while off-chip optics require bulky and expensive equipment, but are generally easier to integrate [13]. Sensitivity of optical methods is reduced when implemented on the micro scale due to smaller optical path lengths and a decrease in size of the sensors [8].

Optofluidics is the integration of optical technologies onto microfluidic devices. Common implementations of chip integrated optics includes fluorescent based measurements, optical scattering and various forms of spectroscopy [16, 7] and incorporates labeled and label-free techniques. The design goal of optofluidics is to reduce size and complexity of the traditional bulky and expensive optical systems. One technique that is used involves placing optical waveguides onto the device oriented close to the channel. This miniaturizes the optical detection equipment and eliminates the need for manual alignment. Possible scattering and unwanted reflections off the surrounding surfaces are a result of these on-device waveguides which can limit the accuracy of data collected. To remedy this, micro lenses are designed to focus the light to reduce the scattering and surface reflections [7]. On-chip optical sensing also requires access to microtechnology and the ability to accurately incorporate it onto a microfluidic chip [8]. The on-chip design does allow for a more compact device and is cheaper to produce in the absence of expensive and high-powered equipment [8].

Off-chip techniques are much easier to incorporate to microfluidic devices as there is very little, if any, microengineering involved. The off-chip optical technology generally consists of larger high-powered equipment that requires special training and specific environments to operate. Off-chip optical devices require proper alignment by the user and can be much less sensitive than that of on-chip devices as more background interference can be collected in detection [8]. While this is less than ideal for micro-detection research, off-chip devices can be easily coupled with more sensitive equipment to reduce errors in data collection. Off-chip techniques can be used for sensing which includes probes, sorting and manipulation technologies. These methods generally require high powered lasers. Off-chip methods are not ideal as they require external alignment and tend to be less accurate [14]. The research discussed in this manuscript tests both on and off-chip approaches for optical integration to microfluidic technology.

Applications for optical data collection falls into two categories: measuring the change in light intensity and change in wavelength [13]. The change in light intensity measurements include absorbance, fluorescence and chemiluminescence and generally are conducted using macro scale optical technology. Absorbance measurements are some of the most widely taken measurements as they are easy to implement off-chip and can do so at a low cost. To increase accuracy and sensitivity for absorbance-based measurements, optical waveguides can be directly integrated onto the microfluidic device which eliminates discrepancy in alignment and minimizes background signals. Fluorescence is another common technique used and is more sensitive than absorbance measurements. Laser induced fluorescence provides the ability to focus on small regions (like a microchannel) while maintaining a high energy beam. Simpler methods for fluorescence measurements in microfluidics include implementing a laser emitting diode (LED) as the light source, as described in an experiment by Miyaki et al [19]. The benefit of the LED based method is that it requires lower power light sources that are cheaper and easier to obtain [8, 19]. A majority of measurements taken using the fluorescence based techniques do require labeling of the particles which can be undesirable as it limits the kind of particles that can be studied due to limited availability of the fluorescent particles and fluorophores that can be bound to particles. Chemiluminescence

is a highly sensitive method for optical measurements of particles using simple instrumentation and eliminates the need for an external light source. This method requires chemical regents to be mixed with the analytes on the device for proper detection which limits the types of samples that can be studied and increases the complexity of the microfluidic chip design [8]. Other methods that have been done with optics are measuring the change in the wavelength, phase or polarization. Changes in phase have been measured using "miniaturized interferometers and resonators for refractive-index-based detectors" as discussed by K. Mogensen and J. Kutter [13]. This is a much more sensitive technique but prone to inaccuracies caused by temperature and fluctuating wavelengths. Measuring changes in wavelength requires very precise and compact on-chip optics for light manipulation which allows for more sensitive measurements but are much harder to design and manufacture.

Miniaturized versions of flow cytometers are a common off-chip design used with microfluidic devices and have been developed to measure fluorescent scattering of cells. Flow cytometers work by shining laser light at a stream of particles and measure either the scattered light at various angles or fluorescent emissions. These flow cytometers can distinguish between populations within the same sample, obtain data of targeted characteristics of individual particles and measure the flow speed of particles using two lasers. These devices are reliable tools for analysis but are bulky, costly and require trained operators [3, 7].

Chapter 3

Microfluidics, Optical Apparatus and Samples

3.1 Introduction

The apparatus for the optical detection method integrated into this microfluidic research consisted of different microfluidic chips, microscopes and optical components used to collect and transmit light. The microfluidic channel was illuminated from below and the light was collected by either an objective lens or fiber optical cable that was then coupled into a photodiode (Optek OPF482, please see Appendix E for data sheet) operating in the photoconductive mode. A core diameter of 1 mm was chosen for the fiber optic cable as it allowed for a large area of light collection from the channel to improve the signal to noise ratio of the optical signal. The 1 mm optical fibers were already assembled with an ST connector to fit the photodiode which eliminated unnecessary purchasing and assembly time.

The two microfluidic devices used were a glass microfluidic device developed by Colorado State University (CSU) PhD candidate Jasmine Nejad and a printed circuit board (PCB) device developed by CSU graduate student Lakshmi Abburi. Each device used a variant method for detection to accommodate the different opacity of the materials of each device. This chapter outlines each experiment set-up and the types of samples used for testing the apparatus.

3.2 Microscope Set-Up

Two different microscope set-ups were used for this research. The first microscope included a stage with a micrometer mount which allowed the user to manually adjust the lateral position of the stage. The illuminated light source was either a blue fiber coupled LED or a white light lamp. The blue fiber coupled LED was used during tests with parasite eggs because a better camera image of the eggs was obtained due to biological tissues being more absorbent in the spectral range 400 nm to 500 nm [20, 21]. The white lamp was used at all other times as the opacity of the glass beads

were not wavelength dependent and the white light provided a better camera image than the blue fiber coupled LED. A beam splitter was placed after the objective lens to send light to a camera as well as to the photodiode. The first microscope bench set-up was located in the CSU laboratory and is shown in Fig. 3.1.

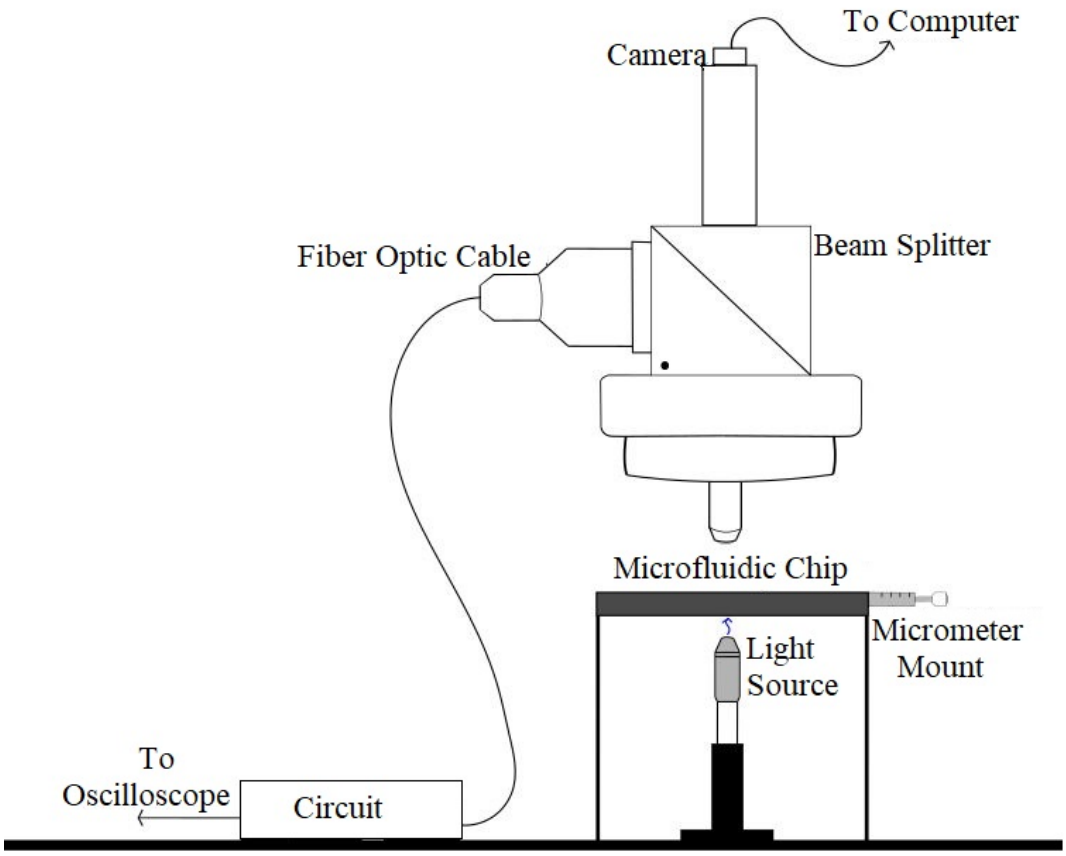

Figure 3.1: The bench set-up of the first microscope used for data collection.Two light sources were used during testing: one blue LED light coupled into a fiber optic cable and a white light lamp.

In March 2020, the severe acute respiratory syndrome coronavirus 2 (more commonly referred to as COVID-19) pandemic caused Colorado State University (CSU) to close campus and all laboratories. The remainder of this project was conducted remotely and the initial microscope set-up in the lab was no longer available and was replaced with a smaller, personal microscope. The second microscope consisted of a 20 W incandescent bulb illuminating the microfluidic channel from

below. The light was directly collected by the photodiode from the objective lens and fiber optic cable. The second microscope set-up is shown in Fig. 3.2.

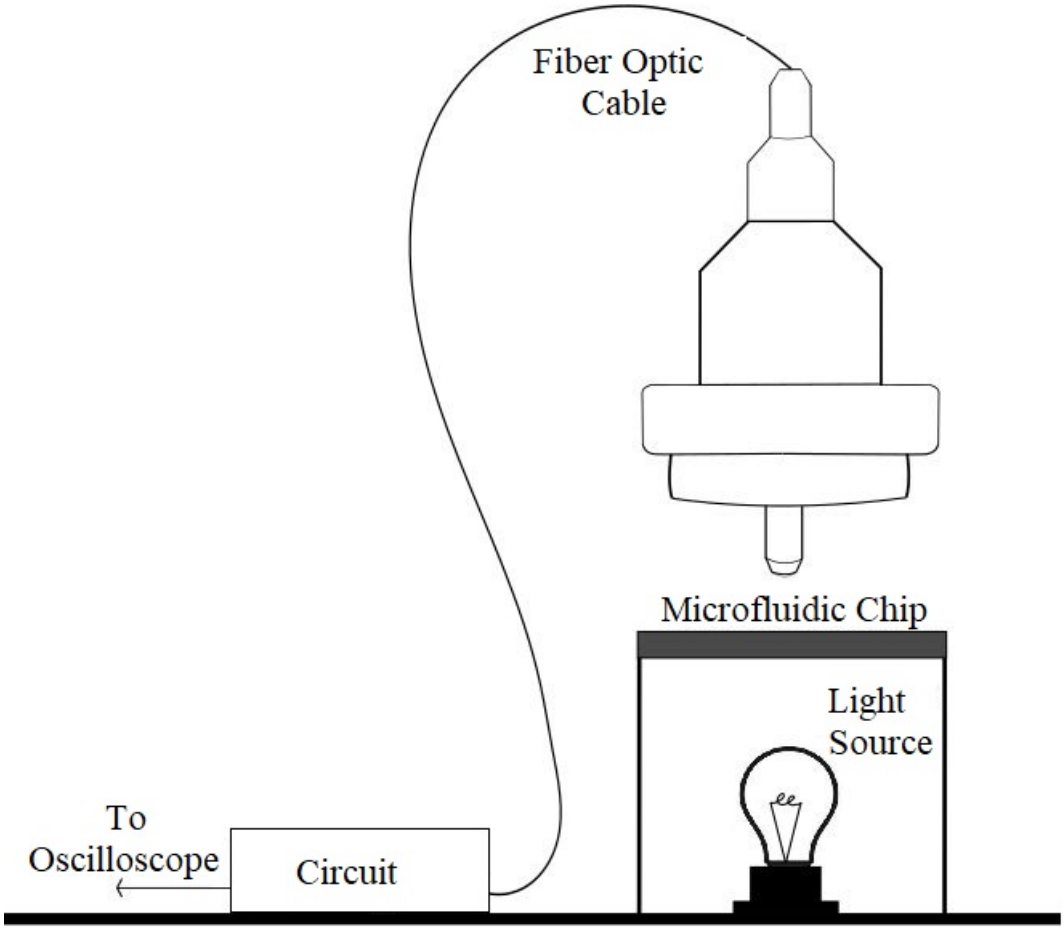

Figure 3.2: The bench set-up of the second microscope used for data collection. The illuminating light source on this microscope set-up was a 20 W incandescent bulb.

The glass microfluidic device needed to be modified to accommodate the smaller size of the second microscope. The device was modified by removing the exit tubing to fit between the objective lens and microscope stage. The working distance of the 4 $\times$/0.1 NA (numerical aperture) objective lens was found to be approximately 1.3 cm and the room required for the exit tubing lifted the glass device too close to the objective lens and out of this working distance. The device was lifted by 0.5 cm thick pieces of cork to allow the liquid to flow out of the channel unobstructed

by the stage. Lifting also alleviated possible pressure changes in the channel caused by the contact between the microscope stage and exit of the channel. The removal of the tubing and the added lift did not affect the fluid flow through the channel or the process of data collection. The modified MIC device is shown in Fig. 3.3.

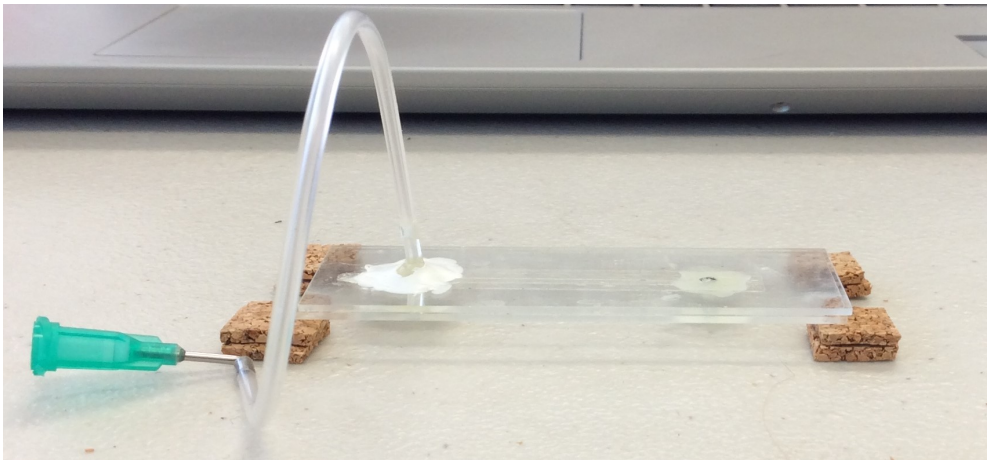

Figure 3.3: The modified glass MIC device used on the second microscope set-up. The exit tubing was removed, and the chip was raised to allow liquid to flow out of the channel without any obstruction and pressure changes caused by the contact with the microscope stage.

The two bench set-ups gave insight on modifications required when using this design of a simple optical detector on changing systems. These adaptations are discussed more in Chapter 6 of this manuscript.

3.2.1 Optical Considerations

The intensity change of the light collected by the photodiode was dependent upon the optical equipment being used. Each microscope set-up had different magnification and NA values. The magnification and NA determined the resolution of an image and the depth of focus which could alter the intensity of the light collected. The fiber optic cable was placed at a fixed distance from the objective lens and had no additional lens to focus all the light into the cable.

On the smaller at home microscope set-up, the vertical translation of the stage had a significant effect on the level of the voltage recorded by the circuit. As the distance between the objective lens

and stage changed, the baseline voltage changed creating an offset between the reference voltage on the comparator and the incoming signal. The second microscope set-up had an additional lens in the aperture on the microscope stage that was believed to have contributed in the change of the baseline voltage. This offset compromised the ability for the comparator to detect any changes in voltage.

For the 4×/0.1 NA objective lens used on the second microscope set-up, the total distance of stage translation was approximately 3.18 cm and the total distance between the objective lens and the light bulb used for illumination was an unchanging 11 cm. It was found that as the the distance between the the stage and objective lens decreased, the baseline voltage of unobstructed light increased. A change of approximately 124 mV was recorded for the full vertical translation the microscope stage. This behavior is shown in Fig. 3.4.

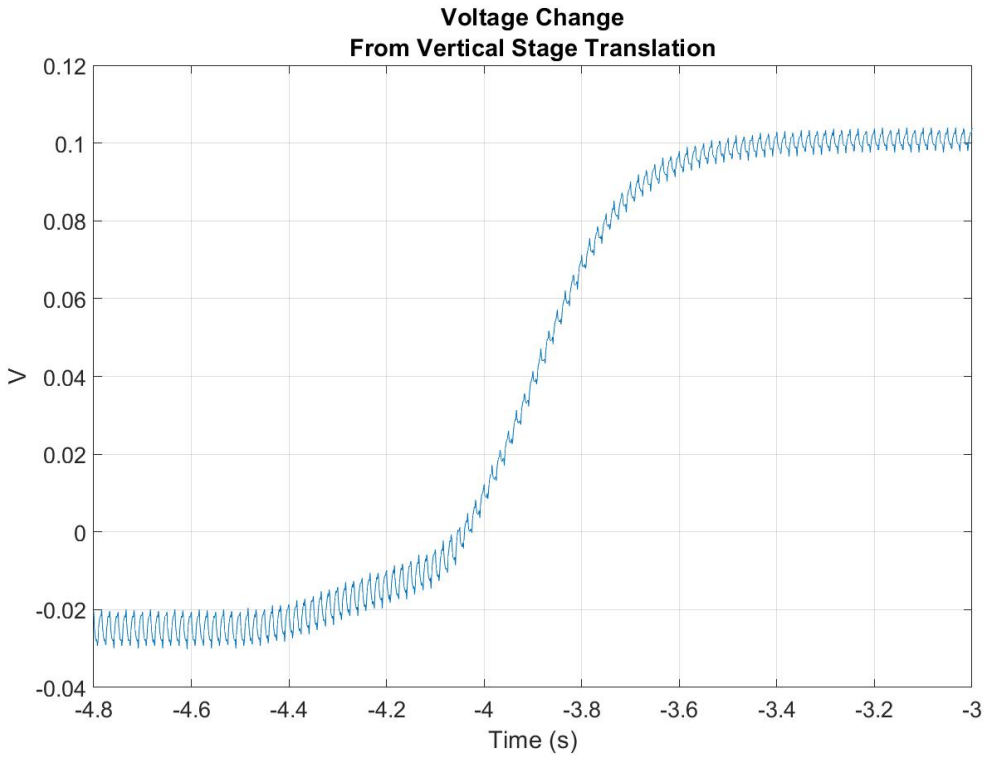

Figure 3.4: Voltage change that is linearly related to the power of the light entering the photodiode as the distance between the microscope stage and objective decreased. A change of 124 mV was recorded for a full vertical translation of 3.18 cm of the microscope stage. The increase in voltage corresponds to the stage moving closer to the objective lens. This was enough to compromise the ability of the comparator to detect changes in voltage.

A test of the optics was done by measuring the change in voltage at various distances between the objective lens and microscope stage. The data taken supports the trend in Fig. 3.4 that a smaller separation between the objective lens and the stage yields a higher baseline voltage. The voltage data recorded at various separation distances of the objective lens and microscope stage are shown in Fig. 3.5.

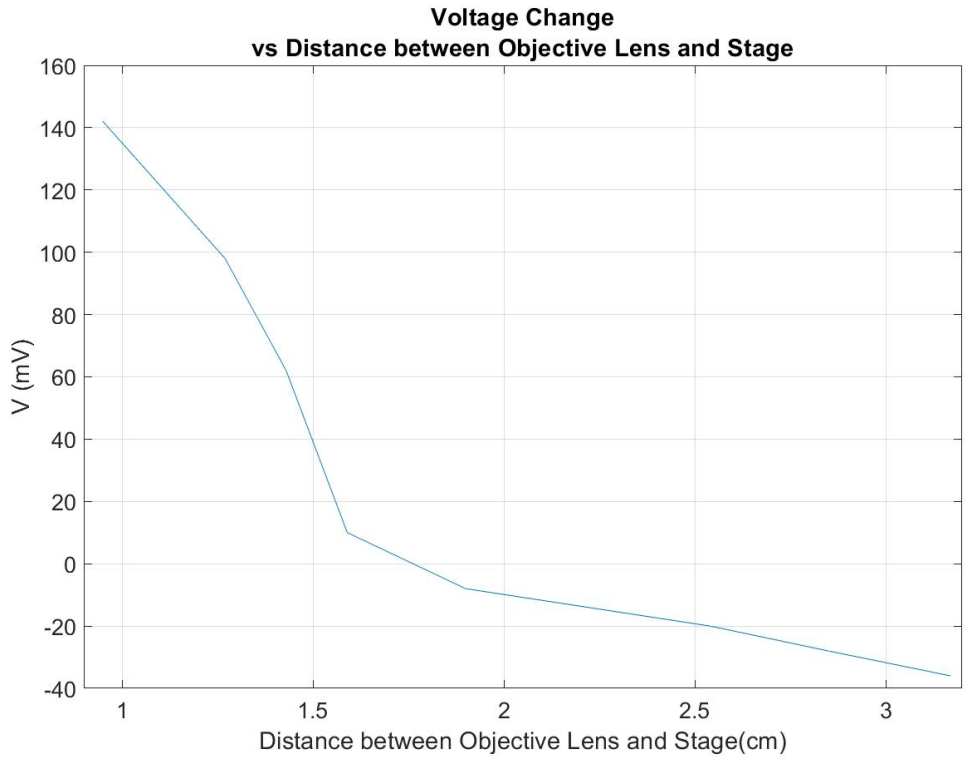

Figure 3.5: Voltage values recorded at various separation distances between the objective lens and the microscope stage. The smaller the separation between the lens and the stage, the higher the baseline voltage value. This plot demonstrates a full vertical translation of 3.18 cm of the microscope stage. The output voltage in this plot is recorded from the output of the transimpedance amplifier of the circuit which is discussed more in Section 4.2.

The glass device was then moved through the light detection area on the microscope to determine if the adhesive material along the channel had any effect on the baseline voltage. As the glass device passed through the light, there was a decrease in voltage when the edges of the glass and edges of the adhesive passed through the beam. This caused the light to scatter decreasing the

amount of light entering the objective at that moment. This change in voltage as the glass device passed through the beam is illustrated in Fig. 3.6.

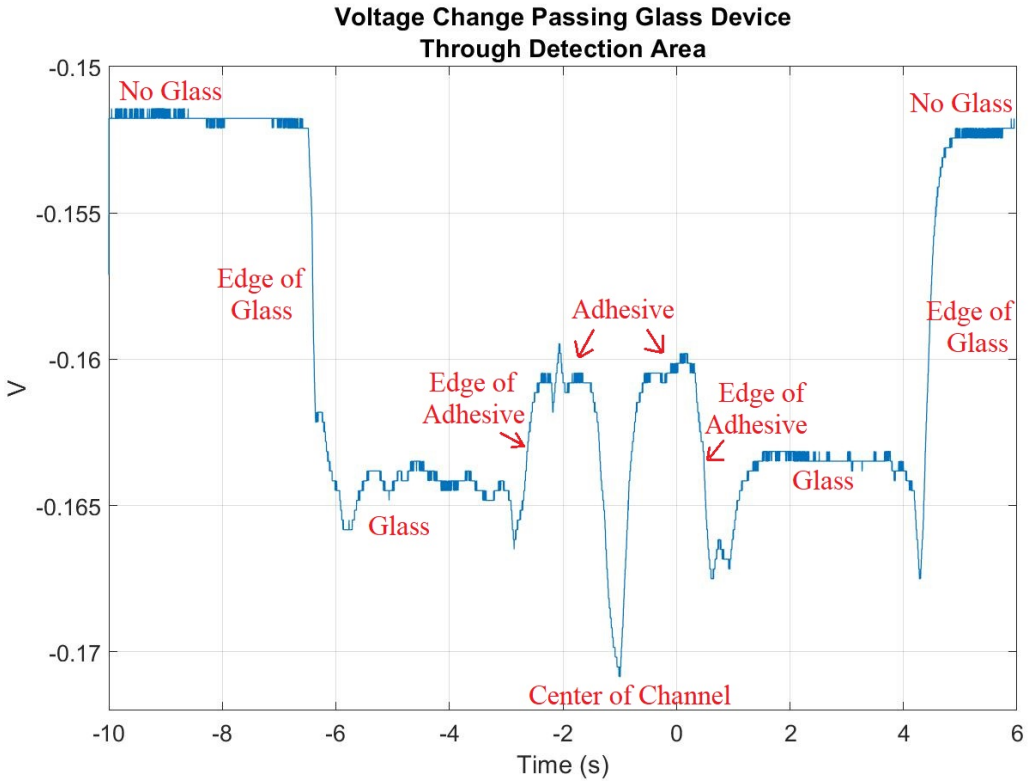

Figure 3.6: Baseline change in voltage as the glass device was passed through the optical detection area. A decrease in baseline voltage occurred at the edges of the glass and edges of the adhesive causing the light to momentarily scatter and thus not all the light was collected by the objective lens.

To avoid baseline changes in voltage due to the optics, the microfluidic channel had to be aligned with the detection area and the stage height had to be set so the channel was imaged by the objective lens onto the fiber. This helped to avoid possible scattering from the edges of the adhesive tape. To do this, the height of the stage was set to a separation distance of 1.27 cm between objective lens and microscope stage which was at the working distance of the objective lens. A focus was found by back propagating laser light through the optical fiber and onto the microscope stage. The microscope stage was then adjusted to where the back propagated light

spot came to a focus. The inside of the microfluidic channel was positioned in that focused area so the objective collected all the light coming from the channel.

The change in the baseline voltage shown in Fig. 3.4 and 3.5 was a key factor in accurate operation and detection of the trigger circuit used in this research. As the distance between the objective lens and microscope stage changed, this baseline voltage changed which resulted in an offset between the inputs on the operational amplifier (op-amp) comparator circuit. The offset due to the changing height of the microscope stage, along with other additional factors contributing to the offset, were alleviated by filtering the signal before it was input to the comparator. The effect on the data, and the design steps taken to eliminate the offset between signals is discussed in detail in Chapter 5 of this manuscript.

3.3 Glass Microfluidic Device

The glass microfluidic device was fabricated using two glass microscope slides bonded together by a microfluidic channel. Complete fabrication details of the glass MIC device, including electrodes is outlined in detail by J. Nejad et al [9]. The transparent properties of the glass drove the design for an off-chip optical detection method. The glass microfluidic chip required no modifications to apply the optical detector as light could easily be shone through the glass and collected by a microscope.

The foundation of the glass MIC device was assembled based on designs developed by Jasmine Nejad [9] and composed of three main components: two glass microscope slides, a laser cut double-sided adhesive channel and flexible polymer tubing. Exit and entrance holes for the channel were drilled onto opposing sides using a diamond coated drill bit. The polymer tubing was aligned to the drilled holes and glued to the slides. Once the glue holding the tubing to the slides dried, the laser cut adhesive was aligned with the holes and adhered to one of the slides. The glass slides were then secured together using the laser double-sided adhesive channel. The construction of the device is outlined in Fig. 3.7.

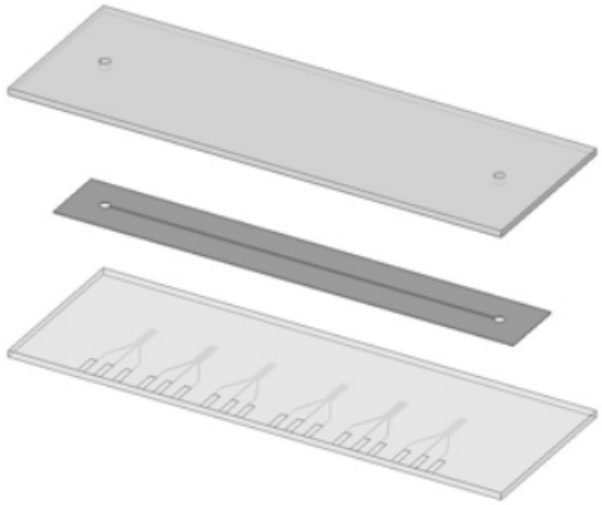

Figure 3.7: A CAD layout of the three main layers of the glass MIC device: electrode slide (bottom), double-sided adhesive channel (middle) and slide with drilled entrance and exit holes (top). For testing the optical device, the bottom slide was generally a plain glass slide without electrodes. The device tested for the optical technique had entrance and exit hole drilled onto opposing slides instead of the same slide as shown in this image. Image reproduced from [9] created by Jasmine Nejad.

For the purpose of testing the optical detection technique for the glass slide, the bottom slide of the device was generally a plain glass slide without electrodes. The addition of the electrodes had no effect on the functioning of the optical detector.

3.4 PCB Microfluidic Device

The microfluidic PCB device was designed by CSU graduate student Lakshmi Abburi. The PCB device consisted of two printed circuit boards joined together by a double-sided adhesive channel. These PCBs were manufactured by a third-party company and then assembled with the double-sided adhesive channel and polymer tubing in the lab. The components of the PCB MIC chip and completed device are shown in Fig. 3.8.

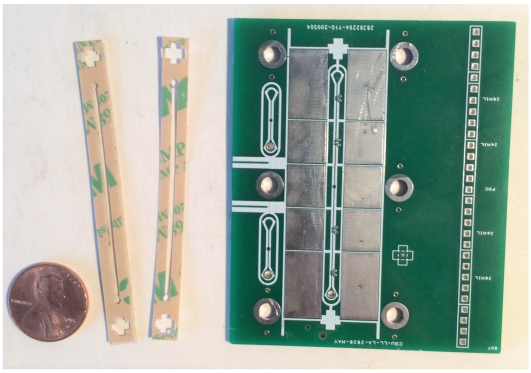

(a)

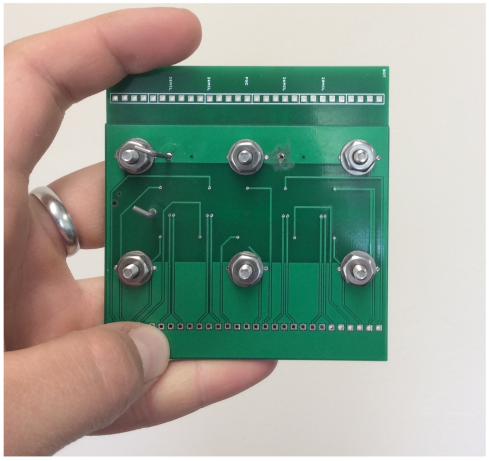

(b)

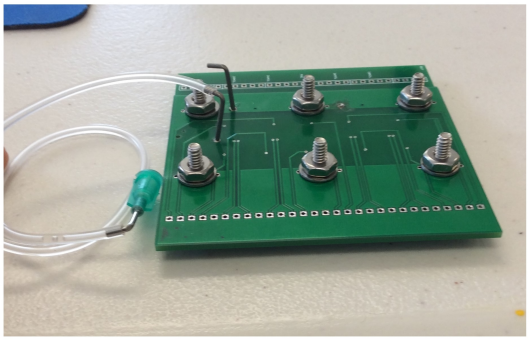

(c)

Figure 3.8: (a) The PCB chip consisted of a double-sided adhesive microfluidic channel and two PCB boards. Penny shown for scale. (b-c) Assembled PCB microfluidic device. PCBs and parts shown were provided by Lakshmi Abburi.

The opacity of the boards required the optical methods to be incorporated on-chip as opposed to the off-chip method described in Section 3.2 and 3.3. Modifications to the original PCB design were required to successfully implement optical detection technology onto the chip. Holes with a diameter of 0.3 mm were designed to align with the channel on each board to allow for the integration of optical fibers used for illumination and detection and were drilled during the manufacturing process of the boards.

3.4.1 Optic Connections

To use optical detection methods on the PCB microfluidic device, the optical approach was altered due to the opaque nature of the the PCB. Plastic optical fibers (POF) were used for light collection on this device and were attached directly to the microfluidic device through the 0.3 mm drilled holes.

The optics were added by aligning and inserting a 0.25 mm diameter POF cable into each of the 0.3 mm diameter drilled holes above the channel. The POF cables were added to the boards before the adhesive channel was secured on the board. POF cables were chosen over glass fiber optic cables for their user-friendly qualities regarding cutting and melting. This allowed for easy at-home modifications to be done without special equipment. Three methods were tested to determine the most effective way to secure the POF to the PCB. The first method was done by gluing the fiber directly into the hole. Tape was placed along the channel side of the board to inhibit the spread of glue from the hole onto the board and to ensure that the edge of the fiber set up flush to the board's surface. A small amount of glue was added to the top of the board and the board was set to dry channel side up to use gravity to prevent glue from settling onto the channel side. The end of the fiber was successfully secured into the hole and flush to the board. Under microscope inspection of the hole incorporating the fiber onto the board, it was found that the glue leaked onto the channel side and that the end of the fiber had been covered in glue yielding a non-uniform surface shown in Fig. 3.9 (a). This non-uniformity could cause unwanted refraction and obstruction of the light in the channel which would not be conducive for detecting micron sized particles.

The second method was done by placing the POF through the hole and melting it back until the plastic expanded (or bubbled). This allowed the cable to rest in the hole on the channel side of the board. The melted plastic would not adhere to the PCB so a small amount of glue was added and dried the same as described above. The expanded plastic on the channel side of the board served as a block to prevent any leakage of glue onto the board. The expanded plastic was then cut using a hot wire knife to make the POF flush with the PCB surface. Under microscope inspection, the terminal end of the POF was not obstructed by a mask of glue as shown in Fig. 3.9 (b). The

non-uniformity of the surface of the hole in Fig. 3.9 (b) is from the glue filling in the 0.05 mm gap between the fiber and the hole and not caused by uneven melting. In both cases, the end of the POF could not be polished as that could have altered the flat surface of the board which would lead to leaks in the channel.

The third, and most effective method, was done by using the tip of a soldering iron to melt back the POF into the hole. This method was able to melt the POF completely flush with the surface and eliminated the need for glue to hold the POF into place as the melted POF adhered to the board. The microscope image of the POF in the hole using the third method is shown in Fig. 3.9 (c).

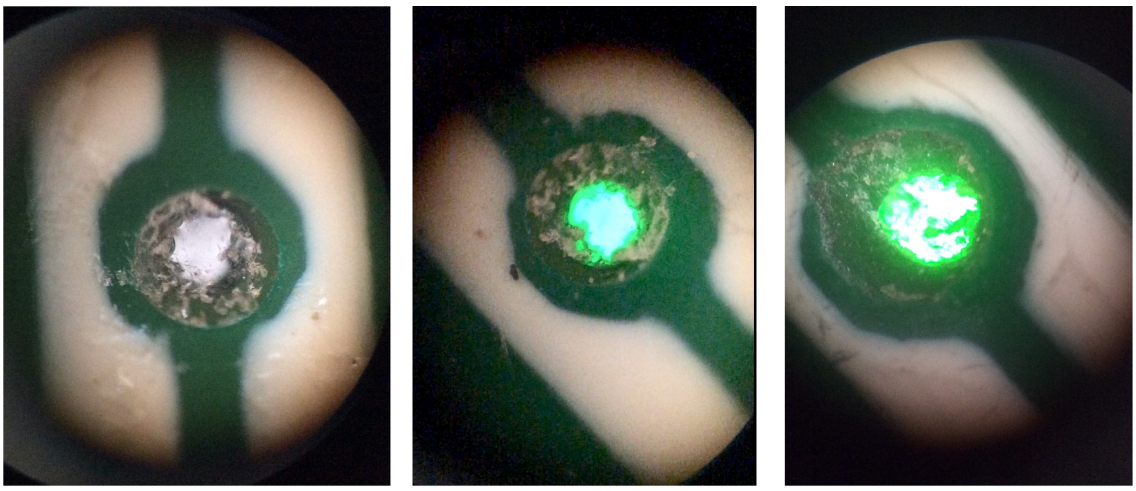

(a) (b) (c)

Figure 3.9: The integration of the POF cable for the three different methods (a) glued into place, (b) burned back and secured into place with super glue and excess plastic removed using a hot knife and (c) soldering iron used to burn POF flush with the board. The method using the soldering iron provided the most uniform and unobstructed terminal end of the POF.

The output light from the POF secured to the board using the soldering iron method was inspected for uniformity by projecting the laser light shone through the cable onto a white sheet of paper. The 0.25 mm diameter size of the POF made it difficult to project and inspect an image. To obtain an image that was large and bright enough to inspect, the maximum distance between the terminal end of the cable and paper was approximately 2 cm. Fig. 3.10 (b) shows that the light

leaving the POF was uniform and circular which verified that the terminal end of the fiber had no obstructions that could cause false detections or block events.

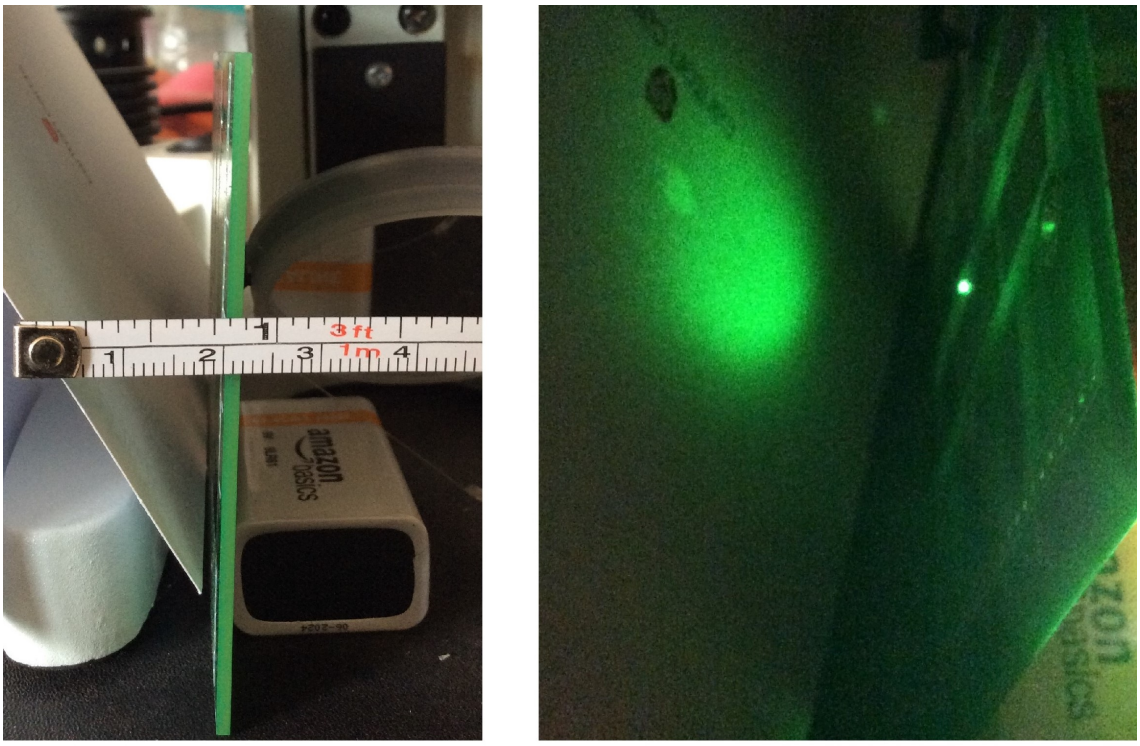

(a) **(b)**

Figure 3.10: (a) A maximum distance of 2 cm between the terminal end of the fiber and paper was used to inspect the uniformity of the image output of the solder burned POF. (b) The output of the POF was uniform and circular verifying that there were no obstructions on the terminal end of the fiber. The tear drop shape in the photo is due to the backward slant of the paper so a photo of the image could be taken.

The breakdown of the assembly of the POF onto the PCB board is illustrated in Fig. 3.11.

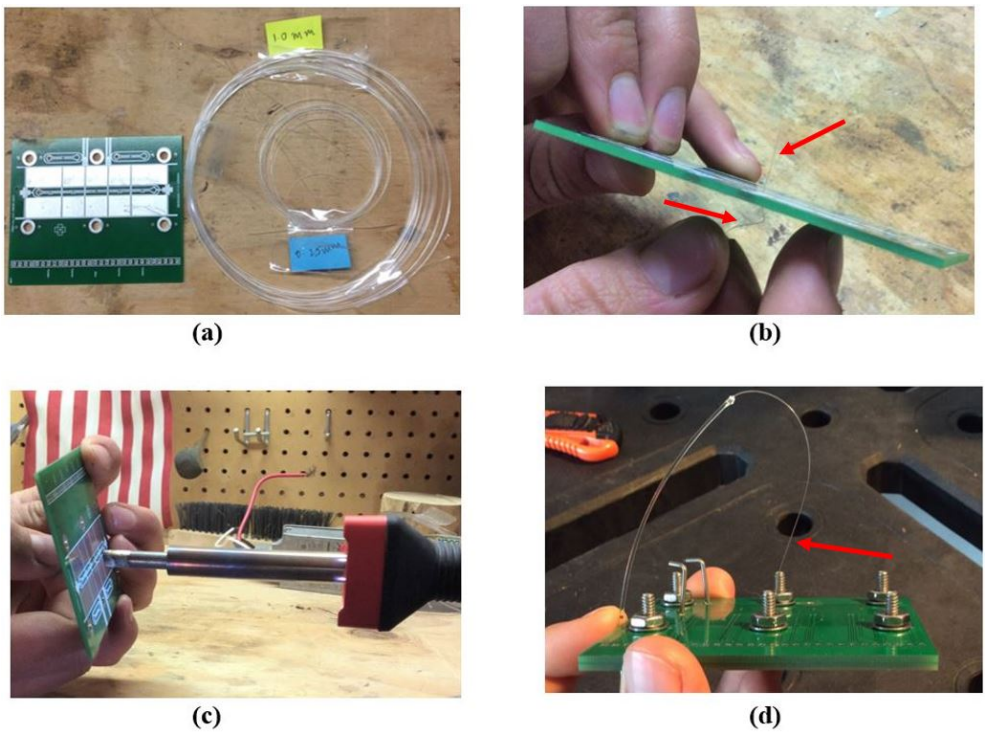

Figure 3.11: (a-c) Assembly of the POF cable onto the board. (a) Materials for POF integration onto the PCB. A 0.25 mm cable was used to insert into the hole on PCB and the 1 mm was inserted into the photodiode. (b) The 0.25 mm end inserted through the hole and (c) melted back into the hole using a soldering iron. (d) Device with assembled POF cables. Red arrows point to the POFs inserted into the PCB.

For the photodiode to better collect the light from the fiber in the absence of an ST connectorized fiber, a 1 mm POF cable was desired for ease of alignment into the photodiode. It was more difficult to guarantee the accuracy of manually aligning a 0.25 mm diameter cable into the ST connector on the photodiode than it was with a larger fiber core diameter. The 0.25 mm cable was melted to a 1 mm section of POF cable that was then fed into the photodiode. The soldering iron was used to melt and smooth the two POF cables together. This did not decrease the quantity of light entering the photodiode, but it did decrease the structural integrity of the fibers at the junction. Extra care was required when handling the melted cables. The junction of the melted 0.25 mm and 1 mm cables is demonstrated in Fig. 3.12.

(a)

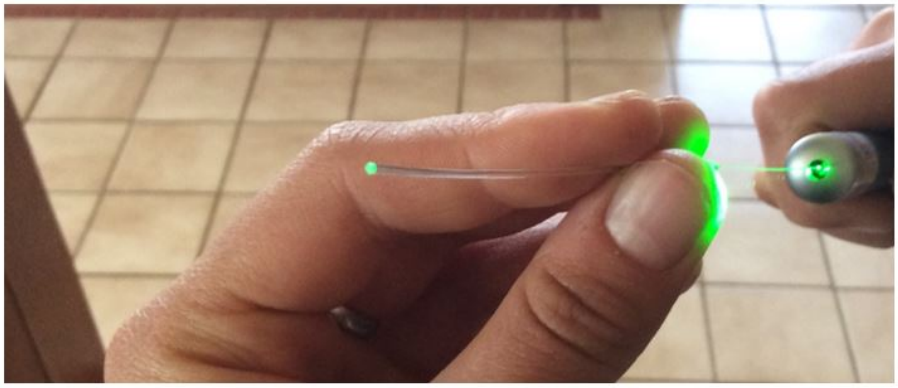

(b)

Figure 3.12: (a) The 0.25 mm and 1 mm POF cables melted junction. The two cables were melted together via the tip of a soldering iron. (b) This did not decrease the quality of light entering the photodiode, but it did decrease the structural integrity of the fibers at the melted junction.

Under microscope inspection, it was noted that the drilled hole was offset by 0.1 mm with respect to other features on the PCB. The offset of each hole could cause a misalignment of the holes when the PCBs were secured together which could lead to either no detection of events in the channel or create a very small detection area. For POF alignment reference, Fig 3.13 (a) shows the unobstructed hole compared to the fiber integrated holes on the PCB.

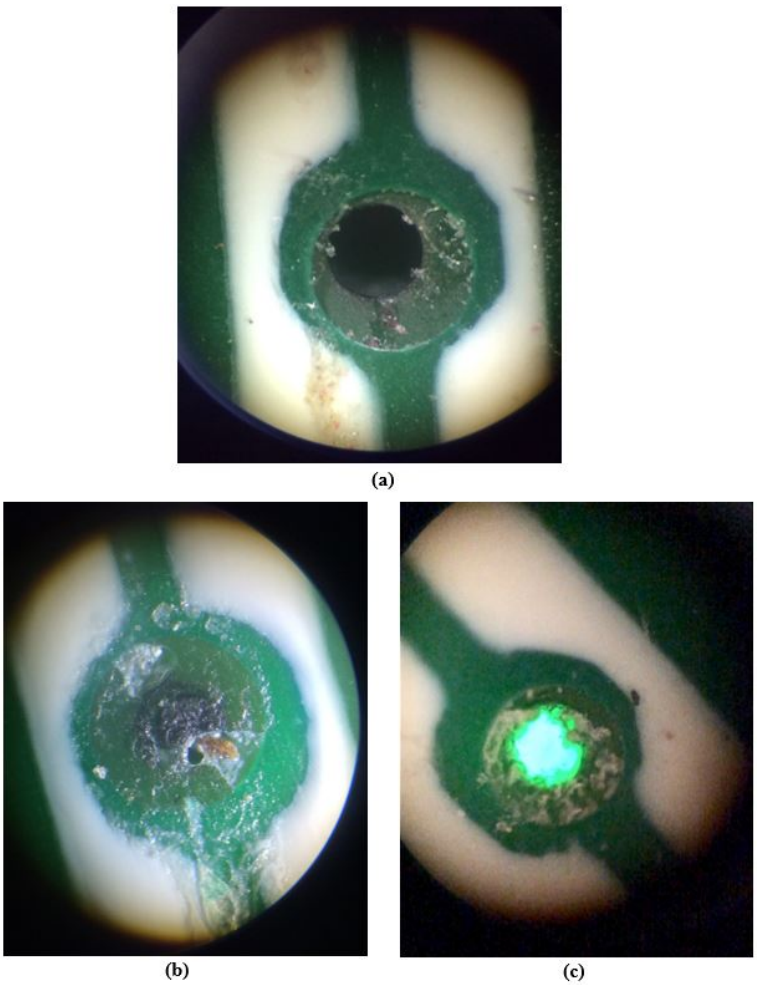

Figure 3.13: The end of the POF on the channel side of the PCB board when (a) no fiber was secured into the hole, (b) the fiber was glued into the hole and (c) when it was melted into the hole with a green laser shining through the cable showing that the POF end was unobstructed.

3.5 Samples for Testing

Multiple types of samples, including glass beads, sewing thread, metal shavings and fishing line were used during testing of the optical apparatus and detection circuit. The initial tests for the glass microfluidic device were done using glass beads 63-75 μm diameter mixed into a saline solution with a concentration of 50 beads/μL [9]. This solution was pushed through the channel at a rate of 25 μL/minute using a syringe pump.

The move to the second microscope bench set-up posed some challenges and required modifications to how the trigger system was tested. The microscope bench set-up in the CSU lab with

simultaneous video feed to optic measurements, allowed the user to confirm when objects of interest were flowing through the detection area in the channel which would then be referenced to the signal change seen on the oscilloscope. The sensitivity and functionality tests of the circuit were able to be conducted using a glass bead/saline solution to accurately simulate parasite eggs flowing through the channel. Without image verification on the second microscope set-up, it was difficult to use the glass bead/saline solution for testing purposes. For testing on the glass device, a 0.33 mm diameter sewing thread was passed in and out of the detection area to simulate a small moving particle. The sewing thread was chosen as it was the smallest diameter object available that allowed easy manipulation for speeds and time for testing to mimic beads passing through the channel. The thread at 0.33 mm in diameter was approximately 4 times larger than a typical strongyle-type parasite egg at 65-100 μm in size [18]. The length of the thread spanned the entire diameter of the detection area which is contrary to the space a strongyle-type egg would occupy. The decrease in voltage from the thread, which was amplified by an inverter with gain -15, fell within the range of the changes in photocurrent recorded from the glass bead which confirmed the thread to be an adequate substitute for glass bead tests in the microfluidic channel. These tests are discussed in Chapter 4 of this document.

The optics on the PCB microfluidic device could not be tested using the sewing thread method stated above. Tests using glass beads could not be used on the PCB device for the same reason they could not be used for the glass device. Multiple samples were tried including a metal shaving from a steel horseshoe nail taken from a metal rasp, fishing line with a mark on the line and fishing line with a dried spot of paint. The metal shaving was tested by moving through the channel using and external magnet, but proved to be difficult and yielded questionable results. The methods and results for the metal shaving are discussed in Appendix D. The marker spot on the fishing line would smear and rub off and also provided inconclusive results. The dried paint spot proved to be the most accurate test of the optics for the PCB device. The paint spot, approximately 0.6 mm wide, was dried onto the clear fishing line which spanned the entire length of the channel. The ends of the fishing line were fed through the entrance and exit holes of the PCB device and the

paint spot was pulled in and out of the detection area using the exposed ends of fishing line. An illustration of the PCB test set-up is shown in Fig. 3.14.

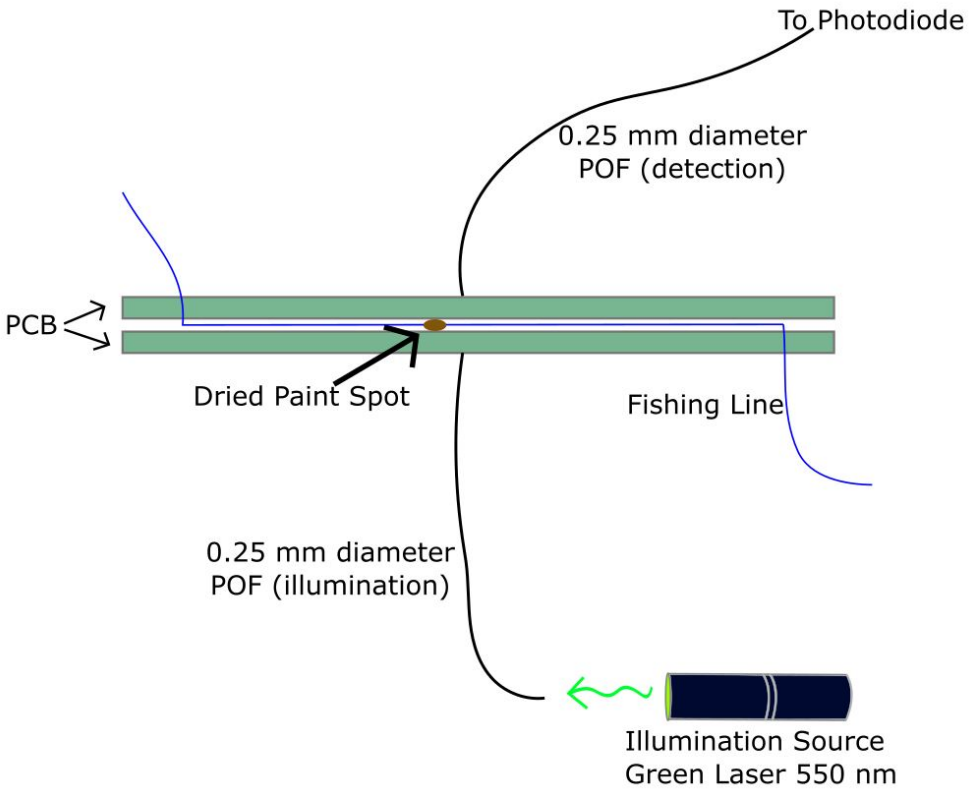

Figure 3.14: Illustration of the set-up used to test the optical apparatus on the microfluidic PCB device. A spot of paint that spanned the width of the channel was dried onto fishing line and place into the channel. The ends of the fishing line were threaded through the entrance and exit holes of the device and were used to externally pull the dried paint spot in and out of the detection area.

As the paint spot passed through the optical detection area it completely blocked the light which was not an accurate simulation of micron sized particles in the channel, but was a testable sample that provided conclusive results. The dried paint spot imaged next to the 0.3 mm detection hole in the PCB is shown in Fig. 3.15.

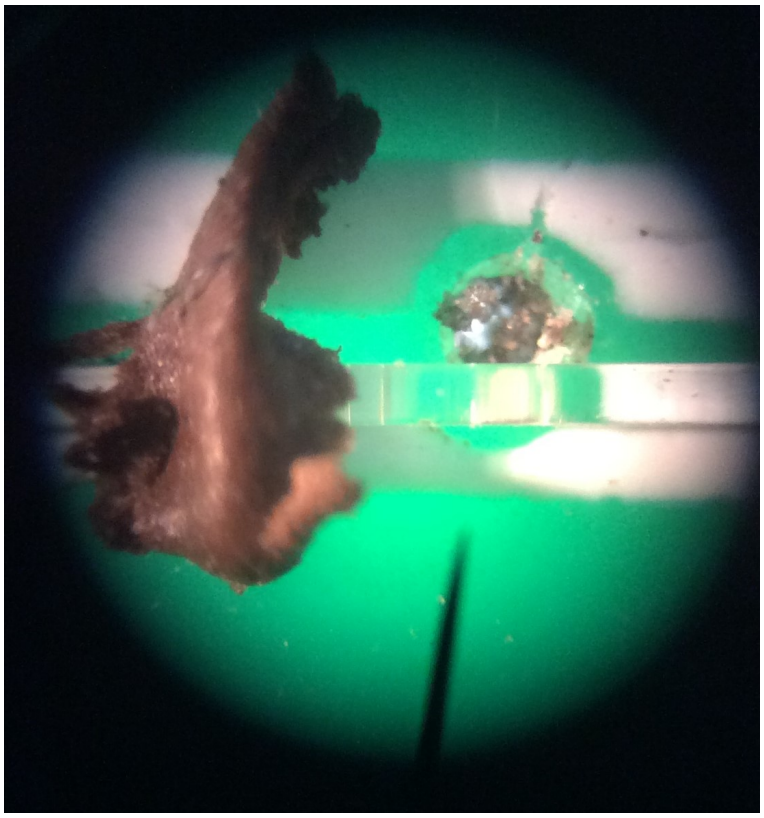

Figure 3.15: Paint spot dried onto fishing line that was used for optical tests on the PCB device. The paint spot was pulled through the channel using the external leads of the fishing line.

Smaller objects that would better mimic the size of glass beads or strongyle-type eggs, such as the metal shavings were available but difficult to collect, place in the channel and manipulate. Using the dried paint spot on the fishing line was done as an initial test to confirm that the integrated optics could detect objects moving inside the microfluidic channel on the PCB device. The sensitivity of the on-chip optical detection method could not be accurately quantified as the test sample of the dried paint spot blocked most or all of the light in the channel while pulled through. To accurately test if additional optics would be needed to detect objects, tests using flowing micron sized particles need to be conducted.

Chapter 4

Light Detection Circuit

4.1 Introduction

The change in light intensity due to an object passing through a microfluidic channel can be used as a trigger signal or marker to improve data acquisition techniques. By utilizing a light detection circuit, changes in photocurrent were amplified and processed in order to be used for the trigger circuit discussed in Chapter 5. This chapter outlines the design of the transimpedance amplifier and other amplification techniques that were used to modify the the signal from the microfluidic channel. Test results of the circuits are discussed in Section 4.4 of this chapter using the samples presented in Section 3.5.

4.2 Transimpedance Amplifier

The incoming light signal generated a photocurrent that was passed through a transimpedance amplifier (TIA), which converted the photocurrent to a voltage with some gain measured in units of V/A. The gain of a TIA is determined by the value of the feedback resistor, and in this design a resistor value of 10 MΩ was chosen. The current output of the photodetector was expected to be on the order of nano-amps so the large valued feedback resistor was used to obtain an output voltage of approximately 10 mV. The gain of the TIA was calculated by

$$R_f = \frac{V_{out}}{I_{in}} \tag{4.1}$$

A resistor value of 10 MΩ was sufficient to amplify and convert a 1 nA photocurrent to 10 mV. A schematic of the first design of the TIA is shown in Fig. 4.1.

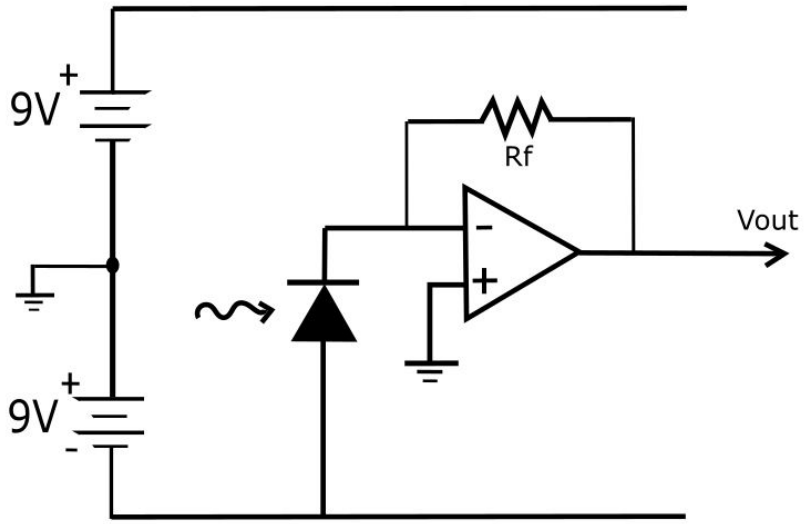

Figure 4.1: Schematic of the first design of TIA showing the photodiode in photoconductive mode at 9 V. The feedback resistor had a value of Rf = 10 MΩ.

The functionality of the TIA was tested by inputting the light signal from the microscope to a photodiode. This photodiode was operated in photoconductive mode at 9 V and was connected to the inverting pin of the op-amp. The op-amps used in this ciruict are LM358 from from Texas Instruments (please see Appendix F for data sheet) . A benchmark test was done to determine the change in voltage resulting from an absolute change in light entering the photodiode. The light entering the photodiode via the microscope objective lens was completely blocked using a business card, and it was determined that the TIA responded to the change in photocurrent to produce a change in output voltage of approximately 20 mV. This absolute change was initially recorded using a multimeter and when inputted to the oscilloscope the change in voltage was difficult to distinguish above high frequency oscillations present on this signal. Changes less than 20 mV would be obscured by these oscillations and not be useable for a trigger-generating circuit.

4.2.1 Oscillation Suppression

The high frequency oscillations observed on the output signal of the TIA were suppressed using capacitors in parallel with various parts of the circuit. To suppress any oscillations that may

be coming from the power supply, by-pass capacitors, Cb, with values of 0.1 μF were added in parallel with each battery. Oscillations in the photodiode current were suppressed using feedback capacitors, C1 and C2, added in parallel to the feedback resistor, Rf, of the TIA. Capacitors in parallel with a feedback resistor serve as a short circuit to high frequency oscillations to reduce or eliminate oscillations on the output. Modifications made to the TIA to suppress high frequency oscillations are shown in Fig. 4.2.

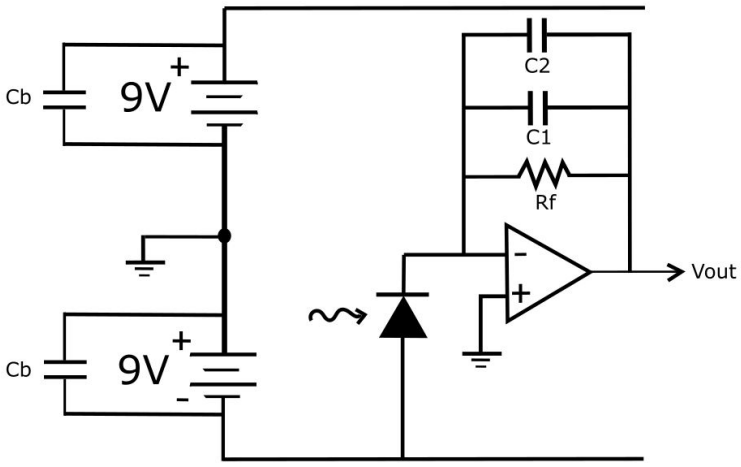

Figure 4.2: Final TIA schematic including two by-pass capacitors, Cb, each with a value of 0.1 μF, two feedback capacitors with values of C1 = 10 nF and C2 = 100 pF and a feedback resistor, Rf, with a value of 10 MΩ.

A single 1 nF feedback capacitor was placed in parallel with the feedback resistor and the high frequency oscillations were recorded to be approximately 50 mV peak-to-peak as shown in Fig. 4.3 (a). The 1 nF feedback capacitor was replaced with a higher valued capacitor of 10 nF which further reduced the high frequency oscillations to 7 mV shown in Fig. 4.3 (b). To further suppress these oscillations, a second feedback capacitor with a value of 100 pF was added in parallel with a 10 nF capacitor and feedback resistor. This reduced the high frequency oscillations to approximately 2 mV as shown in Fig. 4.3 (c).

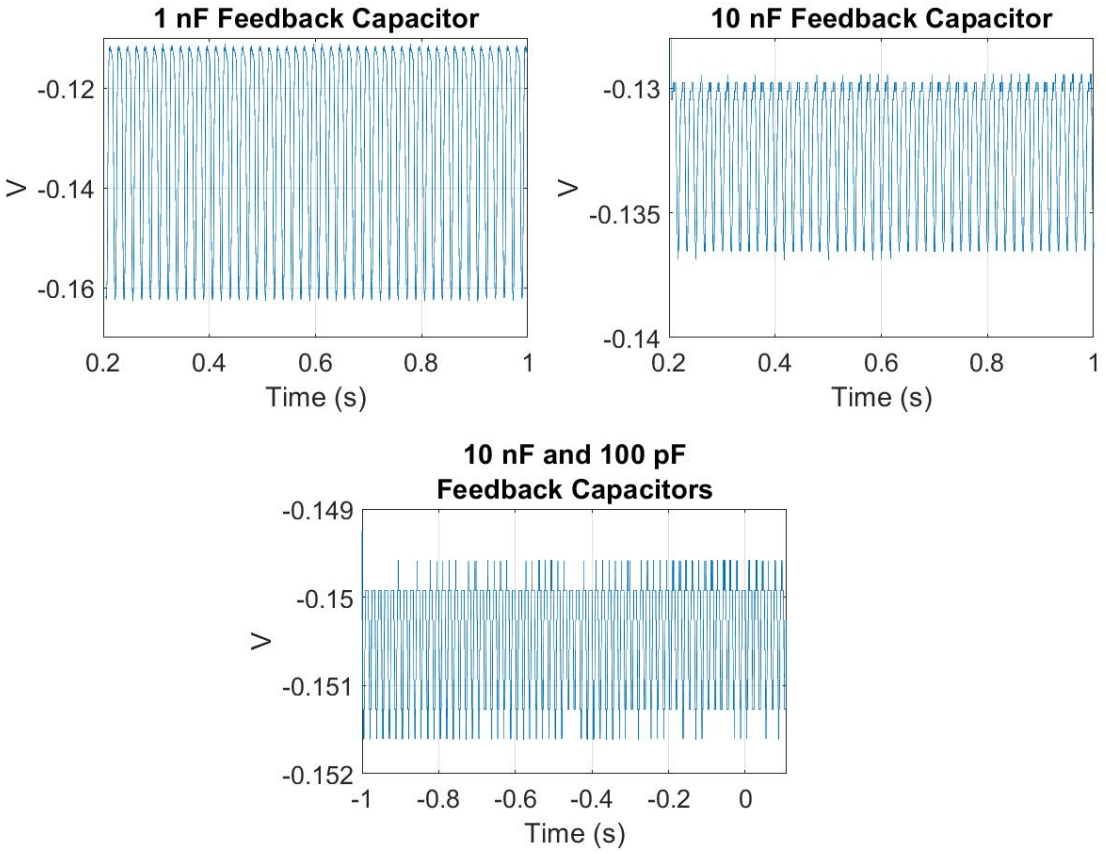

Figure 4.3: High frequency oscillations after the addition of (a) single feedback capacitor of value 1 nF yielding 50 mV oscillations and (b) single feedback capacitor of value 10 nF yielding 7 mV oscillations and (c) two feedback capacitors of values 10 nF 100 pF yielding oscillations of 2 mV. Approximate frequency for oscillations in (a-c) is 60 Hz.

The total feedback capacitance of 10.1 nF was chosen because it suppressed the oscillations while maintaining the small changes in voltage from glass beads. While a larger total feedback capacitance could measurably suppress all the oscillations, it also suppressed any 1-5 mV change in voltage resulting from a glass bead. These oscillations could have been due to parasitic oscillations which occurs when the output of the amplifier is coupled into the input. This coupling can cause mutual inductance between the input and output which causes a changing magnetic field and thus oscillations on the output. The frequency of oscillation shown in Fig. 4.3 was around 60 Hz which is the standard frequency for domestic electrical outlets and wiring in the United States. This means an additional cause of these oscillations could be from the electrical wiring in the lab. The

feedback capacitors were added to allow these higher frequency oscillations to be bypassed through these capacitors. With the combination of the by-pass capacitors and the two feedback capacitors, small changes in light were distinguishable above the high frequency oscillations. When the op-amp comparator was implemented into the circuit design, the original photodiode used for the experiment stopped functioning and was replaced with a brand new component. The oscillations were almost eliminated with the addition of the new photodiode so some of the oscillations on the signal could have been due to the break-down of the internal components of the older photodiode.

4.3 Signal Amplification

The voltage output of the TIA had to be manipulated by an inverting amplifier and filters to create a strong enough signal that would trigger the comparator when an egg or bead passed through the channel. When the light was obstructed, the output voltage of the TIA decreased so a change in the polarity of the signal was required for the comparator to output "HIGH" when it detected a change in voltage that was greater (not less) than the reference voltage. An explicit value of amplification was not necessary for the overall function of the circuit so the inverting amplifier was designed with a gain of -10 (and later -15) to easily confirm on an output signal. A schematic of this circuit is shown in Fig. 4.4.

The gain was achieved by using an input resistor, Rin1, of 1 kΩ and a feedback resistor, Rf1, of 10 kΩ. This configuration sufficiently inverted and increased the magnitude of the voltage signal inputted into the comparator. In later iterations of the circuit design, the gain on the inverting amplifier was changed to be -15 using a feedback resistor, Rf1, of 15 kΩ. This change was made because the baseline voltage of unobstructed light was variable on the second microscope due to the different optics and stage height (discussed in Section 3.2.1) which caused a greater offset between the signal and reference voltage on the comparator. A higher gain helped compensate for this offset. A gain of -15 was chosen as any larger gain resulted in a failure of the amplifier to output any signal.

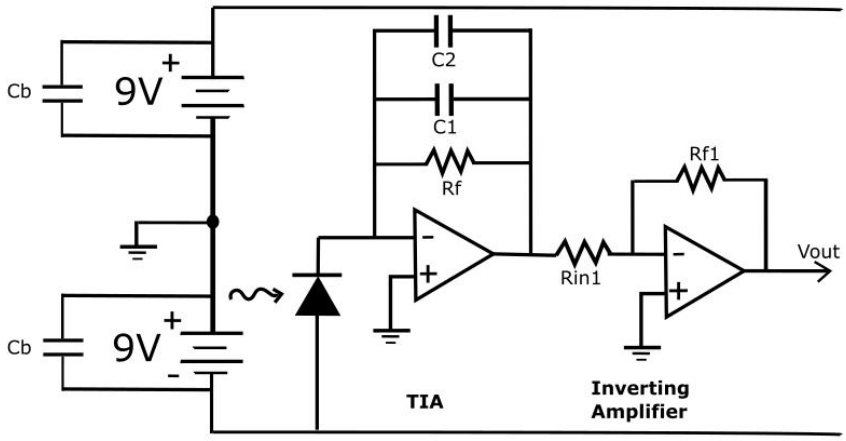

Figure 4.4: Schematic of the TIA and inverting amplifier circuit. Values for Rf, Cb, C1 and C2 are the same as presented in Fig 4.2 with added components Rin1 = 1 kΩ and Rf1 = 10 kΩ (15 kΩ on later iterations of the circuit).

4.4 Signal Results

The function of the light detection and signal amplifying circuit was tested using the glass bead suspension, sewing thread and fishing line outlined in Section 3.5. Each test was preceded by a benchmark analysis of the decrease in voltage that resulted from fully blocking the light. The data from the test samples were compared to the benchmark test to determine the percent change in voltage that a glass bead and similar sized object would cause. This could later help distinguish beads/eggs from bubbles or other debris. The data of voltage changes from glass beads and other materials presented in this section helped drive the required sensitivity of the trigger-generating portion of the circuit.

4.4.1 Glass Bead Analysis

The initial test of the TIA was conducted using the glass bead suspension pushed through the microfluidic channel. The first test was conducted by suspending a stationary bead in the channel and using the micrometer mount on the microscope (see Fig. 3.1) to pass the bead in and out of the optical detection area. The TIA outputted a 6.4 mV drop in voltage when the bead was moved

through the detection area in the channel. This was 34% of the absolute decrease in voltage of 19.6 mV when the light was completely blocked using a business card. The recorded decrease in voltage is shown in Fig. 4.5 (a).

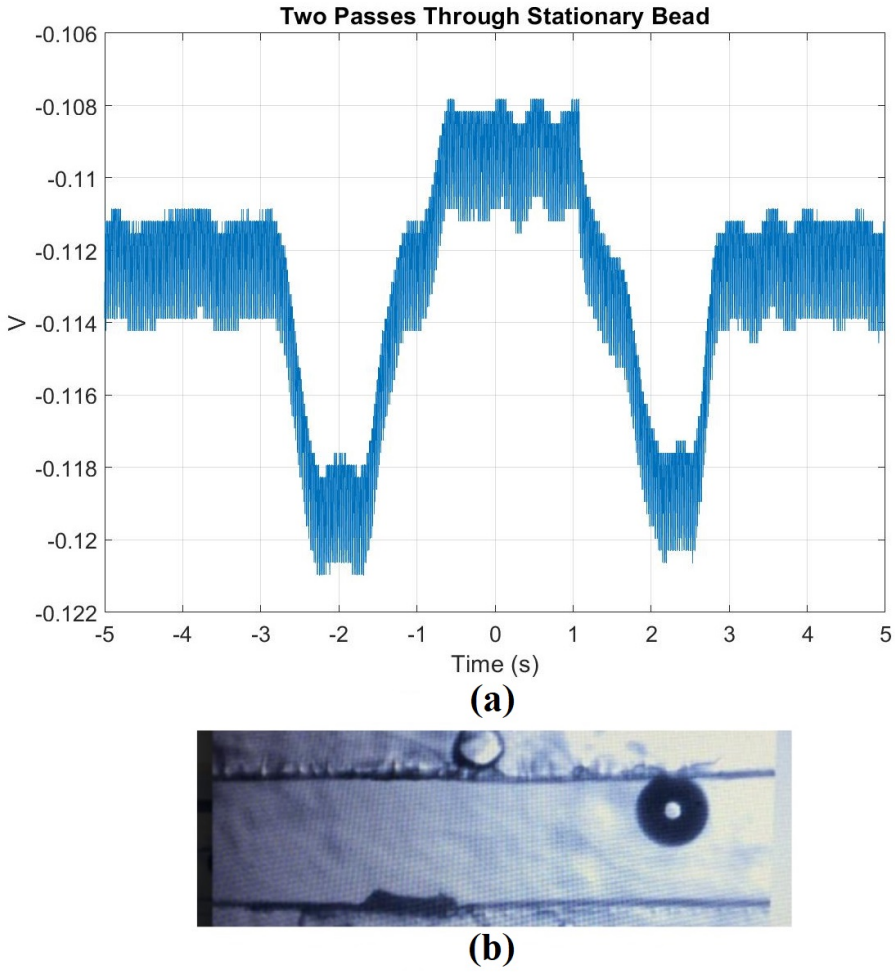

Figure 4.5: (a) Recorded drop in voltage of 6.8 mV at the TIA output of a stationary glass bead manually passed through the optical detection area and (b) camera image of an approximately 75 μm glass bead in the 150 μm wide microfluidic channel. The recorded drop of 6.8 mV from the glass bead was 34% of the total drop in voltage of 19.6 mV when the light was completely blocked.

With the confirmation that manually moving a stationary glass bead through the detection area caused the TIA to output a drop in voltage, the test was continued with glass beads flowing through the microfluidic channel. The flow rate of the syringe pump was set to 25 μL/min which caused the beads to pass through the optical detection area in approximately 0.40 seconds.

The velocity of the glass beads was calculated using the total optical detection area on the microfluidic channel and the duration of the intensity change recorded on the oscilloscope. The optical detection area of the 1 mm fiber optical cable was determined by its image formed by the objective lens onto the microfluidic channel. In the case of the $3\times$ objective lens, the detection area for the objective lens and 1 mm core diameter fiber was calculated by determining the de-magnified image of the fiber cable onto the channel by

$$h_i = \frac{h_o}{M} \tag{4.2}$$

where h_i is the height of the image, h_o is the height of the object and M is the objective magnification. Using 1 mm as h_o and $3\times$ as M, the optical detection area was calculated to be 0.33 mm. Based on this detection area, the velocity of the beads were calculated by

$$Velocity = \frac{\textit{distance}}{\textit{time}} \tag{4.3}$$

A single glass bead flowing through the optical detection area was recorded to cause a 3.7 mV drop in voltage which was 18% of the total decrease in voltage from completely blocking the light. Fig. 4.6 shows the recorded data of a single moving bead passing through the detection area in approximately 0.40 seconds.

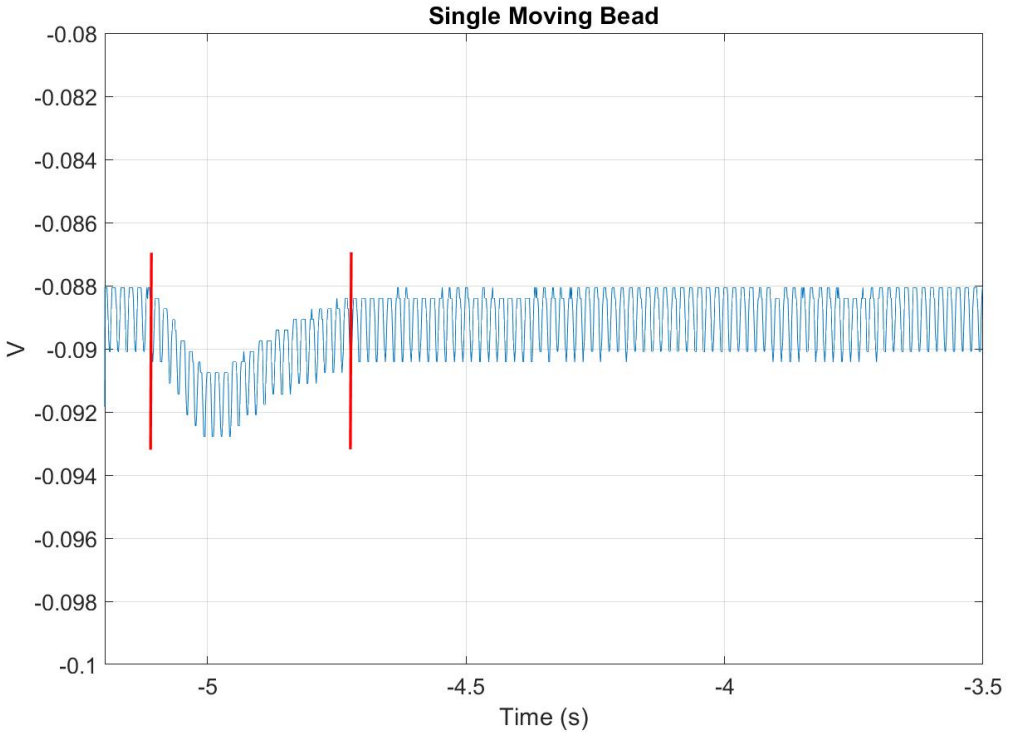

Figure 4.6: The recorded decrease in voltage of a single bead moving at 0.82 mm/second passing through the optical detection area on the microfluidic chip. This bead caused a 3.7 mV decrease in voltage which corresponded to an 18% decrease in the total signal when the beam was completely blocked. Red lines show approximate location on signal to show time duration of approximately 0.40 seconds of bead through detection area to calculate for approximate velocity.

Given the optical detection area of 0.33 mm, a 75 μm size bead should take up approximately 5.1% of that area. It is unclear why the bead that takes up approximately 5% of the detection area blocks 18% (when moving) to 35% (when stationary) of the light. This discrepancy could be due to different objective lens magnification used for this test than what was recorded at original set-up. As multiple students were using this microscope, it is possible that the objective lens was changed and left unrecorded.

Decrease in voltage from two consecutive beads passing through the channel was recorded next. These beads accompanied a clump of other beads and were the easiest to correlate the decrease in voltage to the time the live camera showed them passing through the detection area. Bead 1 caused a 1.7 mV decrease in voltage, and bead 2 caused a 2.3 mV decrease in voltage.

For the beads 1 and 2, it was difficult to accurately determine a speed for each bead. These beads blocked 8.4% and 11.8% of the light respectively. Using optical detection area of 0.33 mm, the beads were approximated to have diameters around 30 μm which is not consistent with the known bead diameter range of 63-75 μm. The faster moving beads in a clump of other beads could have moved too quickly for the circuit to respond to the full change in voltage or the optical detection area could have misaligned with the channel causing some signal in the channel to be lost. As the beads were moving close together it was difficult to determine using just the live video feed where each bead signal exactly started and ended. The decrease in voltage from the two moving beads is shown in Fig. 4.7.

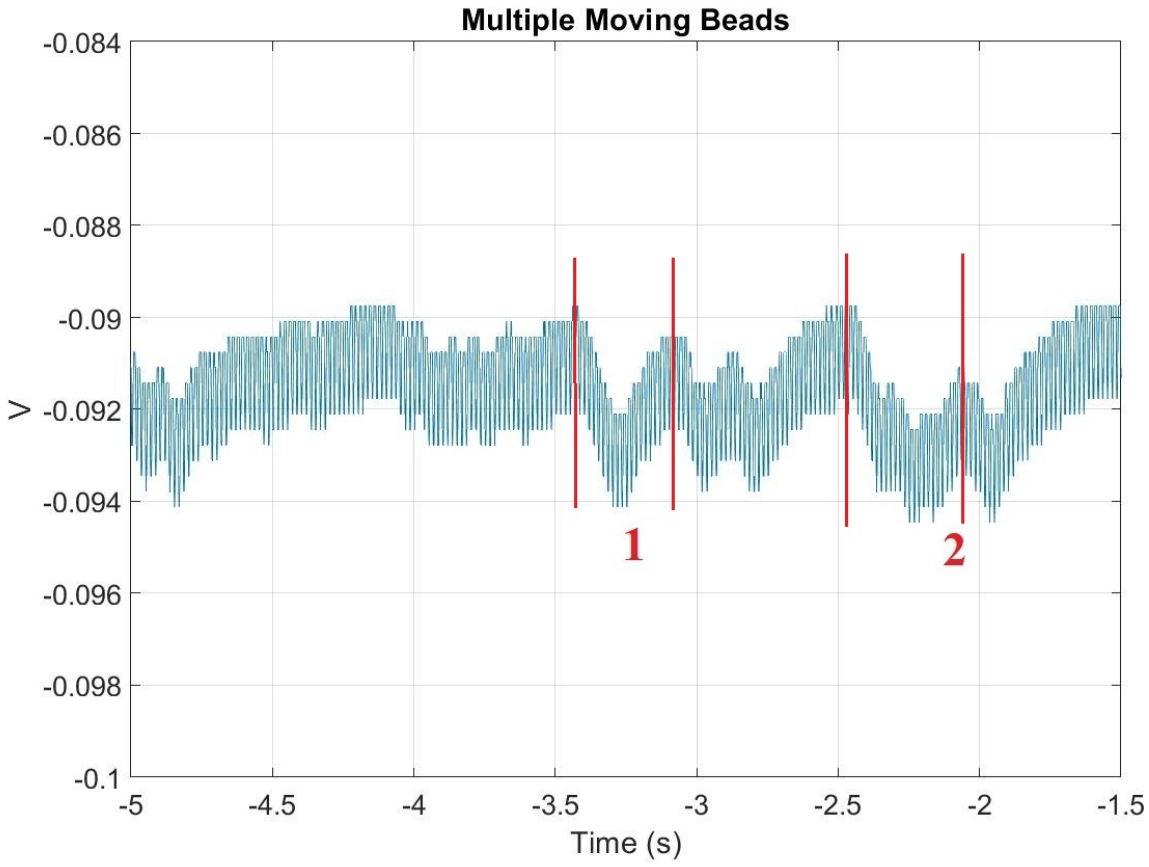

Figure 4.7: The decrease in voltage of two consecutive beads passing through the channel. Bead 1 caused a decrease in voltage of 1.7 mV which was 8.4% of total decrease in voltage and bead 2 caused a decrease in voltage of 2.3 mV which was 11.8% of total decrease in voltage. Red lines show approximate location on signal to approximated full pass of each bead. This was determined by correlating oscilloscope reading to live camera feed.

The velocity of the three moving beads were compared to the approximate fluid velocity in the channel. The approximate fluid velocity of the fluid in the channel pumped at 25 μL/min was calculated to be 18 mm/second by

$$Q = Av \tag{4.4}$$

where Q is the flow rate, A is the area and v is the velocity. The area of a section of the channel was approximated by the square of the width of the channel (150 μm). The velocity of the moving beads was much slower than the estimated fluid velocity which could have been a result of the beads sticking to the side of the channel or the flow of the fluid being impeded by clumps of beads or other objects in the channel.

Confirmation of the TIA's sensitivity to glass beads flowing through the channel served as a basic design to build on for a higher sensitivity circuit. High frequency oscillations were still measurable, but did not impede the data collection of the glass beads or compromise the accuracy of results. After the initial photodiode used for these test was replaced with a new one of the same make and model, all measurable high frequency oscillations were eliminated and no further suppression methods were needed for the remainder of the project. This provided evidence that the oscillations were possibly due in part to the dying original photodide component.

4.4.2 PCB Analysis

The opaque nature of the PCB made it hard to verify what voltage changes resulted from particles of interest. The functionality of the integrated optics onto the PCB was tested using a dried paint spot on fishing line that was pulled through the optical detection area using the ends of the line.

The first test of the optics was conducted using a green laser light coupled into the illumination fiber being blocked by a card. This served as the benchmark of an absolute change in voltage and was recorded from the output of the inverting amplifier. The resulting voltage change from the laser light blocked three times was recorded to be 2.03 V and is shown in Fig. 4.8.

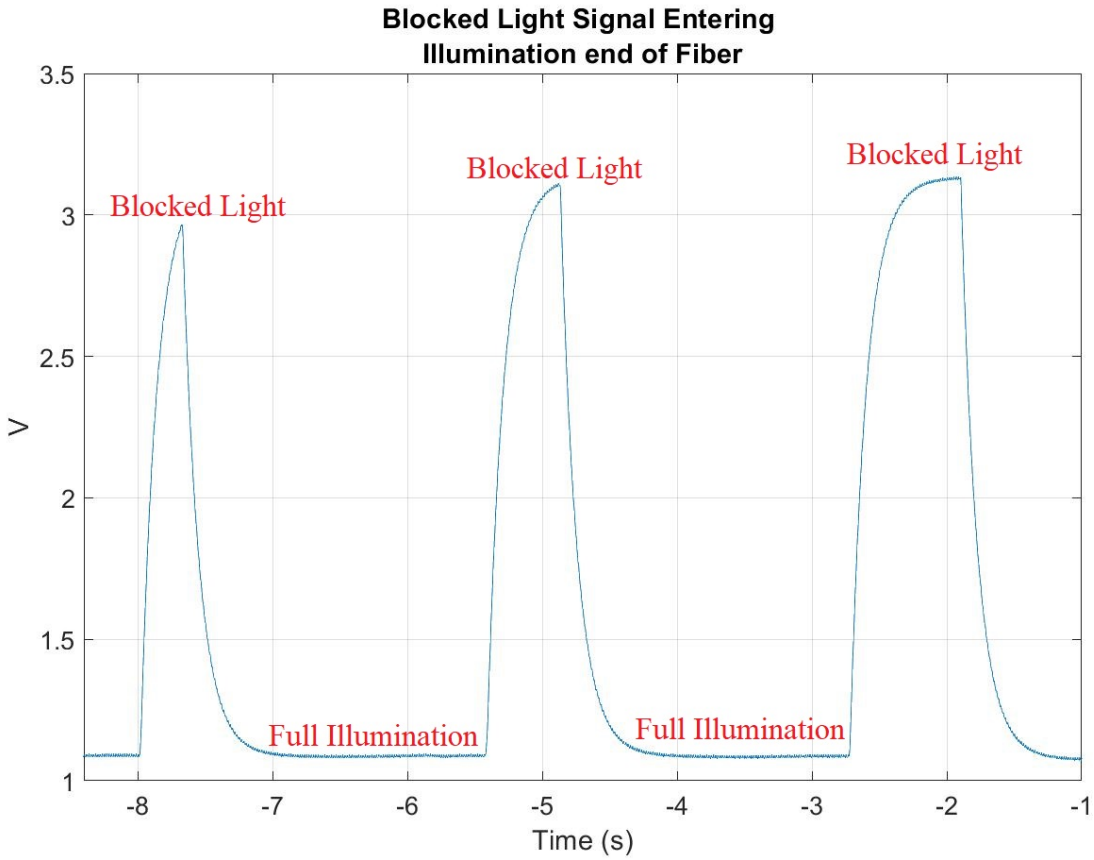

Figure 4.8: The output of the inverting amplifier when the green laser light coupled into the POF attached to the board was blocked using a card. A change in voltage of 2.03 V was recorded and served as a benchmark value for additional tests. This signal was recorded at the output of the inverting amplifier.

With the confirmation that the installed POFs were able to accommodate the photodiode detecting an absolute change in light, a second test using an object in the channel was conducted. A paint spot dried onto fishing line was passed in and out of the optical detection area by pulling on the ends of the fishing line. The paint spot spanned the full width of the channel so it blocked most of the light (depending upon its orientation in the channel) entering the photodiode. A change in voltage of 0.43 V was recorded when the spot was pulled quickly through the detection area and a change of 0.93 V when it was pulled through slower. The magnitude of the change in voltage of the dried paint spot was much larger than that of glass beads or sewing thread. This was expected as the dried paint spot was larger than the optical detection area on the PCB whereas the glass beads

and thread were not. The change in voltage from the dried paint spot pulled through the detection area twice is shown in Fig. 4.9.

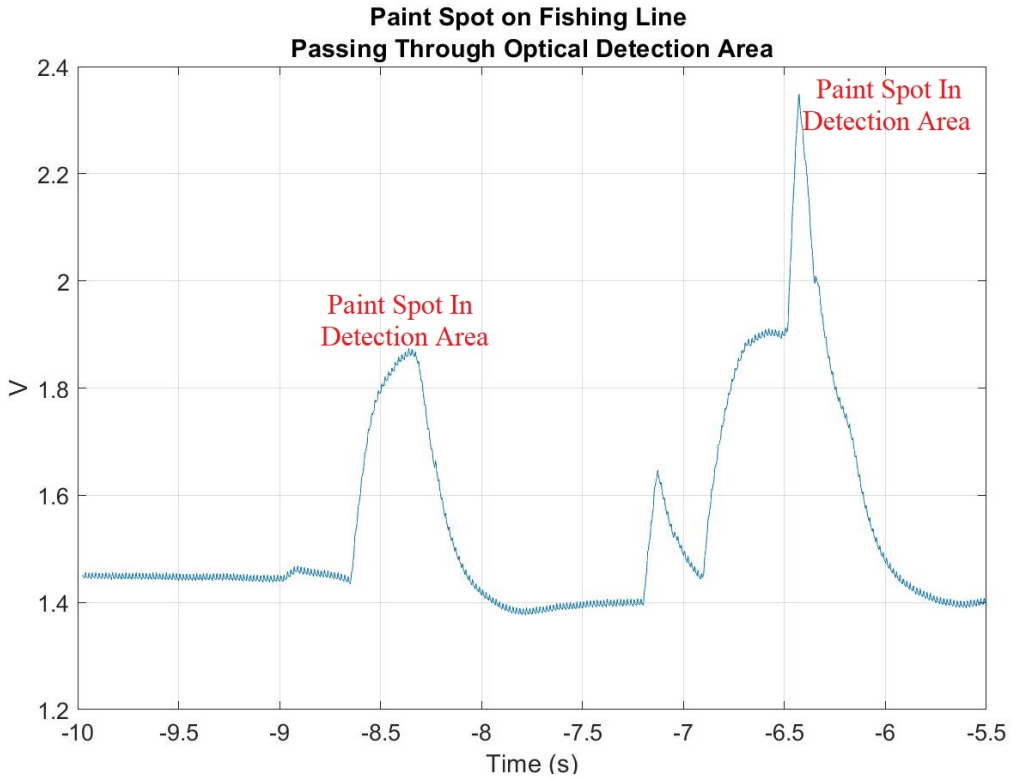

Figure 4.9: The two largest peaks in this plot are a result of a voltage change from a paint spot dried onto fishing line passing through the optical detection area on the PCB device. The first pass yielded a 0.43 V change in voltage and the second pass yielded a 0.93 V change in voltage. The base voltage when no object was in the detection area varies to the base voltage shown in Fig. 4.8 because of the clear fishing line that was used to pull the paint spot through the channel and thus continuously obstructed the light entering the photodiode. This signal was recorded at the output of the inverting amplifier.

The baseline voltage between Fig. 4.8 and 4.9 are different by approximately 0.4 V due to the slight obstruction of light caused by the clear fishing line. The line had to be placed along the entire channel to be able to externally pull the dried paint spot through the detection area. The clear material of the fishing line blocked 19% of the total light entering the photodiode. The smaller change in signal in Fig. 4.9 was a result of moving the paint spot through the detection area approximately twice as fast as the second, larger change in voltage. This is an approximation based on how quickly the fishing line was manually pulled through the channel.

4.5 Discussion

The result of a moving glass bead in the microfluidic channel causing a useable output for a trigger circuit gave confidence that other objects of similar size, like strongyle eggs, would be able to trigger the circuit also. The main limit for a useable output from the TIA was due to the high frequency oscillations that overpowered small changes in light intensity. It was found that too large of values for feedback capacitance on the TIA would not only suppress the oscillations but also suppressed changes of 1-5 mV. Deductive testing of different capacitance values was the quickest and most effective way to determine the necessary feedback capacitance that suppressed oscillations without suppressing the measured signals. The use of a brand new photodiode was found to completely eliminate any measurable oscillations on the output of the TIA which was an example of the importance of the quality and age of components needed for nano-amp light detection. A grounded sheet of foil placed over the circuit was used as a modified Faraday cage used to block external oscillations coming from the electrical wiring of the lab and any other possible external interferences. While the circuit was not noise and oscillation free, the methods outlined above were sufficient to reduce the external effects that compromised the output of the circuit.

The signal changes from moving glass beads through the microfluidic channel blocked approximately 8% to 20% of the total light. These values are important for further designs of the circuit to determine the range at which glass beads/eggs block the light to distinguish them from bubbles and other debris.

This detection circuit tested for light responses on the PCB proved that lens optics were not required to obtain an output signal. The PCB required a modified test as the contents of the channel could not be verified visually and a particle with a diameter 7.5$\times$ larger than a strongyle-sized egg was used to test the efficacy of the integrated optics. Objects that are 70 - 80 μm in diameter are difficult to obtain and difficult to manually manipulate for the preliminary tests conducted for the integrated optics.

4.6 Conclusion

The light detection and signal modification stage of the optical detection circuit consisted of a TIA and inverting amplifier. The TIA was designed to amplify a current signal of 1 nA to approximately 10 mV. A large valued feedback resistor, Rf, in parallel with two feedback capacitors amplified the signal and suppressed some of the high frequency oscillations so changes of 1-2 mV could be distinguished on the oscilloscope. The TIA successfully output distinguishable signals caused by a change in light from stationary glass beads and flowing glass beads in the microfluidic channel. To further increase the magnitude of the voltage signal, an inverting amplifier was placed at the output of the TIA. The amplification and polarity change on the signal allowed for the signal to be used at the input of the comparator circuit that would ultimately serve as the trigger portion of the apparatus.

Testing the accuracy of the optic's detection abilities on the PCB device was more difficult than testing with the glass device. The opaque material of the PCB did not allow for visual inspection of the contents of the channel after the device had been completely constructed. An alternative method for testing was done using a 200 μm paint spot dried onto fishing line that was externally pulled through the optical detection area. This served as an initial test that the integrated optics onto the PCB device could detect objects moving through the channel.

Chapter 5

Comparator Circuit

5.1 Introduction

The function of the comparator was tested using three different configurations for the reference voltage. When a change in signal was detected (i.e. a particle of interest passed through the optical beam in the channel) the comparator output went from a "LOW" voltage of -8 V to a "HIGH" voltage of 8 V. This output was a signal that could be used to trigger any data collection device. To test the baseline operation of the op-amp comparator circuit, a potentiometer was set to the recorded voltage of the unobstructed light that ranged from -200 mV to -90 mV on the initial microscope set-up. The circuit schematic including the potentiometer is shown in Fig. 5.1.

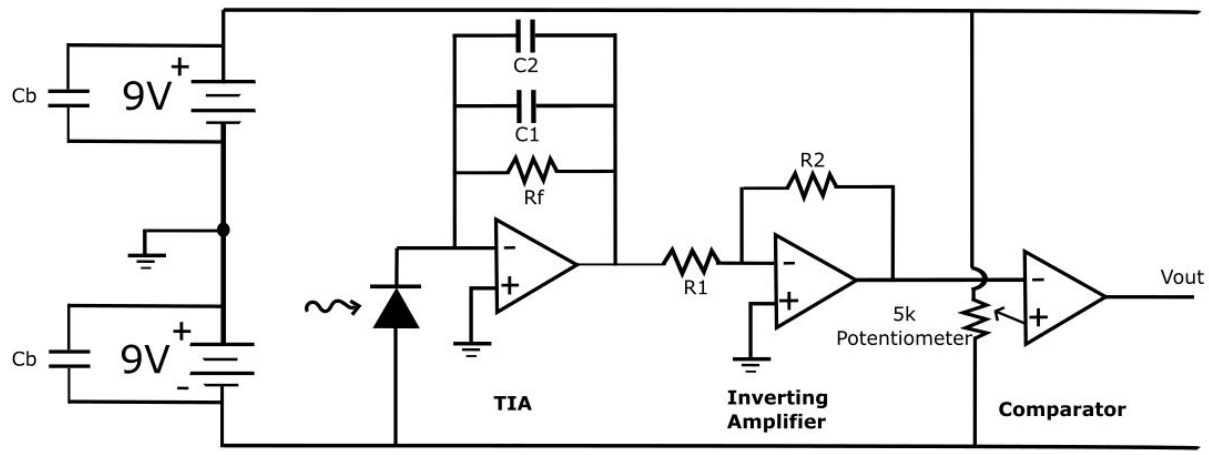

Figure 5.1: Circuit schematic of trigger circuit using a 5k Potentiometer as the reference voltage for the op-amp comparator.

This voltage level of the illuminated light varied by 5-10 mV each test due to changes in light from the lamp/LED and the lab lighting. A business card was used to block the light completely from entering the photodiode causing a 20 mV change in signal, and the comparator successfully output "HIGH". The initial test data of the output of the comparator is shown in Fig. 5.2.

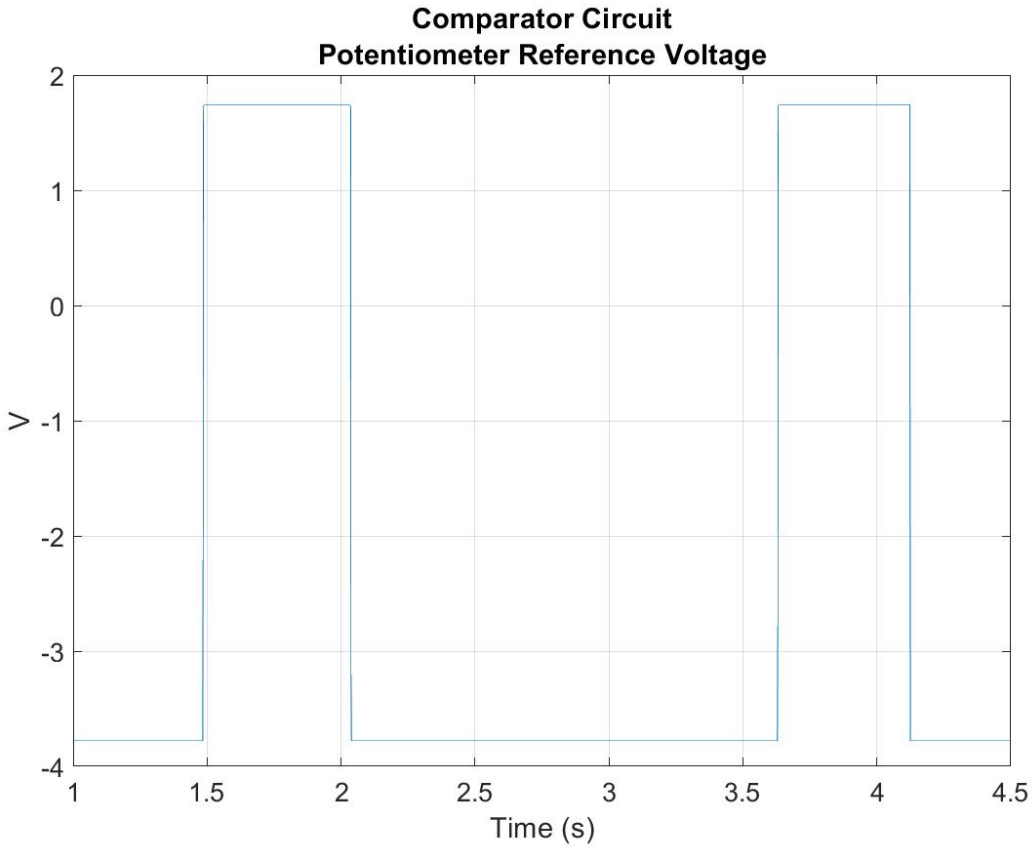

Figure 5.2: Output of op-amp comparator for initial circuit test using a potentiometer as the reference voltage. The two peaks correspond to the light being completely blocked using a business card. The comparator output swung approximately 6 V.

Simulations of the circuit were beneficial in predicting circuit behavior and diagnosing circuit problems. This trigger circuit was simulated in LTSpice XVII which included simulations for stages of the circuit and the entire circuit. The output of the TIA was recorded for a knot tied in a piece of sewing thread (approximately 0.33 mm in diameter) passing through the optical detection area of the glass microfluidic device. This data was saved in a comma separated value (.csv) format through a USB oscilloscope (*Analog Discovery 2* from Digilent). This recorded data was inputted into the simulation for testing. The .csv file of the data was loaded into the voltage source as a piecewise linear function in the LTSpice XVII simulation interface.

The potentiometer method of setting the reference voltage required the voltage level to be set each time a test was run because the baseline voltage due to the unblocked light varied run-to-run

due microscope stage position and illumination source. The sensitivity of the turn-nob to set a voltage on the potentiometer could cause changes of around 50 mV in output signal with a quarter of a turn. Having to manually set the reference voltage for each test was not a conducive way to create a trigger circuit so different filters were designed to mimic the unchanging light signal from the channel.

5.2 Low Pass Filter

To create a more robust method of setting a reference voltage for the comparator, a LPF was implemented following the inverting amplifier as shown in Fig 5.3.

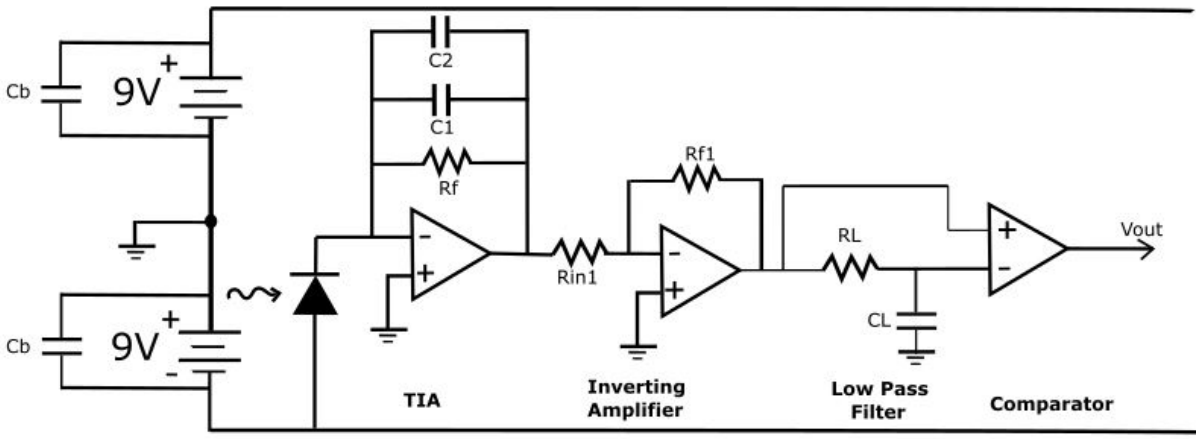

Figure 5.3: Schematic of the detection and trigger circuit with a LPF used to generate the reference voltage for the comparator. All component values are the same as previously stated including additional components RL = 10 MΩ and CL = 10 μF.

To mimic the signal of the unchanging light of the system, the RC time constant, τ, for the LPF was designed to be much longer than the anticipated time of 1 to 10 seconds between bead/egg events in the channel. A time constant longer than the anticipated time between events caused the discharge of the LPF to negligibly react to the change in LPF input voltage and thus appear to remain constant. A resistance value of 10 MΩ was followed by a capacitor of 10 μF yielding a

total RC time constant of 100 seconds (τ = RC). The output of the LPF compared to the signal is shown in Fig. 5.4.

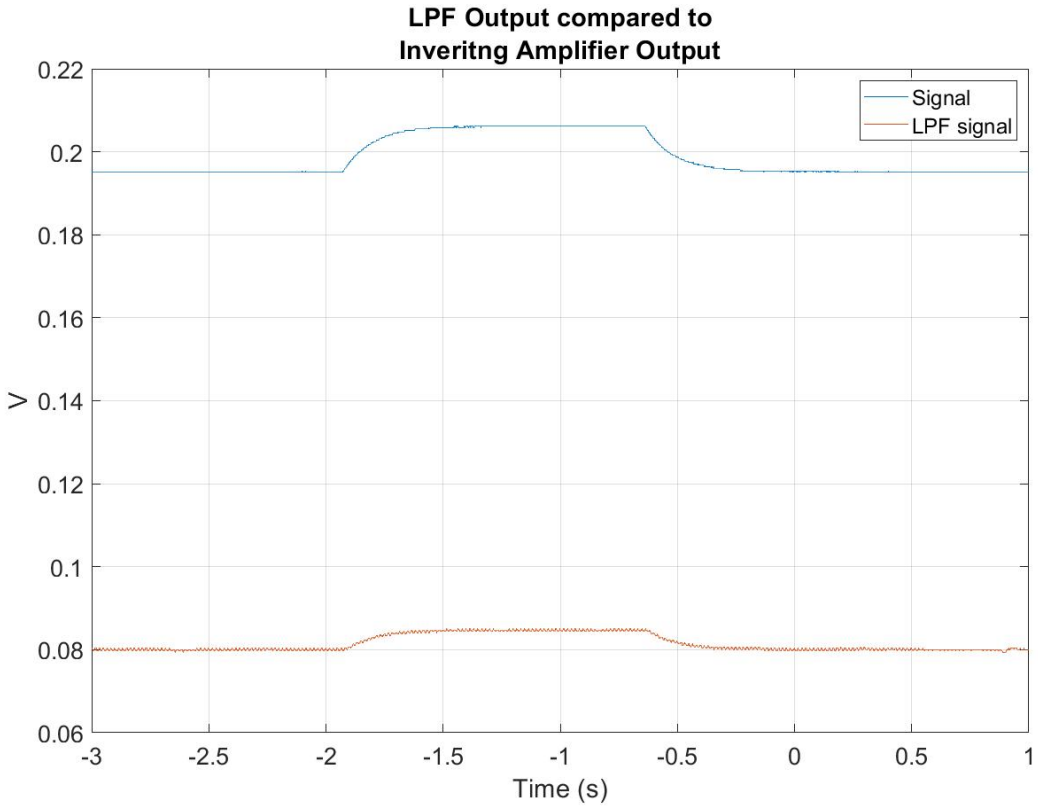

Figure 5.4: The offset between the output of the LPF and the output of the amplifier. There is approximately 0.12 V gap between the two signals the would not allow the comparator to trigger for changes in voltage.

An offset of 0.12 V between the LPF output and inverting amplifier was present on the signal. This offset could cause the comparator to not trigger from a change in voltage due to an object blocking light in the channel. Two tests were done with an additional amplifier and then a buffer wired onto the circuit to remove the offset between the signals. These tests are discussed in the following section.

5.2.1 Additional Amplifier

To remedy the offset present between the LPF and inverting amplifier outputs, an inverting amplifier identical to the first amplifier was placed between the first inverting amplifier and the positive pin on the op-amp comparator shown in Fig. 5.5.

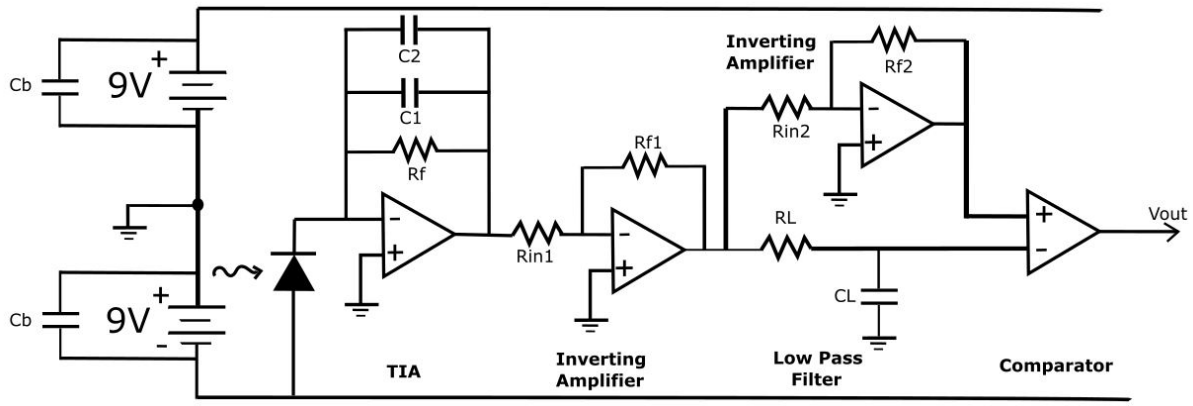

Figure 5.5: Schematic of the detection and trigger circuit with an identical inverting amplifier placed between the output of the first amplifier and positive input pin of the op-amp comparator. All component values are the same as previously stated with additional components Rin2 = Rin1 and Rf2 = Rf1.

This design did not eliminate the DC offset on the signal, but the additional gain applied to the signal compensated for that offset and allowed the comparator to detect a difference in voltage between the two inputs. Fig 5.6 compares the output of the second amplifier to the output of the LPF. While this method worked, it was not a reliable solution as the offset increased with the additional amplification on the signal. The total output signal of the second inverting amplifier was approximately 12 V when the light was fully blocked. In Section 4.4.1, it was found that glass beads blocked 8% to 20% of the total light. With this additional amplification stage, the expected change in voltage resulting from the beads would be around 1 V to 2.5 V which would not be enough to bridge the offset 4 V offset.

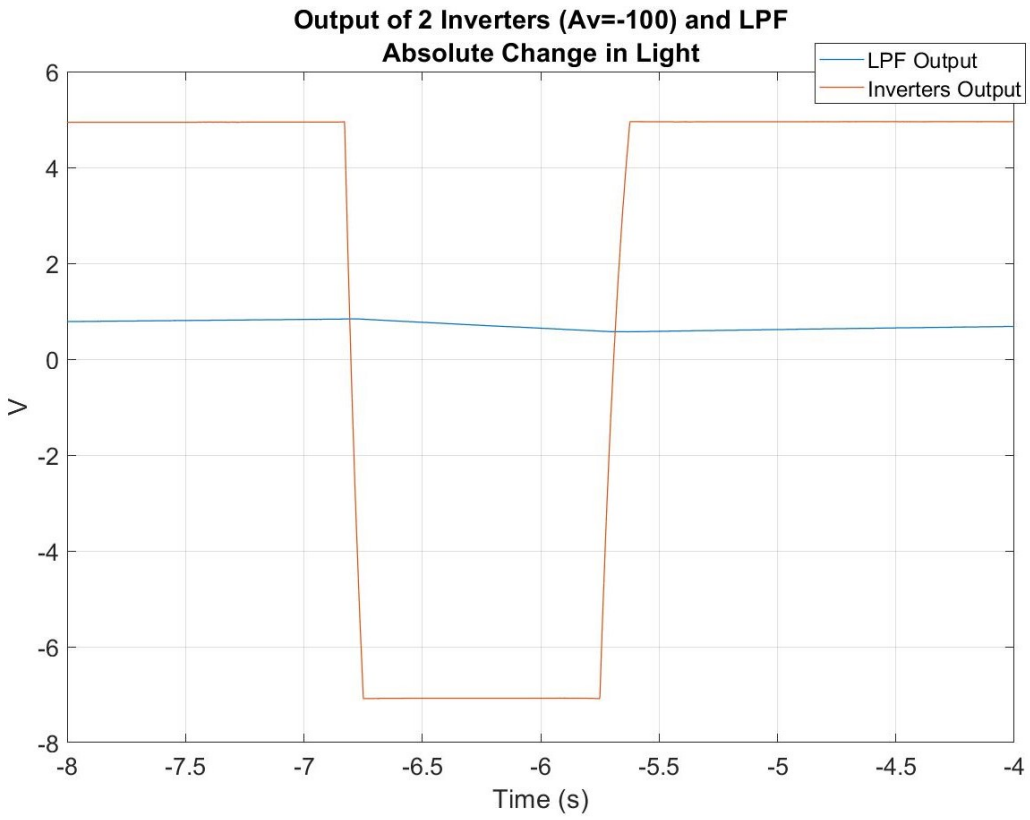

Figure 5.6: Output of the two inverting amplifiers compared to the output of the LPF. The DC offset of the signal was still present, but the amplification compensated for the gap allowing the comparator to read the change in voltage.

The offset between the signals could have been a result of loading on the circuit. Circuit loading happens when a source has a higher impedance than the load, and when connected, the load draws more current causing a drop in voltage. An additional cause of the offset could be due to the *Analog Discovery 2* oscilloscope added in series with the 10 MΩ resistor of the LPF. The signal dropped as it passed across the 10 MΩ resistor of the LPF which was then read by the oscilloscope possibly leading to the offset between the outputs. A buffer between stages is sometimes used to eliminate circuit loading as it raises the impedance of the load and in turn draws less current. A circuit was simulated to determine if a buffer could eliminate the DC offset. The design of the circuit in the simulation mimicked the physical circuit on the breadboard and included an inverting amplifier with gain -10, inverting buffer, a LPF with a τ = 100 seconds and an op-amp comparator. The results of the simulation are shown in Fig. 5.7 and the circuit is shown in Fig. 5.8.

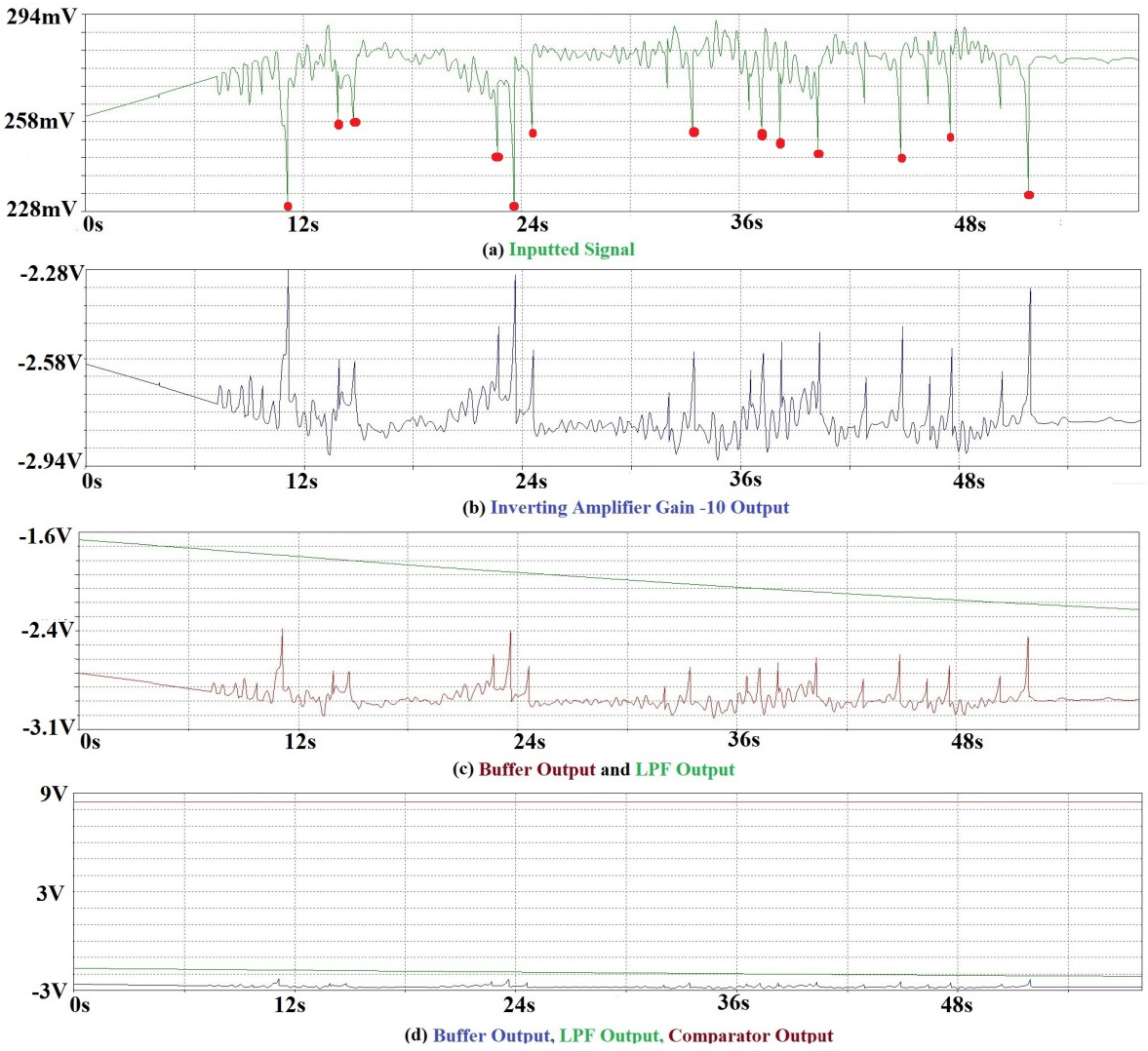

Figure 5.7: (a) The inputted data of a knot in sewing thread recorded from the output of the TIA (signals from the knot passing through the detection area are marked with a red dot totaling 13 events), (b) output of the inverting amplifier with a gain of -10, (c) output of the buffer alongside LPF output (note offset between outputs) and (d) output of comparator alongside LPF and buffer outputs showing no output from a change in voltage. (a-c) Enlarged images of the signals presented alongside comparator output in (d). It is important to note the decreasing green trace of the LPF in (c). This is a result of the long time constant of the filter causing the capacitor to take a long amount of time to charge. In the simulation program there is a setting to compensate for this time, but the computer this simulation had to be conducted on due to COVID-19 could not handle this long of a simulation.

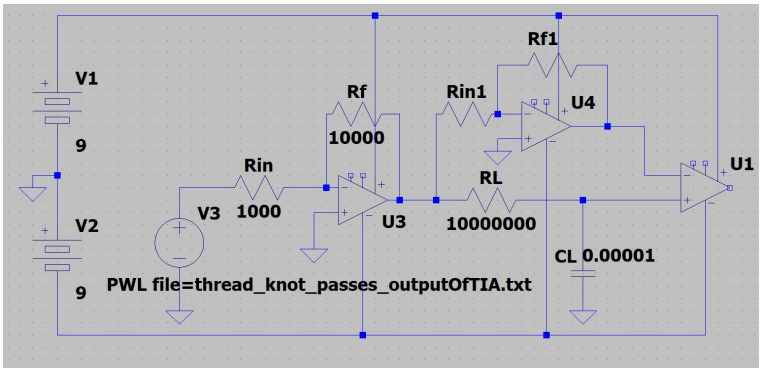

Figure 5.8: Circuit simulated for the results presented in Fig. 5.7.

While this simulation with the inverting buffer was shown to reduce the gap between the output of the inverter and LPF, it was not enough to cause the comparator to trigger at a change in voltage. The use of the LPF removed the need to manually set a voltage on the potentiometer for each test run but still yielded the undesired DC offset on the signal. A third method using a high pass filter was tested to eliminate the DC offset.

5.3 High Pass Filter

The third method used for the reference voltage on the comparator was the implementation of a high pass filter (HPF). The HPF followed the original inverting amplifier and removed the DC offset of the signal. This allowed the signal to be compared to ground by the op-amp comparator and eliminated the need of additional stages in the circuit to modify the voltage to effectively trigger the comparator. The reduced number of components on the board reduced the possibility for feedback within the board, drifting of the original signal, cost and makes the circuit easier to troubleshoot.

A simple configuration using a blocking capacitor between the output of the inverting amplifier and input of the comparator was simulated in LTSpice XVII to see if it could be an appropriate substitution for the LPF and inverting buffer design. The motivation behind the HPF design was to block the DC offset that was present in the signal so the AC portion of the signal could be compared to ground on the comparator. The simulation was performed using the inverting amplifier with

gain -10 and a blocking capacitor whose output was inputted into the negative pin of the op-amp comparator with results shown in Fig. 5.9. This circuit is shown in Fig. 5.10.

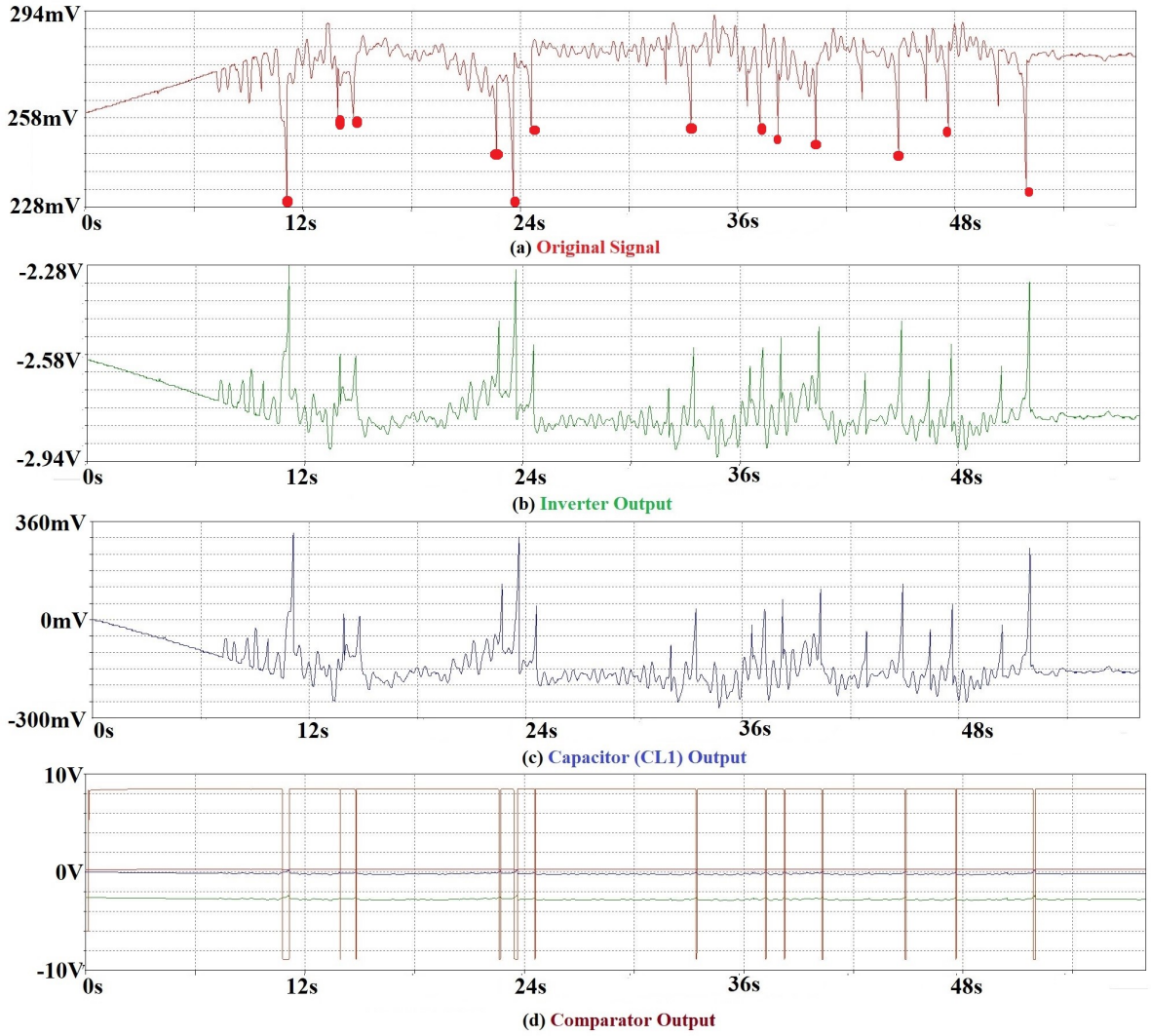

Figure 5.9: (a) The inputted data of a knot in sewing thread recorded from the output of the TIA (signals from the knot passing through the detection area are marked with a red dot totaling 13 events), (b) the output of the inverting amplifier, (c) the output of the blocking capacitor (notice the DC offset has been eliminated) and (d) output of the comparator triggering "LOW" when the knot passed through the detection area. (a-c) Enlarged images of the signals presented alongside comparator output in (d).

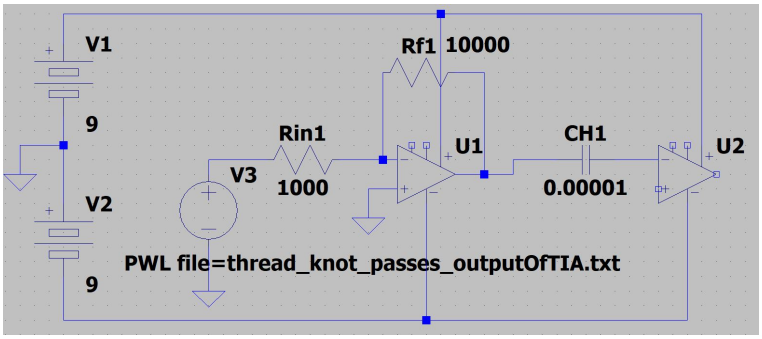

Figure 5.10: Circuit simulated for the results presented in Fig. 5.9.

The DC offset of the signal was successfully eliminated which is shown in Fig. 5.9 (c). In experimentation this design caused a malfunction in the comparator circuit. The single capacitor at the output of the inverter would continuously charge until it caused the comparator op-amp to stop functioning where there was no change in output when the light beam was blocked. A HPF replaced the blocking capacitor and a resistor was added between ground and the non-inverting pin of the op-amp. This resistor had an identical resistance as the resistor in the HPF to balance the impedance at each input. This reduced the offset between the two input pins of the op-amp which could minimize the offset in the comparator output. The LM358 op-amp was equipped with bi-polar junction transistors which allowed current leakage at each input pin. The following design of the HPF tested different values of resistors for the HPF and between ground and non-inverting input pin of the op-amp.

Different values of resistors were simulated to determine which configuration would cause the comparator output to change only when the thread passed through the beam. Resistor values of 1 kΩ, 680 kΩ, 1 MΩ and 10 MΩ were simulated. The simulation showed that resistors less than 10 MΩ caused noise and oscillations to trigger the comparator. The configuration with 10 MΩ resistors allowed only 4 additional signals from oscillations and noise to trigger the comparator. Simulations for the various resistor values are shown in Fig. 5.11.

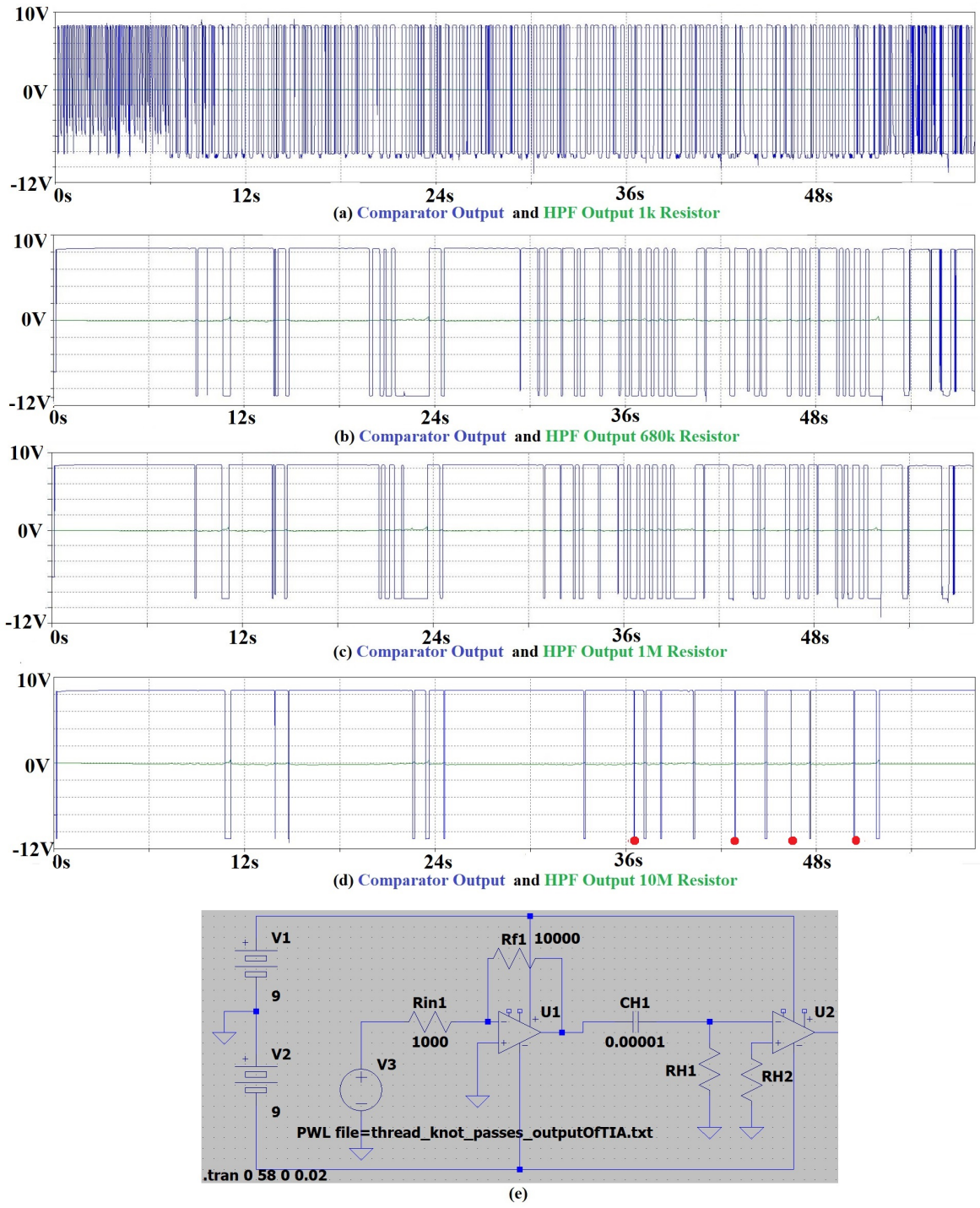

Figure 5.11: Simulations for resistor values (a) 1 kΩ, (b) 680 kΩ, (c) 1 MΩ and (d) 10 MΩ. Each configuration caused the comparator to trigger for events that were not caused by the thread passing through the beam. This configuration allowed 4 additional signals, other than the thread, to trigger the comparator (marked by red dots). (e) Circuit being simulated.

A schematic of the detection and trigger circuit implementing a HPF is shown in Fig. 5.12.

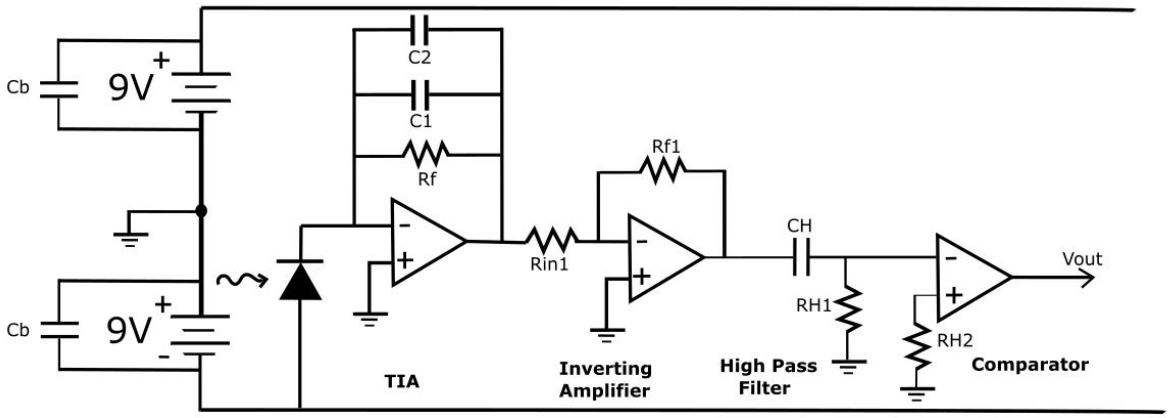

Figure 5.12: Schematic of circuit implementing a HPF after the inverting amplifier. All component values are the same as previously stated with an additional components CH = 10 μF and RH1 = RH2 = 680 kΩ .

In experimentation, RH1 and RH2 resistor values of 10 MΩ caused the comparator to trigger only when the light was completely blocked. Fig. 5.13 shows the output of the HPF where the smaller peaks of 150 mV from sewing thread did not trigger the comparator but a signal of approximately 3 V from blocking all light entering the photodiode did trigger a comparator output.

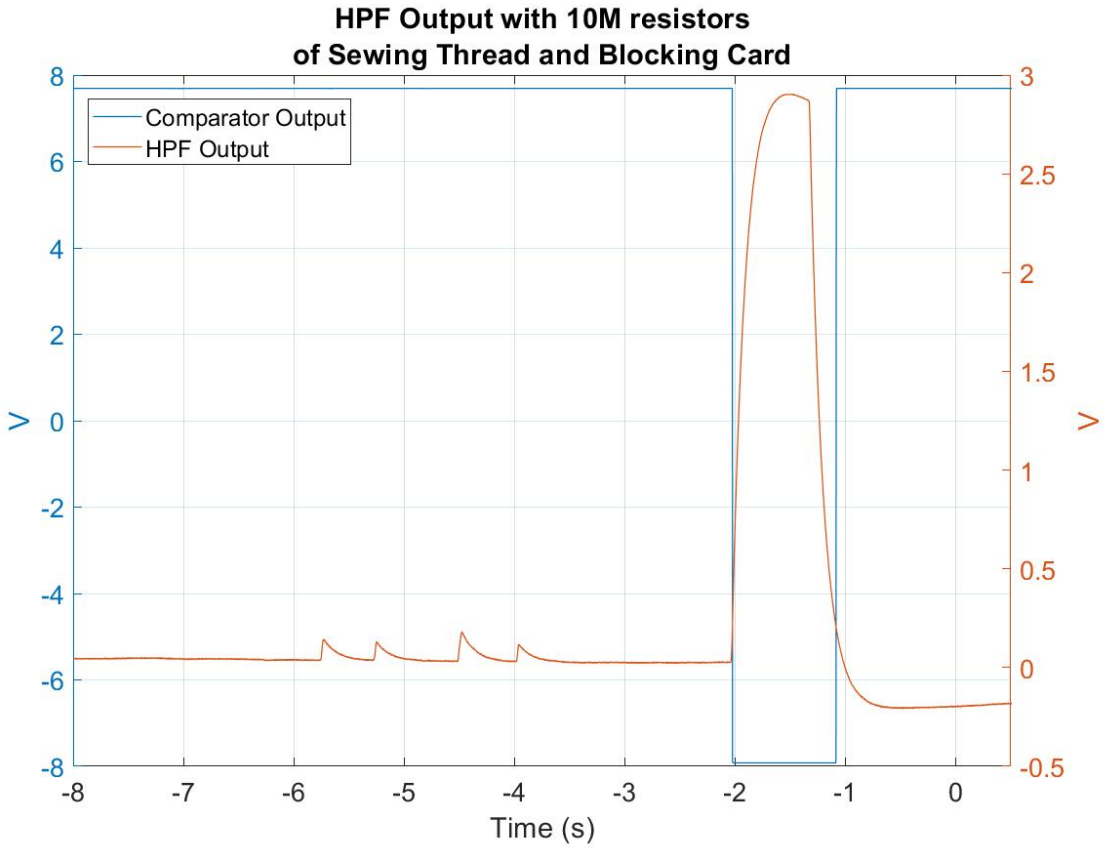

Figure 5.13: Output of the HPF with 10 MΩ resistors connected to ground at the inputs of the comparator. The signals from the sewing thread of 150 mV did not trigger the comparator circuit but the signal of 3 V from completely blocking the light beam did trigger the comparator circuit.

Resistor values below 580 kΩ lowered the DC offset to where noise signals, oscillations and intensity changes caused by the sewing thread triggered the comparator. This was contrary to the simulation results where a resistor value of 10 MΩ still allowed for noise signals to trigger the comparator circuit. Resistors with a value of 680 kΩ were used for RH1 and RH2 (see Fig. 5.12) as they limited the fluctuations at the comparator output and only allowed the signals of interests triggered the comparator. Fig. 5.14 shows the difference in comparator outputs using 560 kΩ resistors and 680 kΩ resistors.

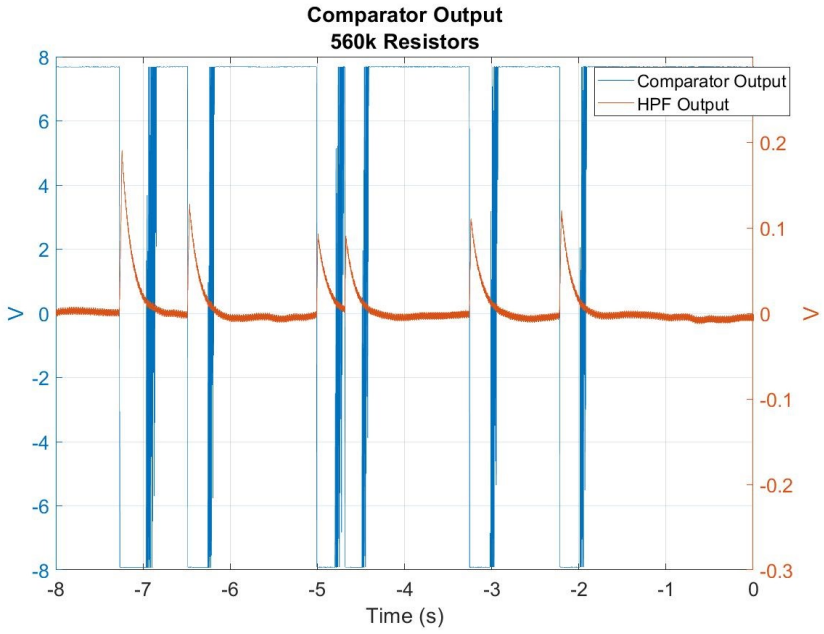

(a)

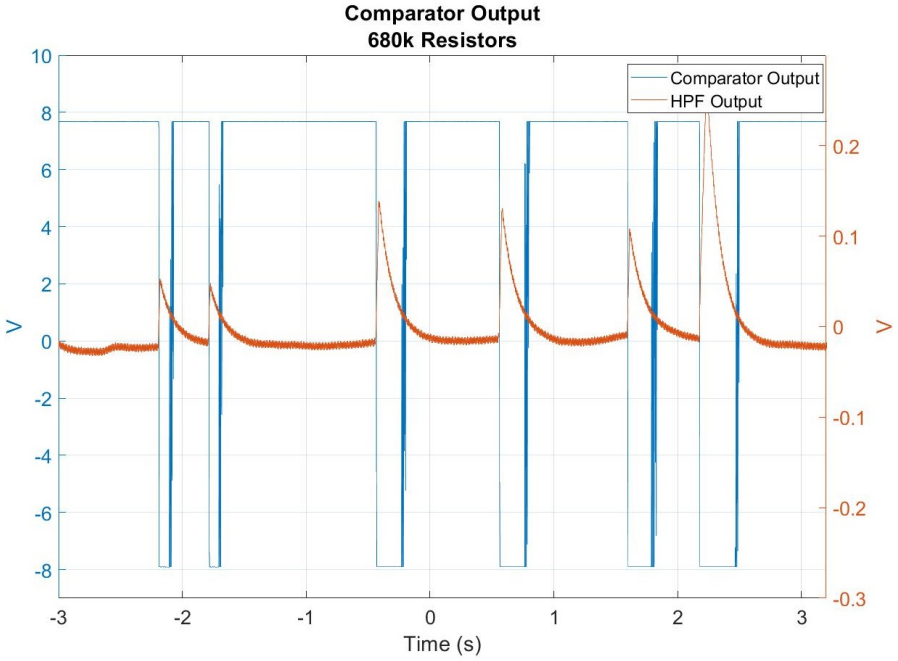

(b)

Figure 5.14: Output of the comparator using (a) 560 kΩ resistors and (b) 680 kΩ resistors at the inputs. The change in voltage resulting from the thread ranged from 60 mV to 280 mV after passing through an amplifier with gain -15. The large difference in voltage changes were due to a range of speeds that the thread was passed through the detection area at.

The fluctuations at the output of the comparator were thought to be due to the the small high frequency oscillations on the falling edge of the signal that continued to trigger the comparator as it fluctuated around the reference voltage. Fig. 5.15 (b) shows a zoomed in view of these fluctuations on the falling edge of the signal.

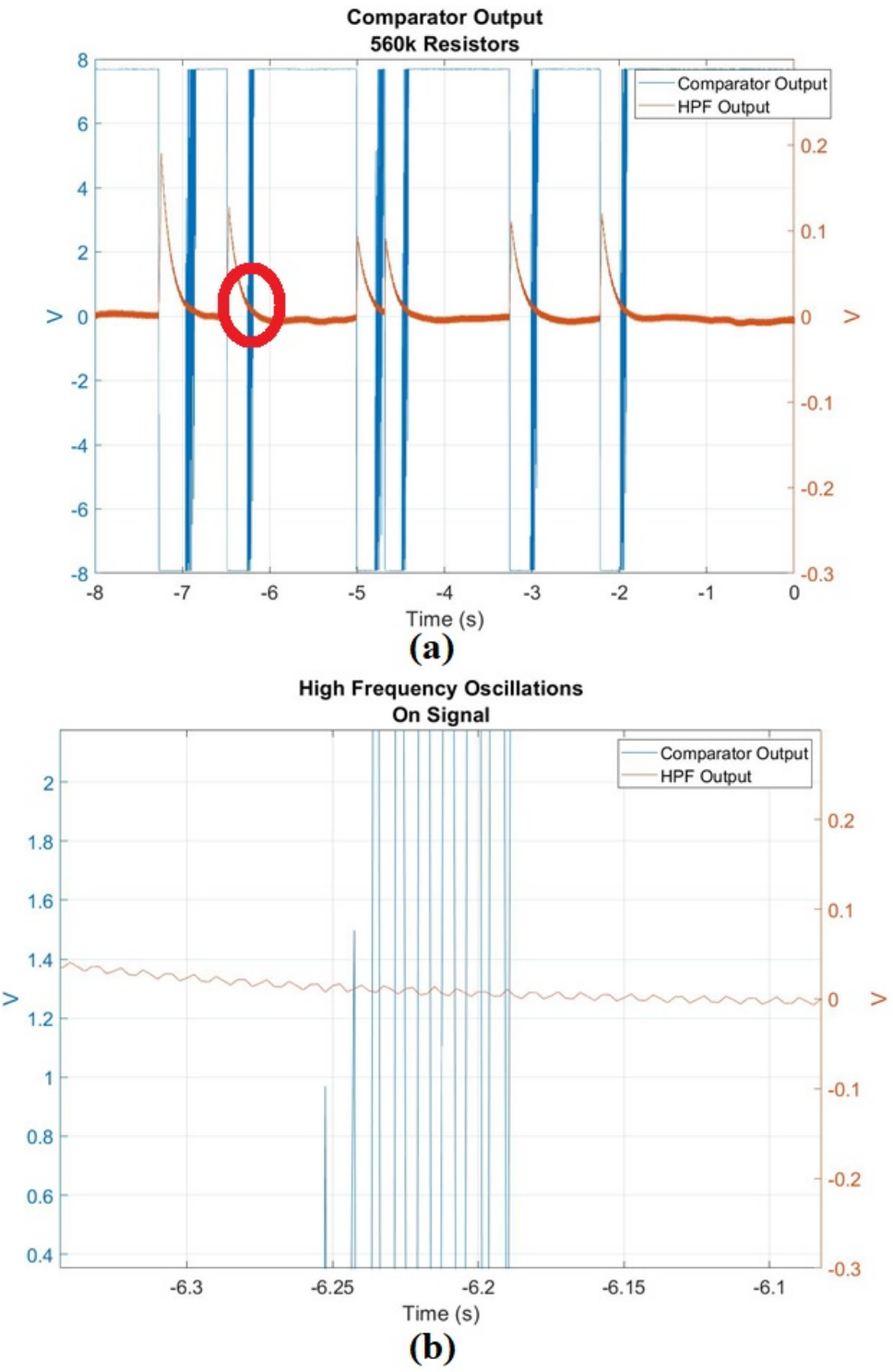

Figure 5.15: (a) The high frequency fluctuations on comparator output using 560 kΩ resistors. Red circle is the area of enlargement of the signal that is presented in (b).

The fluctuations on the output of the comparator could have been caused by an offset between the input bias currents of the op-amp. Ideally, these inputs would be the same, but in reality there is some leakage of current at each input. The input bias current for the LM358 is +/- 10 nA (min) and +/- 35 nA (max) [22] so there are a wide range of offsets that could be present on different components of the same model. In a worst case scenario of a leakage current of 35 nA and added resistance of 680 kΩ at the input, the DC voltage at that point would be around 24 mV. Adding resistors can influence the value of this DC offset which would in turn influence the level of the voltage on the output. The DC voltage with 560 kΩ resistors drops to 19.6 mV. Lowering that DC offset allows more high frequency oscillations to fluctuate around the reference voltage causing more fluctuations at the comparator output. Fig. 5.16 shows an enlarged image of the falling edge of the output signal of the HPF with illustrated levels of small theoretical changes in DC voltage level.

While in a steady operating state the signal could be easily compared to the reference voltage (ground), but the baseline of the signal was still altered depending on the height of the microscope stage discussed in Section 3.2.1. Given a set height of the microscope stage, the HPF filter was a simpler solution for eliminating the DC offset than the LPF and inverting buffer combination. The HPF still presented instability of the comparator output on the falling edge of the signal. It was evident that this was due to small oscillations on the falling edge of the voltage signal, as shown in Fig. 5.15 (b), that were detected because of the level of the DC offset on the reference signal.

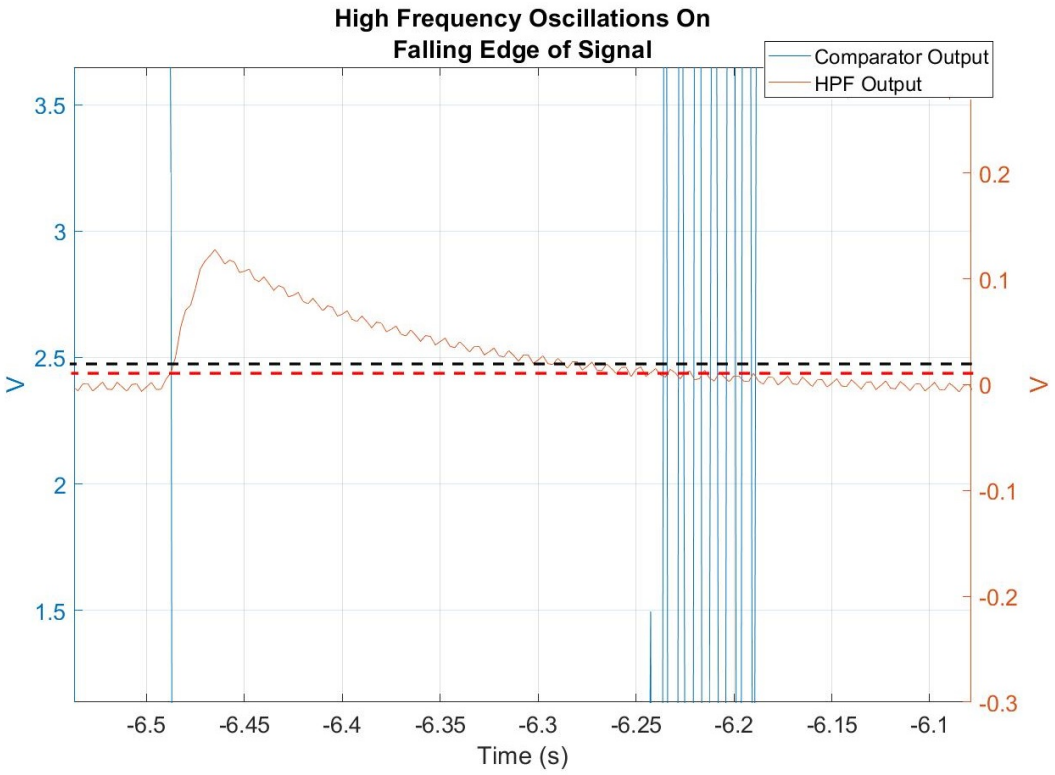

Figure 5.16: Falling edge of the signal out of the HPF with two DC voltage levels influence by resistors at the input. Black dotted line shows a possible DC voltage level using a higher valued resistor at the comparator inputs compared to the red dotted line showing a possible DC voltage level using a lower valued resistor. The red dotted line at the lower voltage level allows more high frequency oscillations to fluctuate around the reference voltage.

5.4 Low Pass Filter at Comparator Output

To eliminate the fluctuations at the output of the comparator shown in Fig. 5.14, a LPF was added to the output of the comparator. A LPF was added to the output of the comparator to suppress the high frequency rail-to-rail fluctuations caused by the high frequency oscillations on the falling edge of the signal. The RC time constant, τ, for the post-comparator LPF was designed to be no longer than 0.3 seconds, which was the approximate time it took for a bead to pass through the optical detection area. Longer recovery times for the LPF would cause the output of the comparator to mask bead/egg events flowing in close succession of each other. The circuit schematic with the LPF at the comparator output is shown in Fig. 5.17.

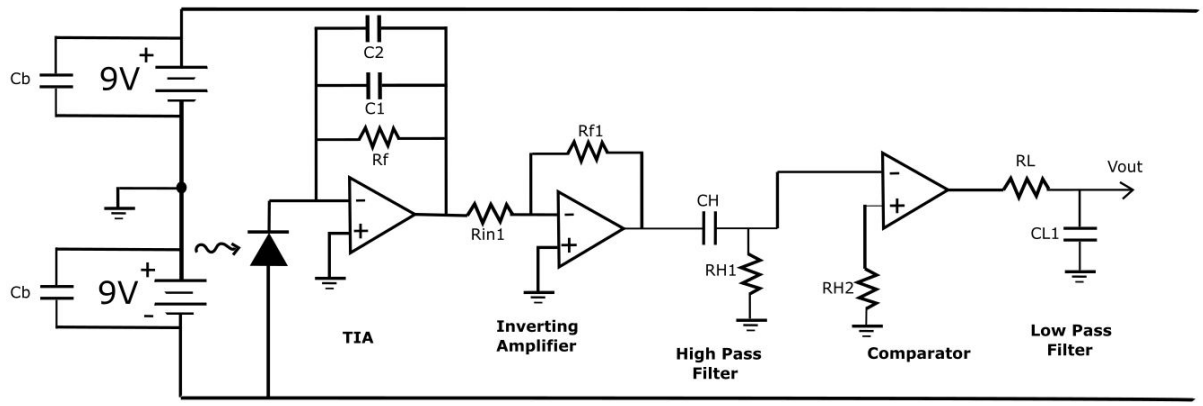

Figure 5.17: Schematic of the circuit that includes a LPF at the output of the comparator. The time constant for the LPF was calculated to be 0.1 seconds with a RL = 10 MΩ and CL = 10 nF.

The reduced rail-to-rail swing of 16 V (Fig. 5.14) to 1.3 V could have been a result of the signal dropping across the large valued resistor, RL, and the signal being recorded directly at the resistor output. This comparator and LPF configuration was able to detect an 18 mV decrease of voltage as well as detect events that occurred in rapid succession. The output from the LPF and decrease in light intensity from sewing thread is shown in Fig. 5.18.

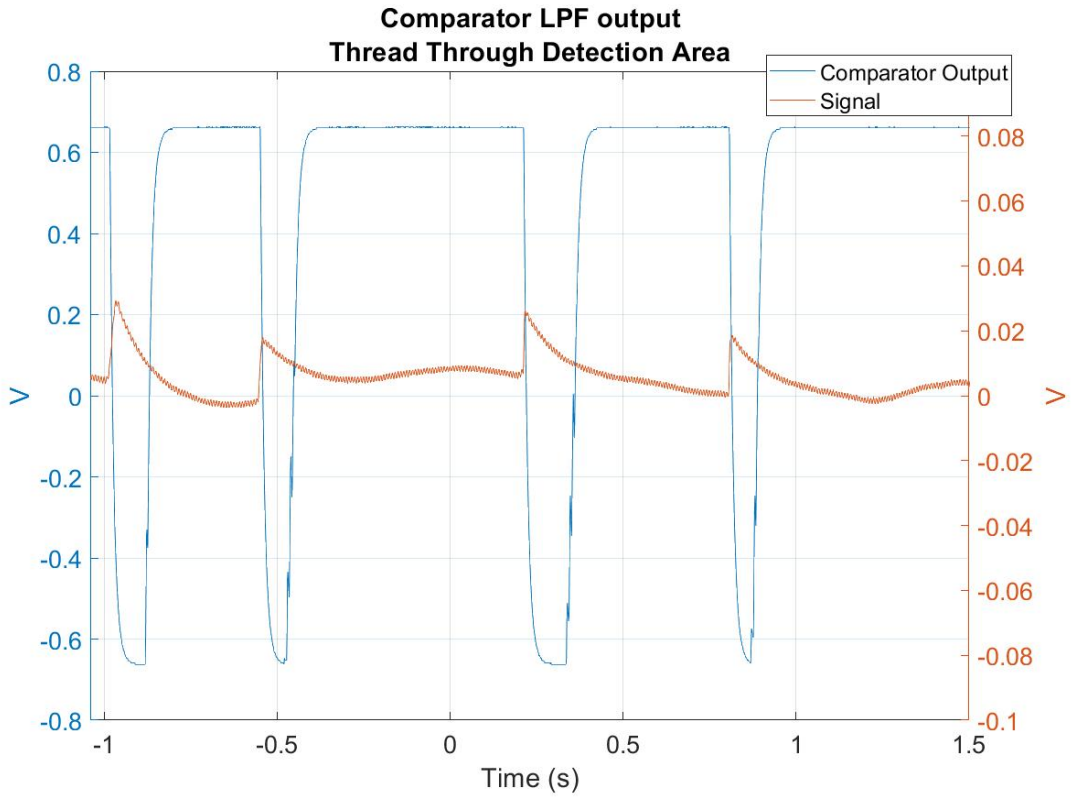

Figure 5.18: The output from the LPF following the comparator resulted in a stabilized output when a thread passed through the detection area. The high frequency rail-to-rail fluctuations on the comparator output were eliminated but the full output swing was suppressed from a 8 V to -8 V swing to a 0.65 V to a -0.65 V swing.

A test was conducted to determine the reliability of the output of the comparator given this particular circuit design. The number of false triggers from the comparator were recorded for when no light was blocked and then the number of triggers were recorded for when the sewing thread was passed through the beam 20 times and at different speeds. The test when no light was blocked ran for approximately 2 minutes. At the start of the test around -50 seconds, the comparator output a full rail-to-rail signal. Other small fluctuations were seen throughout the test, but only one full signal that would act as a trigger or marker for data collection was recorded. The 2 minute test of full light entering the photodiode compared to the output of the comparator is shown in Fig. 5.19.

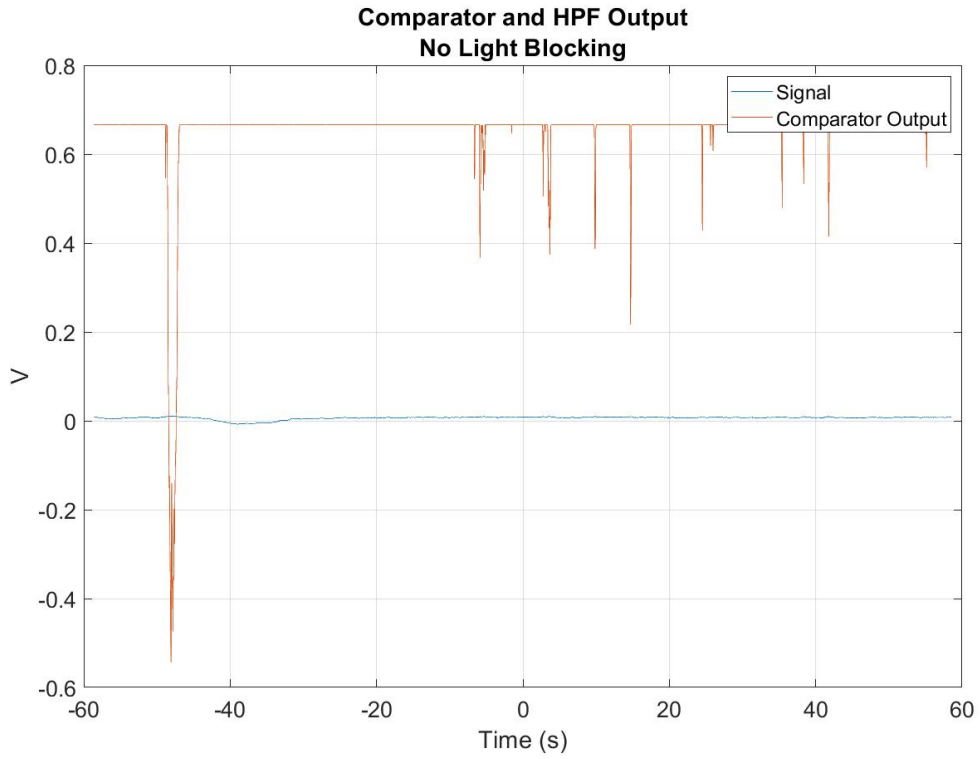

Figure 5.19: The output of the comparator compared to the unblocked light signal for a continual test run of approximately 2 minutes. The only full rail-to-rail output signal occurred at the start of the test run around -50 seconds. Other fluctuations from the comparator output were recorded, but none completed a full swing that would count as a signal for data collection or data marker.

The beam was then blocked 20 times by passing the sewing thread in and out of the detection area at various speeds. One false trigger occurred at the start of the test around -23 seconds, but 100% of the thread passes triggered the comparator. The three sets of passes occurring at seconds 13, 15 and 17, were two passes in rapid succession of each other. Fig. 5.20 demonstrates that even the rapid passes triggered their own output of the comparator.

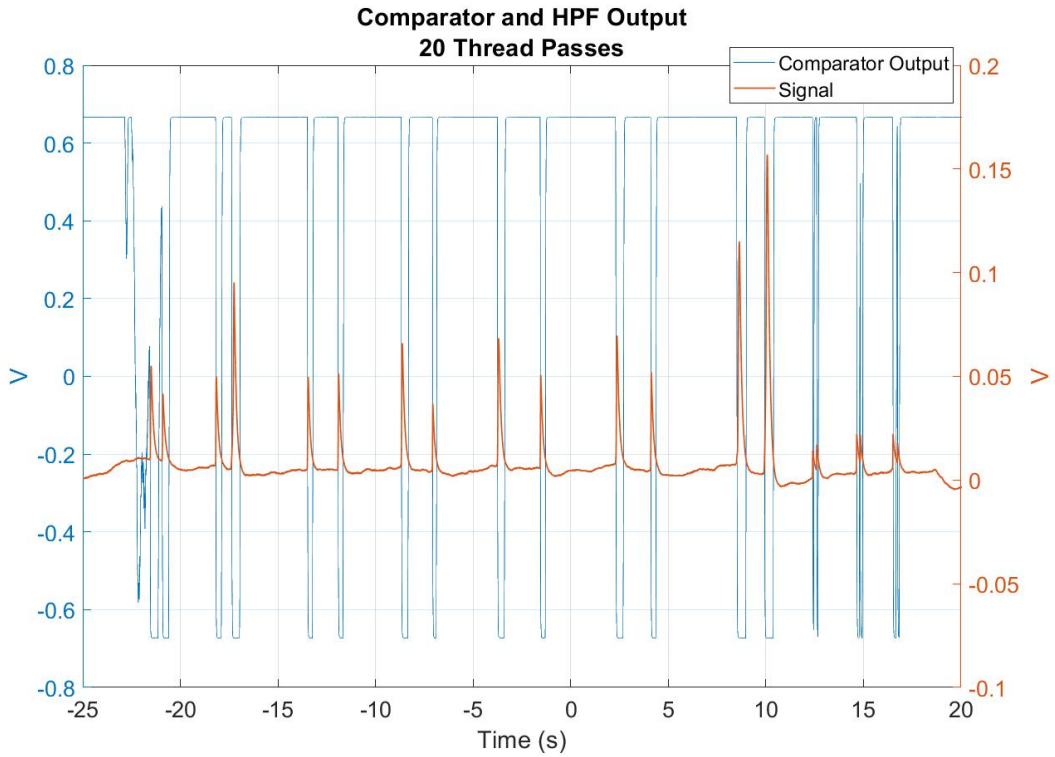

Figure 5.20: The output of the comparator compared to the light blocked by sewing thread passing through the detection area 20 times. One false trigger occurred at the start of the test around -23 seconds, but all other triggers occurred at every pass of the thread. The last three sets of passes at 13, 15 and 17 seconds were passes in rapid succession of each other and each pass was able to produced its own trigger signal.

The HPF proved to be a simple circuit configuration that eliminated the DC offset of the signal and maintained the magnitude of the voltage signal. This HPF configuration replaced the previous LPF and inverting amplifier stage shown in Fig. 5.5. A LPF was added to the output of the comparator to suppress high frequency fluctuations present on the comparator output. The LPF allowed the output of the comparator to still output a trigger for rapid successions events but eliminated false triggers from the high frequency rail-to-rail fluctuations. Through two reliability tests, the HPF and post-comparator LPF design proved to be a robust design as 100% of the 20 thread passes through the optical detection area triggered the comparator and only a single false trigger occurred at the beginning of each test. The addition of the HPF after the inverting amplifier proved to be a more robust and simpler solution to the LPF and inverting buffer configuration used in earlier stages of the circuit design.

Chapter 6

Design Adaptability

6.1 Introduction

Optics can be incorporated into microfluidic research with simple design methods and easily available components. The methods outlined in this manuscript utilized different kinds of microscopes, variety of light sources and a basic circuit. Different microfluidic devices and bench set-ups required slight variations to the technique, but was constructed using the same principles. Implementing this simple method into small or non-optics labs can add additional measurement tools such as counts, triggers and even elementary absorptions measurements without altering the basic design and motivation of the research. These tools could potentially provide confidence and verification to the main source of data on the microfluidic device.

Details on the various ways optics are used and integrated in microfluidics is discussed in Section 2.6 of this manuscript. Most of these methods require special equipment, microfabrication and trained personnel to operate and design the optics [14, 7] which limits the type of laboratories and researchers that can benefit from optical technology. Using simple circuitry and basic optics, a cost effective count, trigger and optical absorption measurements can be taken to increase validity and confidence in the data collected. The methods outlined in this thesis can be used as a guide to incorporate optical technology to a variety of microfluidic devices and can be applied to any level of research.

6.2 Considerations for Design

The design of simple optics for microfluidic research can be applied to different styles of devices and requires very basic laboratory equipment. Design considerations should be made based on opacity of microfluidic device, ability to modify the chip for optical integration, microscope and light sources available and the overall goal for the research. A circuit for signal processing can

be designed using common electrical components to achieve the desired level of sensitivity of the system as well as desired manipulation of the signal. For a basic design, minimal and inexpensive components and equipment is needed to successfully create an optical detection tool.

When working with clear devices, no modifications to the original chip design is necessary as the transparent material allows illumination and detection to be conducted off-chip. The off-chip approach was conducted using a microscope for the collection of light into a fiber optic cable. Objective lens magnification and stage location influenced the success of correct voltage levels from the channel and must be adjusted on each system to achieve a correctly functioning circuit (see Section 3.2.1). In opaque devices, such as the PCB in this thesis, modifications such as small holes drilled through the surface of the board are required for illumination and detection. These types of modifications do not affect the over all functioning of the device and does not require equipment such as a microscope to be used. Optical fiber cables are an essential design component for optic integration onto microfluidic devices. Light sources ranging from white light flashlights to LEDs and lasers can be used as a means of illumination and are chosen based on experiment limitations, such as cell opacity to certain wavelengths, and intensity of light needed for collection.

The design of the circuit is based on the desired goals of the optics integrated. The amplification, suppression of oscillations and polarity changes can all easily be designed for desired signal results. A basic detection and counting method would not require as sensitive of a circuit as absorption measurements would. The light source, microscope and device material are factors in the noise and oscillations present in the signal and can be accounted for with the design of the circuit. The entire circuit and possible modifications can be made by using off-the-shelf electrical components such as resistors, capacitors and op-amps. The principle design of the circuit remains the same with only slight modifications made based on equipment used and level of sensitivity desired.

6.3 Set-Up and Test Modifications

The accuracy of tests and results for this research required the process to accommodate two separate bench set-ups and microscope systems. The initial microscope bench set-up illustrated in Fig. 3.1, consisted of a light illuminating the microfluidic slide from below, a beam splitter that directed the collected light from the objective lens to a fiber optic cable, a camera and a horizontal micrometer mount on the microscope stage. The second microscope bench set-up illustrated in Fig 3.2 illuminated the microfluidic slide from below and was collected straight from the objective lens into the fiber optic cable. The second microscope set-up did not have the availability of the camera image to be used as confirmation of objects in the channel and it was much more difficult to align the channel to the detection area without the use of the camera and micrometer mount. Modifications to each microfluidic device design and the accompanying test procedures were required to test the optics on each system.

The microscope stage height in the CSU lab required no vertical translation to place the microfluidic device between the objective lens and stage and there was no additional lens between the illumination source and objective lens. This allowed the baseline voltage to remain constant as no change in the stage height was needed. This made it easier to design the comparator circuit for comparison of the voltages as there was little variability in light entering the objective lens. Until moving the experiment to the second microscope set-up, the range of voltage changes based on the vertical height of the microscope stage was not a factor in the original design. To compensate for this change in baseline voltage experienced with the second microscope, back propagating light through the microscope to determine the working distance and location of the focus of the objective lens was necessary. The microfluidic channel should be placed directly in this focus to avoid any scattering off other surfaces that could also cause a change in this baseline voltage.

Changing microscope bench set-ups required modifications to how tests of the circuit were conducted and added new variables to consider when conducting the experiment. The lack of image verification on the second microscope set-up made it difficult to accurately run a test of the circuit's ability to detect glass beads flowing through the microfluidic channel. At early stages of

the circuit design, validity was necessary to determine if the changes in voltage were from particles of interest or debris. In place of glass beads, sewing thread and fishing line were passed in and out of the detection area to simulate moving glass beads or parasite eggs. These methods used to test the circuit with the sewing thread and fishing line allowed for verification that the resulting changes in voltage corresponded to an event of interest.

6.4 Alterations of Microfluidic Chip

The microfluidic chips used in this study were glass MIC chips and PCB MIC chips. The initial design of glass chip required no alteration to the original design to implement the optics while the PCB chip required a slight re-design that incorporated small holes above and below the microfluidic channel for optic integration. Both chip designs required modifications to be used on the second microscope set-up to accommodate the optical measurements. These modifications were simple structural changes to the device and did not impede the overall function of the glass chip, but the additional holes aligned with the channel on the PCB did yield possible areas of leakage. The method for melting the POF in place on the PCB allowed the junction of the POF to the channel to maintain optical transparency while plugging possible leakage areas. Refer to Chapter 3 for information regarding specific modifications to each chip design.

Chapter 7

Conclusion

The integration of optical technology to microfluidic devices provided an additional detection and measurement tool. Optical detection methods can be used in on and off-chip approaches depending on the microfluidic device and the goals for the research. The optical detection method in this study was designed using a simple light detection and trigger circuit and applied to glass and PCB microfluidic devices. This design was successful in detecting a change in light intensity from 63-75 μm glass beads flowing through the channel which was a proof-of-design that the optical apparatus could detect light changes from stronglye-type eggs passing through the channel. The design outline in this manuscript can be easily implemented into basic and advanced microfluidic research.

The final design of the circuit was composed of a TIA, inverting amplifier, HPF, comparator and LPF. The TIA was used to amplify the light signal and convert it to a voltage that could be processed by the downstream circuit. The signal from particles ranging from 63-80 μm was anticipated to be below a desired voltage of 10 mV so an additional amplifier was used to create a distinguishable signal that could be easily read by the op-amp comparator. The HPF was used to remove the DC offset of the measured signal and was compared to ground by the comparator. The output of the comparator served as the signal or trigger for when a particle of interest passed through the detection area. A LPF at the output of the op-amp comparator was used to eliminate any high frequency pulses that caused the output of the comparator to fluctuate.

Early versions of this optical detection method successfully detected moving glass bead through the microfluidic channel. Glass beads were used as test samples as they were approximately the same size as strongyle-type eggs which was the main research being conducted by these particular microfluidic devices. Glass beads were shown to produce a change in light intensity ranging from 1.7 to 3.7 mV that blocked 8% to 20% of the total light. This yielded confidence that stronglye-type eggs flowing through the channel would be recorded by this detection circuit.

Due to the global pandemic of COVID-19, in lab experimentation was discontinued and the remainder of the experiment was conducted with an at-home modified set-up. Moving the experiment to a new microscope required modifications to the microfluidic devices, optical apparatus and testing procedures to continue work on the research. These modifications did not inhibit the ability to carry out the experiment and in turn enhanced the process by creating a protocol for testing and a circuit design to accommodate changing systems.

In addition to the glass device, a PCB device was modified to include on-chip optics for the same detection technique used for the glass device. The original PCB design had to be altered by drilling two 0.3 mm holes aligned with the channel where POF cables could be inserted. The POF cables were melted into the holes and used as an illumination and detection source for the microfluidic channel. The testing of the PCB optics was conducted using a dried paint spot onto fishing line that was pulled through the channel using the ends of the line. This allowed confirmation that the changes in light intensity were correlated to an event of interest.

The off-chip detection method conducted using the glass MIC device and microscope set-up caused some difficulties in alignment of the external optics for proper testing. The microfluidic channel had to be aligned to the fiber's image on the device to ensure that the light collected was coming from the channel. The slight misalignment of the device showed that scattering off the edge of the adhesive channel lowered the baseline voltage which would cause a malfunction in the trigger circuit. The on-chip device required no external alignment, but did require chip modifications. The test sample of a dried paint spot on fishing line was used to test the on-chip optics of the PCB device. As this test sample spanned most of the width of the channel, an accurate sensitivity for the integrated optics on this device was not determined during this experiment.

The integration of simple optics provided an additional measurement tool that could enhance the data acquisition on both microfluidic devices. With common equipment and components, this design was successfully implemented and tested for the on and off-chip approaches. This additional optical detection tool will enhance the validity of data obtained by these devices which will yield greater confidence in the data analysis and results obtained.

7.1 Future Work

The future work of this project includes syncing the detection signal to the data acquisition device, moving the completed circuit to a PCB and using the implemented optics to obtain absorption measurements of the particles. The halt on this stated future work was a result of the CSU labs closing for the second half of the spring semester and subsequent summer semester because of the COVID-19 pandemic. Syncing the detection circuit to the data acquisition device will allow for the electronics to begin data acquisition only when a particle of interest passes through the channel as well as providing markers of the events that can be correlated to the impedance data. Additionally, transferring the completed circuit from the breadboard onto a PCB would eliminate possible interference in the signal as well as making the device more portable and user friendly.

Increasing the sensitivity of the optical apparatus and circuit could provide the ability to take absorption profiles of the strongyle eggs. This could be used to compare with their impedance measurements and possibly lead to a broader profile of the eggs and/or additional confirmation of structure and size measurements. Obtaining more data and creating confirmation could be beneficial to the science that is directly studying effects, diagnosis and treatments of helminth infections.

References

[1] Xiufeng Li, Fan Beiyuan, Lixing Liu, Deyong Chen, Shanshan Cao, Dong Men, Junbo Wang, and Jian Chen. A microfluidic fluorescent flow cytometry capable of quantifying cell sizes and numbers of specific cytosolic proteins. *Scientific Reports*, 8, July 2018.

[2] Jing Yu, Jing Zhou, Alex Sutherland, Wei Wei, Young Shik Shin, Min Xue, and James R. Heath. Microfluidics-based single-cell functional proteomics for fundamental and applied biomedical applications. *Annual Review of Analytical Chemistry*, 7:275–295, June 2014.

[3] Dongeun Huh, Wei Gu, Yoko Kamotani, James B. Grotberg, and Shuichi Takayama. Microfluidics for flow cytometric analysis of cells and particles. *Physiological Measurement*, 26:73–98, Feb. 2005.

[4] Yongxiang Feng, Liang Huang, Peng Zhao, Fei Liang, and Wenhui Wang. A microfluidic device integrating impedance flow cytometry and electric impedance spectroscopy for high-efficiency single-cell electrical property measurement. *Analytical Chemistry*, 91:15204–15212, 2019.

[5] Jingdong Chen, Di Chen, Yao Xie, Tao Yuan, and Xiang Chen. Progress of microfluidics for biology and medicine. *Nano-Micro Letters*, 5:66–80, March 2013.

[6] Karen Cheung, Shady Gawad, and Philippe Renaud. Impedance spectroscopy flow cytometry: On-chip label-free cell differentiation. *Cytometry*, 65A:124–132, June 2005.

[7] Jessica Godin, Chun-Hao Chen, Sung Hwan Cho, Wen Qiao, Frank Tsai, and Yu-Hwa Lo. Microfluidics and photonics for bio-system-on-a-chip: A review of advancements in technology towards a microfluidic flow cytometry chip. *Journal of Biophotonics*, 1:355–376, Oct. 2008.

[8] Bambang Kuswandi, Nuriman Nuriman, Jurriaan Huskens, and Willem Verboom. Optical sensing systems for microfluidic devices: a review. *Analytica Chimica Acta*, 601:141–155, Nov. 2007.

[9] Jasmine Nejad, Arya Mugdha, Jesse Wilson, Ashley McGrew, and Kevin Lear. Multifrequency microfluidic impedance cytometry using a field programmable gate array for parasite egg analysis. *Journal of the Rocky Mountain Bioengineering Symposium*, 2020.

[10] S Momčilović, C Cantacessi, V Arsić-Arsenijević, D Otranto, and S Tasić-Otašević. Rapid diagnosis of parasitic diseases: current scenario and future needs. *Clinical Microbiology and Infection*, 25:290–309, March 2019.

[11] Momar Ndao. Diagnosis of parasitic diseases: Old and new approaches. *Interdisciplinary Perspectives on Infectious Diseases*, 2009, Dec. 2009.

[12] J.S. McGrath, C. Honrado, D. Spencer, B. Horton, H.L. Bridle, and H. Morgan. Analysis of parasitic protozoa at the single-cell level using microfluidic impedance cytometry. *Scientific Reports*, 7, June 2017.

[13] Klaus B. Mogensen and Jörg P. Kutter. Optical detection in microfluidic systems. *Electrophoresis*, 30:92–100, March 2009.

[14] Kathleen E. Bates and Hang Lu. Optics-integrated microfluidic platforms for biomolecular analyses. *Biophysics Journal*, 110:1684–1697, April 2016.

[15] Laura Kramer. Science and innovation in parasite diagnostics in companion animals. *Companion Animal*, 21(6):316–322, June 2016.

[16] Ziyi He and Jin-Ming Lin. *Recent Development of Cell Analysis on Microfluidics*. Singapore: Springer Nature Singapore Pte Ltd., 2018.

[17] Marshall Graham. The coulter principle: foundation of an industry. *Journal of the Association for Laboratory Automation*, 8:72–81, Dec. 2003.

[18] National Center for Veterinary Parasitology. Nematodes. https://www.ncvetp.org/nematodes.

[19] Kyo Miyaki, Yanli Guo, Takuya Shimosaka, Tatsuro Nakagama, Hizuru Nakajima, and Katsumi Uchiyama. Fabrication of an integrated pdms microchip incorporating an led-induced fluorescence device. *Analytical and bioanalytical chemistry*, 382:810–816, July 2005.

[20] Julia Sandell and Timothy C. Zhu. A review of in-vivo properties of human tissues and its impact on pdt. *Biophotonics*, 4(11-12):773–787, 2011.

[21] A. Douplik, G. Saiko, I. Schelkanova, and V.V. Tuchin. *Lasers for Medical Applications*. Woodhead Publishing Series in Electronic and Optical Materials, 2013.

[22] Texas Instruments. *Industry-Standard Dual Operational Amplifiers*, Oct. 2019.

[23] All About Circuits. Temperature coefficient of resistance. https://www.allaboutcircuits.com/textbook/direct-current/chpt-12/temperature-coefficient-resistance/.

[24] Polymer Properties Database. Melting points of polymers. http://polymerdatabase.com/polymer%20physics/Polymer%20Tm%20K2.html.

[25] Paul Horowitz and Winfield Hill. *The Art of Electronics*. Cambridge University Press, 1989.

Appendix A

Heat Calculations for PCB

An additional method for optical integration on the PCB microfluidic device was investigated using a heated wire clamped between the two PCBs. The heating element was constructed using an 8 cm long, 29 gauge presumably steel wire, connected to a 9 V battery. The microfluidic channel on each board was aligned to the wire and clamped into place. The motivation behind this technique was to use the heated wire to melt the POF cables flush to the board. The wire used had no label on the spool, but was assumed to be steel based on appearance. The apparatus with the clamped PCB is shown in Fig. A.1.

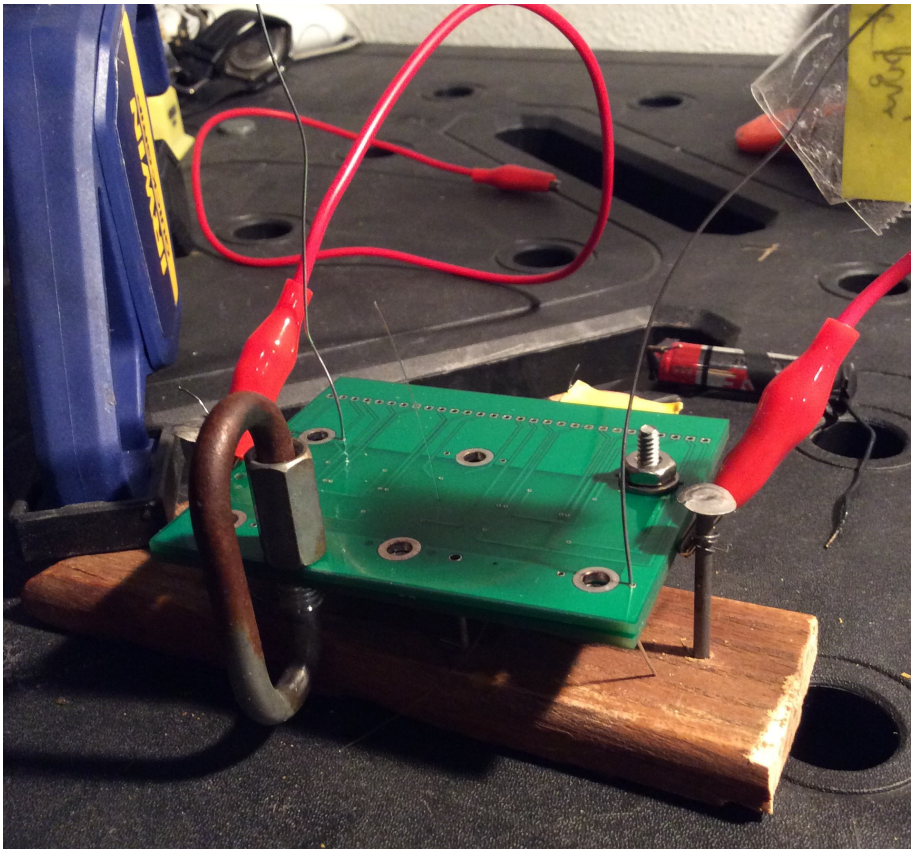

Figure A.1: The PCBs clamped around the wire heating device made from a 29 gauge wire and a single battery.

This home found wire was chosen as it was the only wire readily available of the approximate gauge that fit in the channel. Due to COVID-19, access to other materials such as nichrome wire was delayed by approximately 4 weeks. Steel wire has a resistivity of 90×10^{-6} ohm $\cdot$ cm as compared to the larger resistivity of nichrome wire (commonly used for heating elements) which is 112×10^{-6} ohm $\cdot$ cm. The resistivity of steel is 80% of the resistivity of nichrome (the two values differ by 22×10^{-6} ohm $\cdot$ cm) so it was expected that steel wire would still be able to produce heat to possibly melt the Poly(methyl methacrylate) (PMMA), which was the material of the POF cable.

To model the heat flow and temperature of the wire, the heat (diffusion) equation was solved

$$\frac{\partial T}{\partial t}(cm_D A) = \kappa A \frac{\partial^2 T}{\partial x^2} + H \tag{A.1}$$

where $\partial T/\partial t$ is the temperature change of the wire over time, c is the specific heat capacity, m_D is mass density, A is the cross-sectional area, κ is the thermal conductivity, $\partial^2 T/\partial x^2$ is the second derivative of the temperature along the length of the wire and H is the power generation per unit length. If we assume the system is in steady state, $\partial T/\partial t = 0$, this means that the heat transfer along the wire does not vary with time, then the equation becomes

$$\frac{\partial^2 T}{\partial x^2} = -\frac{H}{\kappa A}. \tag{A.2}$$

To solve, Eq.A.2 is integrated with respect to x

$$\int \frac{d^2 T}{dx^2} dx = -\frac{H}{\kappa A} \int dx \tag{A.3}$$

and then integrated again to obtain a final equation for T

$$\int \frac{dT}{dx} dx = -\frac{H}{\kappa A} \int (x + C) dx \tag{A.4}$$

$$T = -\frac{H}{\kappa A}\left(\frac{x^2}{2} + Cx + B\right). \tag{A.5}$$

If the system is assumed to be symmetric, then the heat generation along the wire is also symmetric. With the boundaries at $x = 0$ and $x = 2L$ at a fixed temperature T_0, then the solution for temperature for the first half of the wire, T_L (from $x = 0$ to $x = L$), will be equal to the solution for the second half of the wire, T_{2L} (from $x = L$ to $x = 2L$). The boundary of this system, $x = 0$ and $x = 2L$, can be assumed to be at the same initial temperature T_0 as the nails the wire was wrapped around did not heat up (this was confirmed by touching the nail during testing). The heat along the wire is uniform when operating under the assumption that the resistance of the wire does not change as temperature increases.

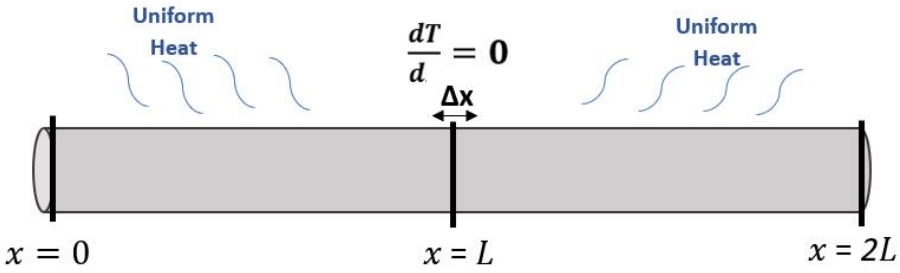

Figure A.2: Heat is uniform along a wire with the assumption that the resistance along the wire is also uniform. No heat is transferred across the center of the wire $x = L$.

This implies that in this steady state condition, there is no heat transfer that occurs from the center of the wire to a small region Δx, i.e. $\partial T/\partial x = 0$. Heat transfer occurs only when there is a temperature difference in a medium. As a voltage is applied to the wire and it begins to heat up, the atoms in a bound state (for a solid object) begin to vibrate and run into the neighboring atoms. Heat flows from the high temperature, or "hot" area, to the low temperature, or "cooler" area. In this steady state model, the nails at the end of the wire are kept at a constant temperature, T_0, so the flow of heat generated through the wire at a constant temperature will flow towards those boundaries and the rate of heat flow increases towards the boundaries shown in Fig. A.3.

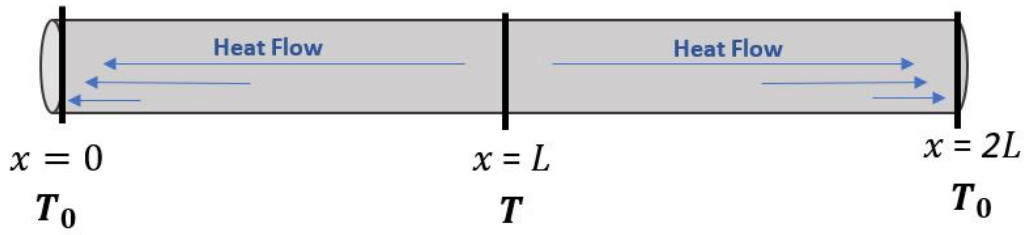

Figure A.3: Heat flows from the warmer medium to the cooler medium with the heat flow increasing towards the boundaries. In the case of this wire, heat flow was towards the nails that were kept at a fixed temperature T_0.

Eq. A.4 was evaluated at $x = L$ to solve for constant C.

$$\frac{dT}{dx}|_{x=L} = -\frac{H}{\kappa A}(x + C)|_{x=L} = 0 \tag{A.6}$$

Equation A.6 requires the value of C to be $-L$. Constant B was solved by evaluating Eq. A.5 at $x = 0$ where $T = T_0$.

$$T|_{x=0} = -\frac{H}{\kappa A}\left(\frac{x^2}{2} - Lx + B\right)|_{x=0} = T_0 \tag{A.7}$$

where $B = -(\kappa A/H)T_0$. The final equation for the temperature change, ΔT= $T(x) - T_0$, across the wire in steady state with heat generation was found to be

$$\Delta T(x) = -\frac{H}{\kappa A}\left(\frac{x^2}{2} - Lx\right). \tag{A.8}$$

The voltage output of the 9 V battery was directly measured and found to be 1.2 V. Every battery has an internal resistance that limits the voltage it can supply to a load. The internal resistance coupled with the fact that the battery had been previously used could have contributed to the decrease in output voltage. A range of current values between 1.6 A and 1.8 A were measured directly using a multimeter in series with the wire and battery for a 32 second test. These current values are plotted vs time in Fig. A.4.

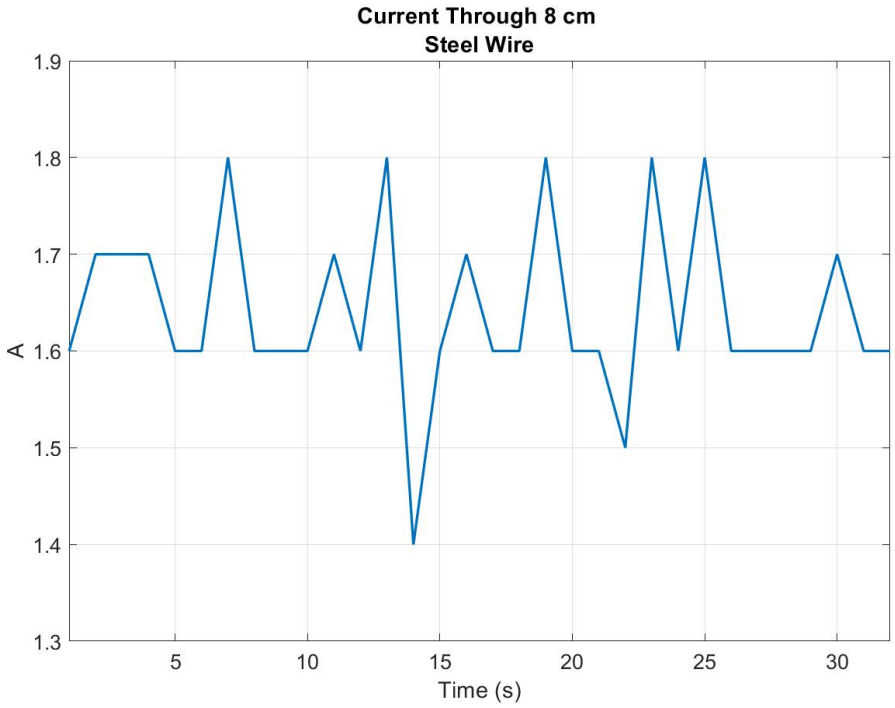

Figure A.4: The range of current values through the wire that fluctuated between 1.6 A and 1.8 A measured directly using a multimeter for a 32 second test of the battery.

Power generated by a voltage source across this wire can be calculated by

$$P = \frac{V^2}{R} \tag{A.9}$$

and the resistance of the wire can be calculated by

$$R = \frac{\rho L_{length}}{A} \tag{A.10}$$

where L_{length} is the length of the wire and A is the cross-sectional area of the wire with a value of 0.062 mm^2. The value of resistance for the full length (8 cm) of a steel wire was calculated to be 1.17 Ω, which means the calculated power for the full length of this wire would be 1.2 W. Based on the measured values of the wire with a voltage of 1.2 V and current of 1.6 A, the actual resistance across this full wire was calculated to be $R_{measured}$ = 0.75 Ω using Ohm's Law ($V = IR$). This

means that the actual resistance across half this wire was R_{half} = 0.37 Ω and subsequent power, P_{half} = 3.9 W. This discrepancy is due to not knowing the actual material of the wire used.

To determine the temperature of the steel wire at $x = L$, the heat generated for half the length of the wire had to be calculated using the equation

$$H = \frac{V^2/R}{L}. \tag{A.11}$$

Using the calculated value of $R_{half} = 0.37\ \Omega$, half the measured voltage $V_{half} = 0.6$ V and the measured value of $L = 0.04$ m, the heat generated H was calculated to be 24.3 W/m.

The temperature of the center of the wire, $x = L$, in steady state was calculated using Eq. 8

$$\Delta T(L) = \frac{24.3\text{W/m}(0.04\text{m})^2}{2 \times 50.2\text{W/m K} \times 62\mu\text{m}^2} \tag{A.12}$$

for a value of $\Delta T = 6252$ °C which was too large of a value to be possible. By observation, the wire was warm to the touch and, from a previous test, the observed wire smoked briefly and was too hot to touch (using a brand new battery). Eq. A.8 was plotted to illustrate the temperature change along this wire and is shown in Fig. A. 5.

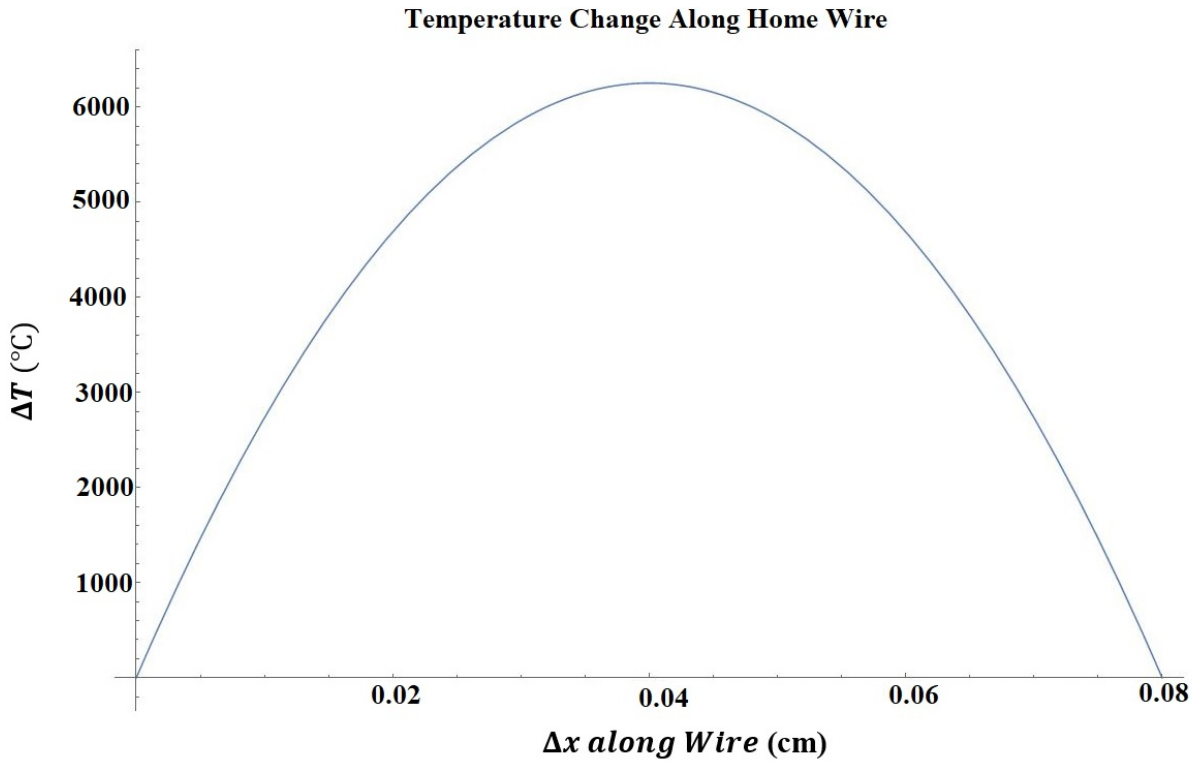

Figure A.5: Simulated temperature change along the home found wire. This wire was shown to have a ΔT of around 6252°C at the center $x = L$ which was not a logical value of temperature or consistent with the physical observations.

A temperature change of this magnitude was not logical or consistent with the observed by touch physical temperature change of the wire in question. The same calculation was done for a theoretical nichrome wire of the same gauge and same length. The thermal conductivity of nichrome is 11.3 W/mK with a resistance of 1.45 Ω was calculated for the full length of the wire and the rate of heat generation per unit length, H was found to be 6.23 W/m. The change in temperature of a 29 gauge nichrome wire over 8 cm is illustrated in Fig. A.6.

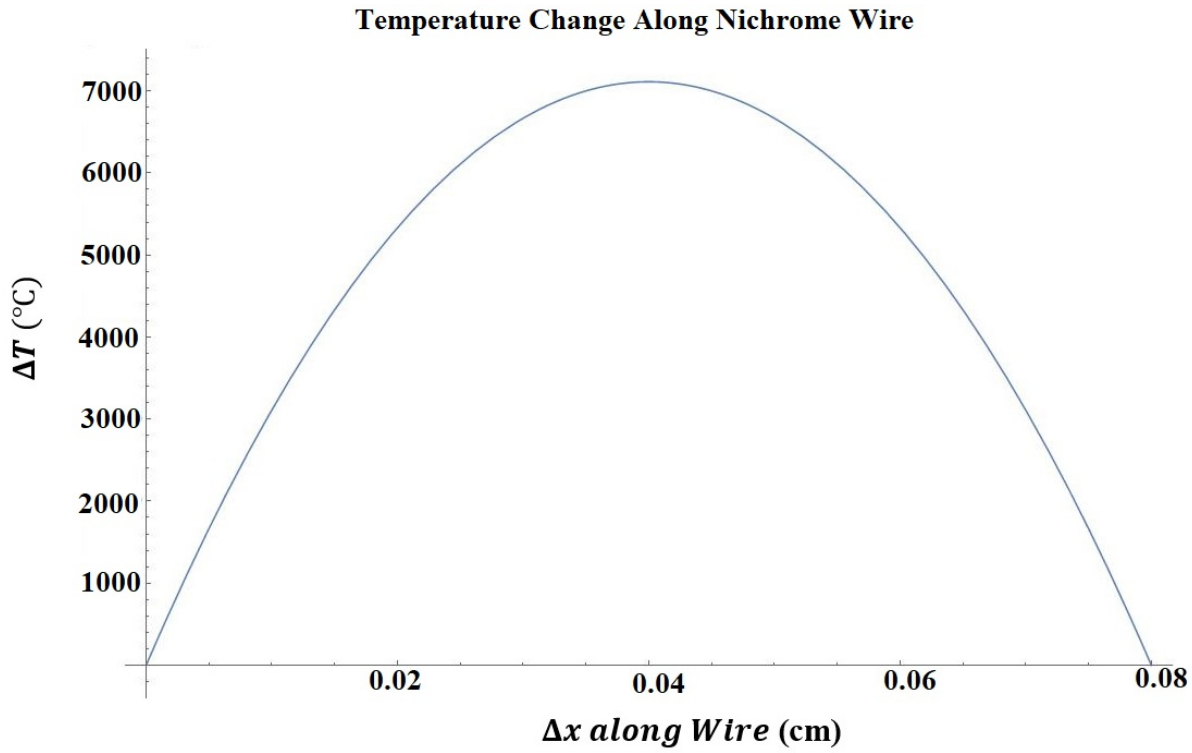

Figure A.6: Simulated temperature change along an 8 cm long 29 gauge nichrome wire. This wire was shown to have a value of ΔT of a little less than 7111°C at the center $x = L$.

The change in temperature profile over the length of the wire calculated for nichrome still blows up to a ΔT around 7111°C. These results show that the wire found at home was probably not steel, as a steel wire of that size would not be able to conduct that amount of current, and both temperature values blow up for this size or wire and material. The wire used in this test probably had a higher resistance and lower thermal conductivity value than that of steel.

The resistance of a metal at changing temperatures can be approximated using the the equation

$$R(T) = R_0[1 + \alpha(T - T_0)] \tag{A.13}$$

where R_0 is the reference resistance at temperature T_0, α is the temperature coefficient of resistance of the metal and $R(T)$ is the resistance at desired temperature T. For steel, the temperature coefficient of resistance is $\alpha = 0.003$ /°C at 20°C [23]. If the 8 cm steel wire was heated to the melting temperature of 150°C for PMMA [24] with an initial $T_0 = 20$°C and $R_0 = 0.75\ \Omega$, then

a temperature change of 130°C would increase the resistance of the wire to $R(T) = 1.0\ \Omega$. For nichrome, $\alpha = 0.00017$ /°C at 20°C [23] and a value of $R(T)$ was calculated to be 1.48 Ω. As the temperature continues to increase, the resistance increases thus producing more heat. These resistance values calculated show an increase of approximately 0.02 and 0.03 Ω respectively which would not greatly change the temperature values calculated and have a limited affect on the modeling of the temperature change of this system.

To determine why this wire used for this experiment did not effectively melt the POF to the PCB, definitive values would need to be obtained. Based on observation, the wire did heat up to cause some melting of the POF, but did not maintain this temperature for a long enough period of time. Using a smaller gauge wire could prove to have a more successful result with this method of melting the POF cable to the PCB. With a smaller gauge wire, the temperatures would not seemingly blow up causing a fast burn out of the material and could possibly maintain the temperature longer. The localized heat from the soldering iron was applied for 5 to 10 seconds which allowed the POF to adhere to the PCB and melt the terminal end flush with the channel. Fig. A.7 shows the terminal ends of the POF melted with localized heat compared to the melted end with the wire clamped between the two PCBs.

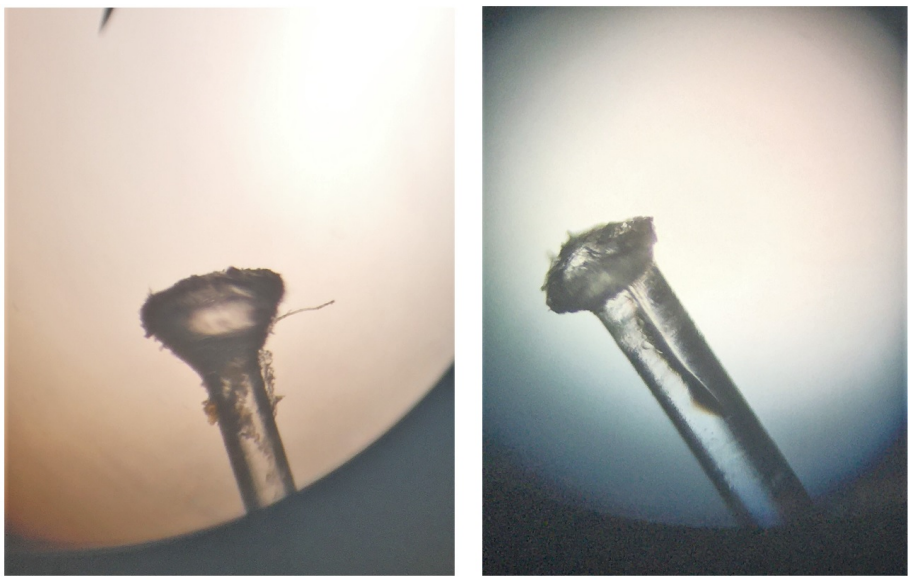

Figure A.7: The terminal ends of the melted POF cables from (a) localized heat using a soldering iron and (b) heated wire clamped between PCBs. The heated wire did cause some structure change to the POF cable when inserted into the hole, but it was not enough to secure the POF into the hole. Localized heat for 5 to 10 seconds applied to the POF was the best method for securing the POF onto the PCB.

While the POF cable in Fig. A.7 (b) did expand at the end slightly, it was not enough to secure the POF into the hole or melt it flush to the channel side of the PCB. The temperature from the home wire could reach a value to melt the POF, but could not maintain a high enough temperature to melt and adhere the POF to the desired form. Thus the method using the tip of the soldering iron proved to be a better method for securing the POF to the PCB.

Appendix B

Operational Amplifier Non-Idealities and Considerations

Operational amplifiers (op-amps) operate by two golden rules when used as feedback circuits: 1) no current flows in or out of the inputs of an op-amp and 2) their output continually adjusts so the voltage difference between the inputs remains zero [25]. The assumptions of perfect operation under the golden rules make analysis and approximation of a circuit design easy as real op-amps operate close to their ideal conditions. In real components, non-idealities present result in deviation from these golden rules possibly leading to unexpected behavior or outputs of the circuit. These non-idealities are important to understand when troubleshooting any op-amp configuration.

Offset voltage and bias currents in op-amps are the apparent differences of voltage and current between the two input pins. The unmatched voltage values at the input causes a non-zero output of the op-amp even when the differential input voltage is zero. The input offset voltage is amplified by the gain in the feedback circuit so in a circuit with higher gain, the more offset voltage will be seen on the output signal. In the TIA design discussed in Section 4.2 this document, a large DC offset was present on the signal which could have been due to the 10 MΩ of gain on the 0.3 mV to 2 mV input offset voltage specified for the LM358 op-amp [22] used for this project. The input bias currents are leakage currents present on each input terminal and can lead to an added voltage offset on the inputs. In Section 5.3 of this manuscript, a resistor was added between ground and the non-inverting pin of the op-amp comparator circuit. This resistor had the same value as the one in the HPF to match the impedance at the of inputs of this op-amp to make the non-zero voltages similar at each input.

The slew rate is how fast the output voltage of the op-amp can change. Ideally this would be instantaneous but a component can only change its output as fast as the design allows. This results in a delay between the change in input and change in output. The LM358 has slew rate of 0.5 V/μs

[22] which is considered a slow op-amp compared to faster op-amps that can have slew rates of 100 - 6000 V/μs [25]. The slow slew rate for the LM358 did not affect the results of this experiment as events in the microfluidic channel were separated by multiple seconds and a fast response between input and output of the comparator was not necessary. The total rise time of the output of the LPF at the output of the comparator was 0.45 mV/ms from the data in Fig. 5.14, which is much larger than the slew rate of 0.5 V/μ for the LM358 op-amp [22].

The gain bandwidth (GBW) product is a parameter that describes the gain of an op-amp with respect to the frequency. Ideal op-amps "have infinite gain", however, in real op-amps, the gain is limited. The open-loop gain of a component decreases after a specified cutoff frequency as the frequency increases. This compromises the gain performance of the op-amp. For low gain circuits, the GBW product has little effect on the gain of the circuit.

Offset voltage, input bias currents, slew rate and GBW values vary between op-amps and can be found in each component's data sheets. If the non-idealities yield a significant negative effect on the performance of the circuit, different techniques found in the component data sheets or electronic handbooks can be implemented to mitigate these effects.

Appendix C

Engineering with COVID-19

In March 2020, Colorado State University made the decision to close campus in response to the growing pandemic of the novel severe acute respiratory syndrome coronavirus 2 (commonly called COVID-19). This included the closure of most laboratories across campus, the optics lab this research was being conducted in was one of them. Due to this closure, steps were taken to adapt the continuation of this project outside of the lab. Essential equipment to the research was borrowed from the lab and the final installments of this project was completed in an at-home lab set-up.

The goal of this project was to create a working trigger circuit that was connected to a data acquisition apparatus. The final desired test was to be done using strongyle eggs pushed through the microfluidic device to test the functionality of the circuit and to obtain absorption profiles of the eggs. The final steps on this project were left incomplete and the remainder of the project was focused on various device designs for optic incorporation onto different styles of microfluidic chips.

In lieu of the research progress lost during this time, I believe that an important lesson and perspective on engineering came out of this unique situation. In the academic setting we have the luxury to access all kinds of equipment and specialized knowledge in various fields of study which helps in understanding details, functions and provides greater ease in accomplishing specialized tasks. COVID-19 forced me (and many other STEM students) to work by what engineering is at its core: creative creation and ability to adapt.

When I moved home to my small mountain town after the state-wide lock-down, I was left with extremely limited access to materials and equipment. The limitation on resources available required me to pull from all areas of my expertise to achieve success in this research. After a few weeks of being frustrated over the situation, I began to approach every problem with a new mindset, mainly because I had no other choice if I wanted to succeed. I moved out of the academic

track I had become so accustomed to and was able to start bridging the separation of niche sciences and engineering to the everyday world.

I owe completion of this project to a community in the Colorado mountains, where artists, fire-fighters, ski bums, mushers among many others provided their unique perspectives that promoted problem solving and the success of this thesis. The most important lesson from this research, that I believe would have been lost if I had the luxury to complete this project in the academic world, is that engineering is nothing more than simply being human.

Appendix D

PCB Metal Shaving Test

An initial test of the optical apparatus integrated onto the PC was done using a metal shaving from a steel horseshoe nail externally manipulated using a magnet. The results of this test were not convincing to be able to conclude that the optics worked. The metal shaving was replaced with fishing line with the dried paint spot for a conclusive test of the optics. This appendix describes the method and results of testing using the metal shaving.

The first test of the optics was conducted using a green laser being turned on and off to achieve the benchmark of an absolute change in voltage and this signal was recorded from the output of the inverting amplifier. Green laser light was directed into the bottom hole on the PCB device and turned on and off. The result was a change in voltage of 3.40 V. The voltage when the laser light was turned on caused the 3 drops in voltage because of the polarity change from the inverting amplifier. The benchmark voltages are shown in Fig. D.1.

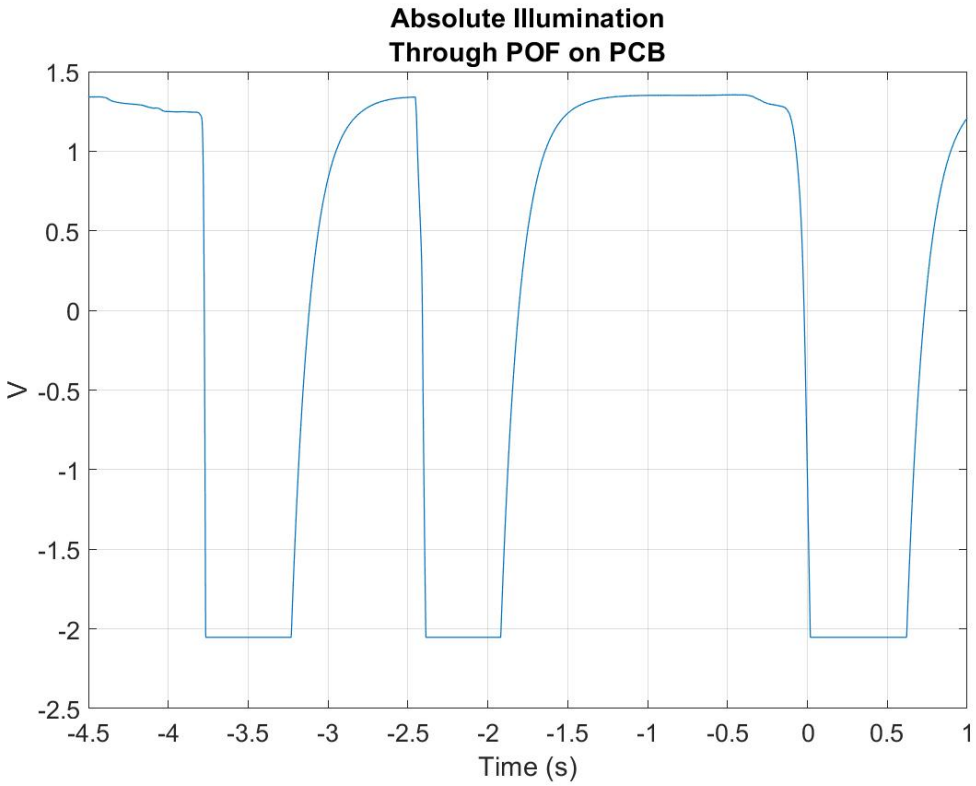

Figure D.1: The output of the inverting amplifier when a green laser was turned on and off through the integrated optics on the PCB microfluidic device. A change in voltage of 3.40 V was recorded.

With the confirmation that the installed POFs were able to accommodate the photodiode in detecting an absolute change in light intensity, a second test using an object in the channel was conducted. A metal shaving approximately 0.7 mm in length, was passed using an exterior magnet through the illuminated channel. The metal shaving in the channel is shown in Fig. D.2.

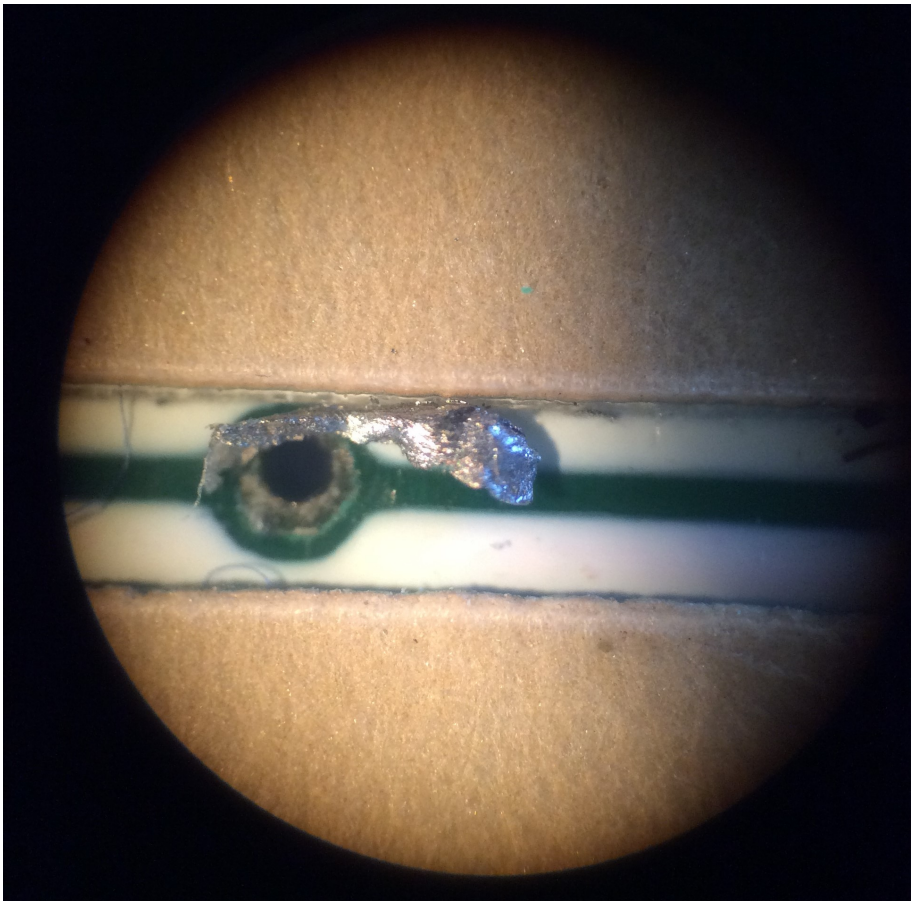

Figure D.2: The metal shaving from a steel horseshoe nail placed inside the microchannel. This shaving is approximately 0.7 mm in length and imaged next to the 0.3 mm drilled hole for reference.

The metal shaving was passed through the detection area 4 times and produced a change in voltage of around 0.07 V which was approximately 2% of the absolute change in voltage. The signals from the metal shaving are shown in Fig. D.3.

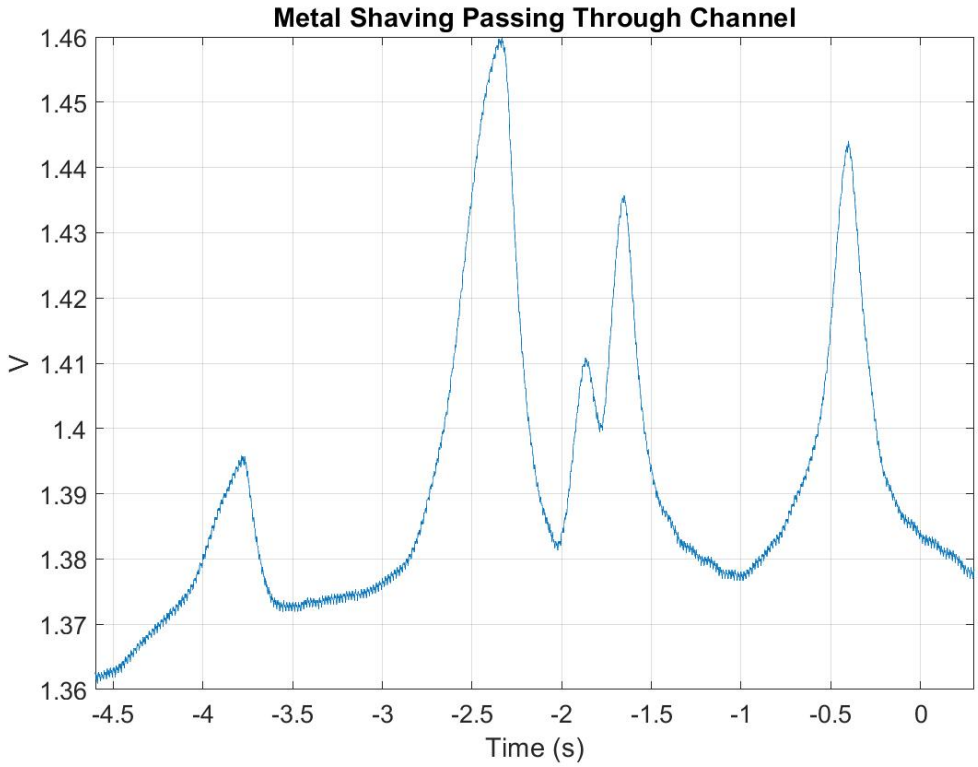

Figure D.3: Voltage change of approximately 0.07 V resulting from a metal shaving manually passed through the detection area four times on the PCB microfluidic device. This was 2% of the absolute change in voltage. The shaving was moved back and forth using an exterior magnet to ensure that the signal recorded was from an object of interest.

It is important to note the differences between the decrease in voltage in Fig. D.1 and the increase in voltage in Fig. D.3. The changes in voltage from the metal shaving shown in D.3 are positive because the light is being blocked by the metal shaving causing a decrease in intensity. The output of the inverting amplifier causes the decrease in intensity to be read as a positive change in voltage. The decrease in voltage shown in Fig. D.1 are due to the channel being illuminated thus showing an increase in light intensity.

Appendix E

Photodiode OPF482 Data Sheet

Specifications for the OPF482 photodiode used for this experiment are provided here for reference. This information is provided by Optek Technology, Inc. in Carrollton, Texas.

Product Bulletin OPF482
August 1996

OPTEK

Fiber Optic High Speed PIN Photodiode in ST* Receptacle
Type OPF482

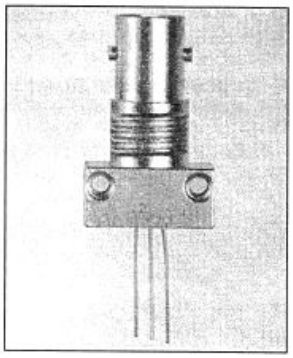

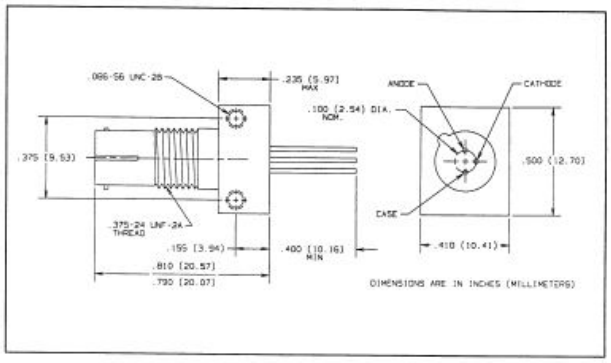

Features

- Component pre-mounted and ready to use
- High speed, low capacitance
- Pre-tested with fiber to assure performance
- Popular ST style receptacle
- Electronically isolated from case

Description

The OPF482 consists of a low cost plastic cap PIN photodiode pre-mounted and aligned in an ST receptacle. This configuration is designed for PC board or panel mounting. Includes lock washer and jam nut, two 2-56 screws, and dust cap.

The PIN Photodiodes are designed to interface with multimode optical fibers from 50/125 to 100/140 microns.

*ST is a registered trademark of AT&T.

Absolute Maximum Ratings (T_A = 25° C unless otherwise noted)

Reverse Voltage	100 VDC
Continuous Power Dissipation	200 mW(1)
Storage Temperature Range	-55° C to +100° C
Operating Temperature Range	-40° C to +85° C
Lead Soldering Temperature [1/16 inch (1.6 mm) from case for 5 sec. with soldering iron]	240° C(2)

Notes:
(1) Derate linearly @ 2.0 mW/° C above 25° C.
(2) RMA flux is recommended. Duration can be extended to 10 sec. max when flow soldering.
(3) Test @ V_R = 5 V with 50/125 micron, 0.20 N.A. fiber, @ 10 µW optical power @ 850 nm. Responsivity levels apply to 50 µm, 62.5 µm and 100 µm core optical fibers.

Optek Technology, Inc. 1215 W. Crosby Road Carrollton, Texas 75006 (972) 323-2200 Fax (972) 323-2396

Type OPF482

Electrical Characteristics (T_A = 25° C unless otherwise noted)

SYMBOL	PARAMETER	MIN	TYP	MAX	UNITS	TEST CONDITIONS
R	Flux Responsivity	0.45	0.55		A/W	V_R = 5.0 V(3)
I_D	Dark Current		0.1	5.0	nA	V_R = 5.0 V
λp	Peak Response Wavelength		860		nm	
t_r	Output Rise Time		0.6		ns	V_R = 50 V, R_L = 50 Ω, 10%-90%
t_r	Output Rise Time		1.0		ns	V_R = 15 V, R_L = 50 Ω, 10%-90%
t_r	Output Rise Time		2.0		ns	V_R = 5.0 V, R_L = 50 Ω, 10%-90%
C_T	Total Capacitance		1.5	2.0	pF	V_R = 5.0 V

Typical Performance Curves

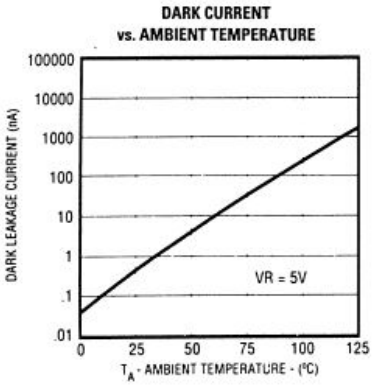

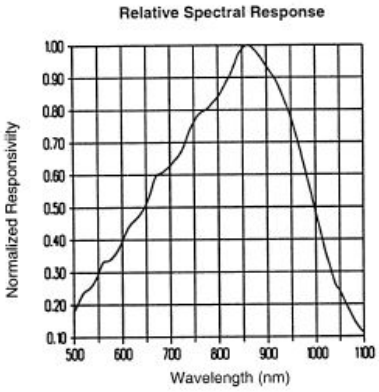

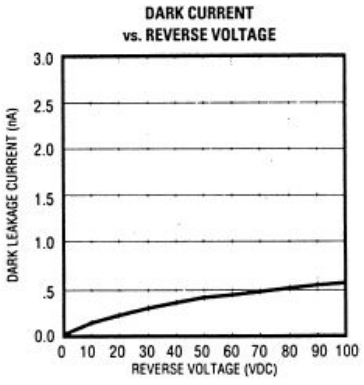

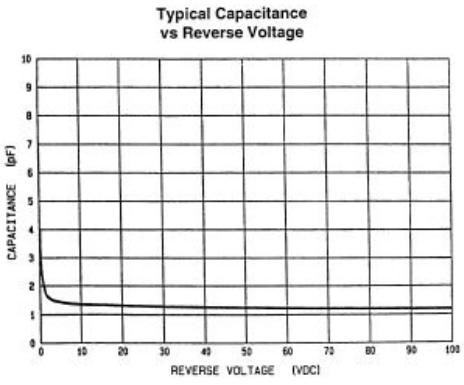

Appendix F

Operational Amplifier LM358 Data Sheet

Specifications for the LM358 op-amp used for this experiment are provided here for reference. This information is provided by Texas Instruments, Inc. in Dallas, Texas. Please see reference [22] for full documentation.

Industry-Standard Dual Operational Amplifiers

1 Features

- Wide supply range of 3 V to 36 V (B version)
- Quiescent current: 300 µA per amplifier (B version, typical)
- Unity-gain bandwidth of 1.2 MHz (B version)
- Common-mode input voltage range includes ground, enabling direct sensing near ground
- Low input offset voltage of 3 mV at 25°C (A and B versions, maximum)
- Internal RF and EMI filter (B version)
- On products compliant to MIL-PRF-38535, all parameters are tested unless otherwise noted. On all other products, production processing does not necessarily include testing of all parameters.

2 Applications

- Merchant network and server power supply units
- Multi-function printers
- Power supplies and mobile chargers
- Motor control: AC induction, brushed DC, brushless DC, high-voltage, low-voltage, permanent magnet, and stepper motor
- Desktop PC and motherboard
- Indoor and outdoor air conditioners
- Washers, dryers, and refrigerators
- AC inverters, string inverters, central inverters, and voltage frequency drives
- Uninterruptible power supplies
- Programmable logic controllers
- Electronic point-of-sale systems

Single-Pole, Low-Pass Filter

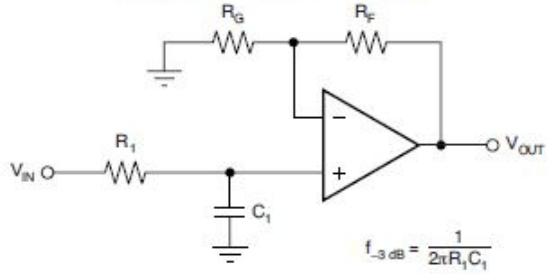

$$\frac{V_{OUT}}{V_{IN}} = \left(1 + \frac{R_F}{R_G}\right)\left(\frac{1}{1 + sR_1C_1}\right)$$

3 Description

The LM358B and LM2904B devices are the next-generation versions of the industry-standard operational amplifiers (op amps) LM358 and LM2904, which include two high-voltage (36-V) op amps. These devices provide outstanding value for cost-sensitive applications, with features including low offset (300 µV, typical), common-mode input range to ground, and high differential input voltage capability.

The LM358B and LM2904B op amps simplify circuit design with enhanced features such as unity-gain stability, lower offset voltage of 3 mV (maximum at room temperature), and lower quiescent current of 300 µA per amplifier (typical). High ESD (2 kV, HBM) and integrated EMI and RF filters enable the LM358B and LM2904B devices to be used in the most rugged, environmentally challenging applications.

The LM358B and LM2904B amplifiers are available in industry standard packages, including SOIC, TSSOP, and VSSOP.

Device Information(1)

PART NUMBER	PACKAGE	BODY SIZE (NOM)
LM358B, LM2904B, LM358, LM358A, LM2904, LM2904V, LM258, LM258A	SOIC (8)	4.90 mm × 3.90 mm
LM358B(2), LM2904B(2), LM358, LM358A, LM2904, LM2490V	TSSOP (8)	3.00 mm × 4.40 mm
LM358B(2), LM2904B(2), LM358, LM358A, LM2904, LM2904V, LM258, LM258A	VSSOP (8)	3.00 mm × 3.00 mm
LM358, LM2904	SO (8)	5.20 mm × 5.30 mm
LM358, LM2904, LM358A, LM258, LM258A	PDIP (8)	9.81 mm × 6.35 mm
LM158, LM158A	CDIP (8)	9.60 mm × 6.67 mm
LM158, LM158A	LCCC (20)	8.89 mm × 8.89 mm

(1) For all available packages, see the orderable addendum at the end of the data sheet.

(2) Package is for preview only.

6 Pin Configuration and Functions

D, DGK, P, PS, PW, and JG Packages
8-Pin SOIC, VSSOP, PDIP, SO, TSSOP, and CDIP
Top View

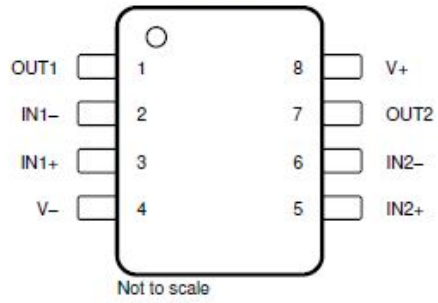

Not to scale

FK Package
20-Pin LCCC
Top View

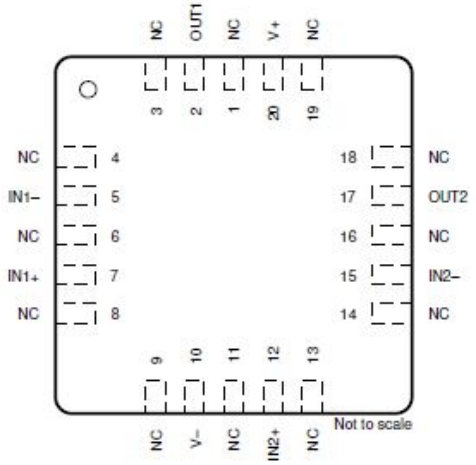

Not to scale

NC - No internal connection

Pin Functions

PIN			I/O	DESCRIPTION
NAME	LCCC[1]	SOIC, SSOP, CDIP, PDIP, SO, TSSOP, CFP[1]		
IN1–	5	2	I	Negative input
IN1+	7	3	I	Positive input
IN2–	15	6	I	Negative input
IN2+	12	5	I	Positive input
OUT1	2	1	O	Output
OUT2	17	7	O	Output
V–	10	4	—	Negative (lowest) supply or ground (for single-supply operation)
NC	1, 3, 4, 6, 8, 9, 11, 13, 14, 16, 18, 19	—	—	No internal connection
V+	20	8	—	Positive (highest) supply

(1) For a listing of which devices are available in what packages, see *Device Comparison Table*.

7 Specifications

7.1 Absolute Maximum Ratings

over operating ambient temperature range (unless otherwise noted)(1)

			MIN	MAX	UNIT
Supply voltage, V_S = ([V+] – [V–])		LM358B, LM358BA, LM2904B, LM2904BA		±20 or 40	V
		LM158, LM258, LM358, LM158A, LM258A, LM358A, LM2904V		±16 or 32	
		LM2904		±13 or 26	
Differential input voltage, V_{ID}(2)		LM358B, LM358BA, LM2904B, LM2904BA,LM158, LM258, LM358, LM158A, LM258A, LM358A, LM2904V	–32	32	V
		LM2904	–26	26	
Input voltage, V_I	Either input	LM358B, LM358BA, LM2904B, LM2904BA	–0.3	40	V
		LM158, LM258, LM358, LM158A, LM258A, LM358A, LM2904V	–0.3	32	
		LM2904	–0.3	26	
Duration of output short circuit (one amplifier) to ground at (or below) T_A = 25°C, $V_S \leq 15$ V(3)				Unlimited	s
Operating ambient temperature, T_A		LM158, LM158A	–55	125	°C
		LM258, LM258A	–25	85	
		LM358B, LM358BA	–40	85	
		LM358, LM358A	0	70	
		LM2904B, LM2904BA, LM2904, LM2904V	–40	125	
Operating virtual-junction temperature, T_J				150	°C
Storage temperature, T_{stg}			–65	150	°C

(1) Stresses beyond those listed under *Absolute Maximum Ratings* may cause permanent damage to the device. These are stress ratings only, and do not imply functional operation of the device at these or any other conditions beyond those indicated under *Recommended Operating Conditions*. Exposure to absolute-maximum-rated conditions for extended periods may affect device reliability.
(2) Differential voltages are at IN+, with respect to IN–.
(3) Short circuits from outputs to V_S can cause excessive heating and eventual destruction.

7.2 ESD Ratings

			VALUE	UNIT
LM358B, LM358BA, LM2904B, AND LM2904BA				
$V_{(ESD)}$	Electrostatic discharge	Human-body model (HBM), per ANSI/ESDA/JEDEC JS-001(1)	±2000	V
		Charged-device model (CDM), per JEDEC specification JESD22-C101(2)	±1000	
LM158, LM258, LM358, LM158, LM258A, LM358A, LM2904, AND LM2904V				
$V_{(ESD)}$	Electrostatic discharge	Human-body model (HBM), per ANSI/ESDA/JEDEC JS-001(1)	±500	V
		Charged-device model (CDM), per JEDEC specification JESD22-C101(2)	±1000	

(1) JEDEC document JEP155 states that 500-V HBM allows safe manufacturing with a standard ESD control process.
(2) JEDEC document JEP157 states that 250-V CDM allows safe manufacturing with a standard ESD control process.

7.3 Recommended Operating Conditions

over operating ambient temperature range (unless otherwise noted)

			MIN	MAX	UNIT
V_S	Supply voltage, V_S= ([V+] – [V–])	LM358B, LM358BA, LM2904B, LM2904BA	3	36	V
		LM158, LM258, LM358, LM158A, LM258A, LM358A, LM2904V	3	30	
		LM2904	3	26	
V_{CM}	Common-mode voltage		V–	V+ – 2	V
T_A	Operating ambient temperature	LM358B, LM358BA	–40	85	°C
		LM2904B, LM2904BA, LM2904, LM2904V	–40	125	
		LM358, LM358A	0	70	
		LM258, LM258A	–20	85	
		LM158, LM158A	–55	125	

7.4 Thermal Information

THERMAL METRIC[1]		LM258, LM258A, LM358, LM358A, LM358B, LM358BA, LM2904, LM2904B, LM2904BA, LM2904V[2]					LM158, LM158A		UNIT
		D (SOIC)	DGK (VSSOP)	P (PDIP)	PS (SO)	PW (TSSOP)	FK (LCCC)	JG (CDIP)	
		8 PINS	8 PINS	8 PINS	8 PINS	8 PINS	20 PINS	8 PINS	
$R_{\theta JA}$	Junction-to-ambient thermal resistance	124.7	181.4	80.9	116.9	171.7	84.0	112.4	°C/W
$R_{\theta JC(top)}$	Junction-to-case (top) thermal resistance	66.9	69.4	70.4	62.5	68.8	56.9	63.6	°C/W
$R_{\theta JB}$	Junction-to-board thermal resistance	67.9	102.9	57.4	68.6	99.2	57.5	100.3	°C/W
Ψ_{JT}	Junction-to-top characterization parameter	19.2	11.8	40	21.9	11.5	51.7	35.7	°C/W
Ψ_{JB}	Junction-to-board characterization parameter	67.2	101.2	56.9	67.6	97.9	57.1	93.3	°C/W
$R_{\theta JC(bot)}$	Junction-to-case (bottom) thermal resistance	—	—	—	—	—	10.6	22.3	°C/W

(1) For more information about traditional and new thermal metrics, see *Semiconductor and IC Package Thermal Metrics*.
(2) For a listing of which devices are available in what packages, see *Device Comparison Table*.

7.5 Electrical Characteristics: LM358B and LM358BA

V_S = (V+) – (V–) = 5 V - 36 V (±2.5 V - ±18 V), T_A = 25°C, V_{CM} = V_{OUT} = V_S/2, R_L = 10k connected to V_S/2 (unless otherwise noted)

PARAMETER		TEST CONDITIONS			MIN	TYP	MAX	UNIT
OFFSET VOLTAGE								
V_{OS}	Input offset voltage	LM358B				±0.3	±3.0	mV
				T_A = –40°C to +85°C			±4	mV
		LM358BA					±2.0	mV
				T_A = –40°C to +85°C			±2.5	mV
dV_{OS}/d_T	Input offset voltage drift			T_A = -40°C to +85°C[1]		±3.5	11	µV/°C
PSRR	Power Supply Rejection Ratio					±2	15	µV/V
	Channel separation, dc	f = 1 kHz to 20 kHz				±1		µV/V
INPUT VOLTAGE RANGE								
V_{CM}	Common-mode voltage range	V_S = 3 V to 36 V			(V–)		(V+) – 1.5	V
		V_S = 5 V to 36 V		T_A = –40°C to +85°C	(V–)		(V+) – 2	V
CMRR	Common-mode rejection ratio	(V–) ≤ V_{CM} ≤ (V+) – 1.5 V	V_S = 3 V to 36 V			20	100	µV/V
		(V–) ≤ V_{CM} ≤ (V+) – 2.0 V	V_S = 5 V to 36 V	T_A = –40°C to +85°C		25	316	µV/V
INPUT BIAS CURRENT								
I_B	Input bias current					±10	±35	nA
				T_A = –40°C to +85°C[1]			±50	nA
I_{OS}	Input offset current					0.5	4	nA
				T_A = –40°C to +85°C[1]			5	nA
dI_{OS}/d_T	Input offset current drift			T_A = –40°C to +85°C		10		pA/°C
NOISE								
E_n	Input voltage noise	f = 0.1 to 10 Hz				3		$µV_{PP}$
e_n	Input voltage noise density	f = 1 kHz				40		nV/√Hz
INPUT IMPEDANCE								
Z_{ID}	Differential					10 || 0.1		MΩ|| pF
Z_{IC}	Common-mode					4 || 1.5		GΩ|| pF
OPEN-LOOP GAIN								
A_{OL}	Open-loop voltage gain	V_S = 15 V; V_O = 1 V to 11 V; R_L ≥ 10 kΩ, connected to (V-)			70	140		V/mV
				T_A = –40°C to +85°C	35			V/mV
FREQUENCY RESPONSE								
GBW	Gain bandwidth product					1.2		MHz
SR	Slew rate	G = + 1				0.5		V/µs
θ_m	Phase margin	G = + 1, R_L = 10kΩ, C_L = 20 pF				56		°
t_{OR}	Overload recovery time	V_{IN} × gain > V_S				10		µs
t_s	Settling time	To 0.1%, V_S = 5 V, 2-V Step , G = +1, C_L = 100 pF				4		µs
THD+N	Total harmonic distortion + noise	G = + 1, f = 1 kHz, V_O = 3.53 V_{RMS}, V_S = 36V, R_L = 100k, I_{OUT} ≤ ±50µA, BW = 80 kHz				0.001		%
OUTPUT								
V_O	Voltage output swing from rail	Positive Rail (V+)		I_{OUT} = 50 µA		1.35	1.42	V
				I_{OUT} = 1 mA		1.4	1.48	V
				I_{OUT} = 5 mA[1]		1.5	1.61	V
		Negative Rail (V-)		I_{OUT} = 50 µA		100	150	mV
				I_{OUT} = 1 mA		0.75	1	V
			V_S = 5 V, RL ≤ 10 kΩ connected to (V–)	T_A = –40°C to +85°C		5	20	mV
I_O	Output current	V_S = 15 V; V_O = V-; V_{ID} = 1 V	Source[1]		-20	-30		mA
				T_A = –40°C to +85°C	-10			
		V_S = 15 V; V_O = V+; V_{ID} = -1 V	Sink[1]		10	20		
				T_A = –40°C to +85°C	5			
		V_{ID} = -1 V; V_O = (V-) + 200 mV			60	100		µA
I_{SC}	Short-circuit current	V_S = 20 V, (V+) = 10 V, (V-) = -10 V, V_O = 0 V				±40	±60	mA
C_{LOAD}	Capacitive load drive					100		pF
R_O	Open-loop output resistance	f = 1 MHz, I_O = 0 A				300		Ω
POWER SUPPLY								
I_Q	Quiescent current per amplifier	V_S = 5 V; I_O = 0 A		T_A = –40°C to +85°C		300	460	µA
I_Q	Quiescent current per amplifier	V_S = 36 V; I_O = 0 A					800	µA

9 Detailed Description

9.1 Overview

These devices consist of two independent, high-gain frequency-compensated operational amplifiers designed to operate from a single supply over a wide range of voltages. Operation from split supplies also is possible if the difference between the two supplies is within the supply voltage range specified in the *Recommended Operating Conditions* section, and V_S is at least 1.5 V more positive than the input common-mode voltage. The low supply-current drain is independent of the magnitude of the supply voltage.

Applications include transducer amplifiers, dc amplification blocks, and all the conventional operational amplifier circuits that now can be implemented more easily in single-supply-voltage systems. For example, these devices can be operated directly from the standard 5-V supply used in digital systems and easily can provide the required interface electronics without additional ±5-V supplies.

9.2 Functional Block Diagram - LM358B, LM358BA, LM2904B, LM2904BA

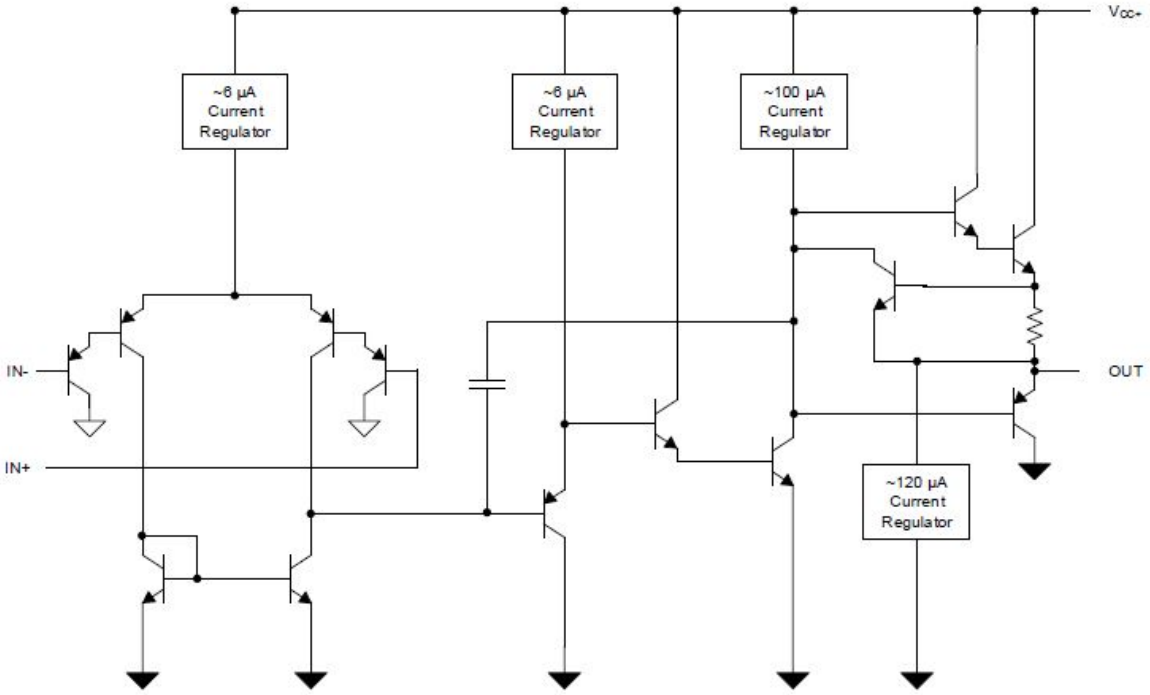

9.3 Feature Description

9.3.1 Unity-Gain Bandwidth

The unity-gain bandwidth is the frequency up to which an amplifier with a unity gain may be operated without greatly distorting the signal. These devices have a 1.2-MHz unity-gain bandwidth (B Version).

9.3.2 Slew Rate

The slew rate is the rate at which an operational amplifier can change its output when there is a change on the input. These devices have a 0.5-V/μs slew rate (B Version).

9.3.3 Input Common Mode Range

The valid common mode range is from device ground to V_S – 1.5 V (V_S – 2 V across temperature). Inputs may exceed V_S up to the maximum V_S without device damage. At least one input must be in the valid input common-mode range for the output to be the correct phase. If both inputs exceed the valid range, then the output phase is undefined. If either input more than 0.3 V below V– then input current should be limited to 1 mA and the output phase is undefined.

9.4 Device Functional Modes

These devices are powered on when the supply is connected. This device can be operated as a single-supply operational amplifier or dual-supply amplifier, depending on the application.